

Preparation of graphene nanocomposites for anticorrosion and sensors



A Dissertation Submitted in Partial Fulfillment of the Requirements  
for the Degree of Doctor of Philosophy in Nanoscience and Technology  
Inter-Department of Nanoscience and Technology  
Graduate School  
Chulalongkorn University  
Academic Year 2018  
Copyright of Chulalongkorn University

การเตรียมนาโนคอมพอสิตของแกรฟีนสำหรับการต้านการกัดกร่อนและตัวรับรู้



วิทยานิพนธ์นี้เป็นส่วนหนึ่งของการศึกษาตามหลักสูตรปริญญาวิทยาศาสตรดุษฎีบัณฑิต  
สาขาวิชาวิทยาศาสตร์นาโนและเทคโนโลยี สหสาขาวิชาวิทยาศาสตร์นาโนและเทคโนโลยี

บัณฑิตวิทยาลัย จุฬาลงกรณ์มหาวิทยาลัย

ปีการศึกษา 2561

ลิขสิทธิ์ของจุฬาลงกรณ์มหาวิทยาลัย

Thesis Title	Preparation of graphene nanocomposites for anticorrosion and sensors
By	Miss Nadtinan Promphet
Field of Study	Nanoscience and Technology
Thesis Advisor	Dr. NADNUDDA RODTHONGKUM, Ph.D.
Thesis Co Advisor	Professor Dr. ORAWON CHAILAPAKUL, Ph.D.

---

Accepted by the Graduate School, Chulalongkorn University in Partial Fulfillment of the Requirement for the Doctor of Philosophy

..... Dean of the Graduate School  
(Associate Professor Dr. THUMNOON NHUJAK, Ph.D.)

DISSERTATION COMMITTEE

..... Chairman  
(Associate Professor Dr. VUDHICHAJ PARASUK, Ph.D.)

..... Thesis Advisor  
(Dr. NADNUDDA RODTHONGKUM, Ph.D.)

..... Thesis Co-Advisor  
(Professor Dr. ORAWON CHAILAPAKUL, Ph.D.)

..... Examiner  
(Assistant Professor Dr. RATTHAPOL RANGKUPAN, Ph.D.)

..... Examiner  
(Assistant Professor Dr. NUTTHITA CHUANKRERKKUL,  
Ph.D.)

..... External Examiner  
(Assistant Professor Dr. Sarute Ummartyotin)

นาฏดินันท์ พรหมเพชร : การเตรียมนาโนคอมพอสิตของแกรฟีนสำหรับการต้านการกัดกร่อน และตัวรับรู้. ( Preparation of graphene nanocomposites for anticorrosion and sensors) อ.ที่ปรึกษาหลัก : ดร.นาฏนิตดา รอดทองคำ, อ.ที่ปรึกษาร่วม : ศ. ดร.อรุวรรณ ชัยลภากุล

วิทยานิพนธ์นี้มุ่งเน้นการพัฒนาแกรฟีนออกไซด์นาโนคอมพอสิต เพื่อพัฒนาสมบัติต่างๆของวัสดุรองรับ สำหรับการใช้งานเป็นตัวรับรู้ โดยแบ่งออกเป็น 2 ส่วนหลัก ในส่วนแรกเป็นการพัฒนาแกรฟีนออกไซด์ร่วมกับระบบการเคลือบนิเกิล-ฟอสฟอรัส เพื่อเพิ่มสมบัติต่างๆของวัสดุรองรับโลหะ สำหรับการใช้งานเป็นตัวรับรู้ทางเคมีไฟฟ้า การเคลือบนิเกิลฟอสฟอรัส-ไททานเนียมไดออกไซด์ โซล-รีดิวซ์แกรฟีนออกไซด์บนผิวโลหะถูกเตรียมโดยการใช้วิธีเคลือบโดยไม่ใช้ไฟฟ้าแบบรวดเร็วได้สำเร็จ จากผลการศึกษาผิวเคลือบพบว่าฟิล์มรีดิวซ์แกรฟีนออกไซด์ ซึ่งมีสมบัติกันน้ำปกคลุมอยู่บนผิวเคลือบอย่างสม่ำเสมอและเป็นเนื้อเดียวกัน ส่งผลให้ผิวเคลือบของนิเกิลฟอสฟอรัส-ไททานเนียมไดออกไซด์ โซล-รีดิวซ์แกรฟีนออกไซด์ มีสมบัติการต้านทานการกัดกร่อนเพิ่มขึ้นและมีค่าการนำไฟฟ้าสูง ในส่วนที่ 2 เป็นการพัฒนาแกรฟีนออกไซด์นาโนคอมพอสิตเคลือบวัสดุรองรับสิ่งทอ เพื่อเพิ่มประสิทธิภาพในการตรวจวัดของตัวรับรู้เชิงสีแบบไม่เจาะผ่านผิวหนัง ซึ่งแกรฟีนออกไซด์นาโนคอมพอสิตถูกรวมเข้ากับวัสดุรองรับสิ่งทอ คือ สิ่งทอผ้าฝ้าย และเส้นด้าย ด้วยวิธีการเคลือบและบิ้อดโดยใช้ลูกกลิ้ง โดยตัวรับรู้บนสิ่งทอชนิดผ้าฝ้ายถูกประดิษฐ์ขึ้น เพื่อตรวจวัดค่าความเป็นกรด-ด่างและแลคเตทในเหงื่อได้สำเร็จ อีกทั้งสามารถนำไปประยุกต์ติดบนผิวหนังเพื่อตรวจวัดค่าความเป็นกรด-ด่างและแลคเตทในเหงื่อขณะออกกำลังกายได้อีกด้วย ซึ่งตัวบ่งชี้ค่าความเป็นกรด-ด่างจะค่อยๆเปลี่ยนสีจากแดงเป็นน้ำเงิน เมื่อค่าความเป็นกรด-ด่างเพิ่มขึ้น ในขณะที่ตัวบ่งชี้ปริมาณแลคเตทจะเปลี่ยนจากไม่มีสีเป็นสีม่วง ซึ่งความเข้มของสีที่เกิดขึ้นจะสัมพันธ์กับความเข้มข้นของแลคเตทที่มีในเหงื่อ โดยตัวรับรู้สามารถบ่งชี้ค่าความเป็นกรด-ด่างของเหงื่อได้ในช่วง 1 ถึง 14 และปริมาณแลคเตทในช่วง 0 ถึง 25 มิลลิโมลาร์ สำหรับวัสดุรองรับสิ่งทอชนิดเส้นด้ายนั้นได้ถูกพัฒนาขึ้นเพื่อตรวจวัดกลูโคสและยูเรียแบบไม่เจาะผ่านผิวหนัง เส้นด้ายเป็นอุปกรณ์ของไหลจุลภาคที่มีความน่าสนใจสำหรับตัวรับรู้ทางชีวภาพ เนื่องจากใช้ปริมาณสารเคมีและสารตัวอย่างน้อย ปฏิกริยาเกิดขึ้นเร็ว และมีความไวสูง ตัวรับรู้บนสิ่งทอเส้นด้ายนี้สามารถใช้บ่งชี้จุดผิดปกติของปริมาณกลูโคส (0.3 มิลลิโมลาร์) และยูเรีย (65 มิลลิโมลาร์) ในเหงื่อได้ ตัวรับรู้นี้อาจจะถูกนำไปรวมกับเสื้อผ้าหรืออุปกรณ์ต่างๆ เพื่อตรวจวัดสารบ่งชี้ทางชีวภาพในเหงื่ออย่างต่อเนื่องและทันที ซึ่งระบบตัวรับรู้บนสิ่งดังกล่าวเป็นแนวทางใหม่สำหรับการตรวจวัดแบบไม่เจาะผ่านผิวหนังในการดูแลสุขภาพ และจะถูกนำไปรวมกับเสื้อผ้าและเครื่องแต่งกายสำหรับผู้ใช้ในอนาคค

สาขาวิชา	วิทยาศาสตร์นาโนและเทคโนโลยี	ลายมือชื่อนิสิต .....
ปีการศึกษา	2561	ลายมือชื่อ อ.ที่ปรึกษาหลัก .....
		ลายมือชื่อ อ.ที่ปรึกษาร่วม .....

# # 5887782620 : MAJOR NANOSCIENCE AND TECHNOLOGY

KEYWORD: Graphene oxide, Electrochemical sensor, Colorimetric sensor, Non-invasive, Sweat sensor

Nadtinan Promphet : Preparation of graphene nanocomposites for anticorrosion and sensors. Advisor: Dr. NADNUDDA RODTHONGKUM, Ph.D. Co-advisor: Prof. Dr. ORAWON CHAILAPAKUL, Ph.D.

This dissertation focused on the development of graphene (GO) nanocomposite coating to improve various substrate properties for the sensor application, which is divided into 2 main parts. The first part is the development of GO incorporated into electroless nickel phosphorus (NiP) coating to improve the properties of metal for electrochemical sensor application. Nickel phosphorus – titanium dioxide sol – reduced graphene oxide (NiP-TiO<sub>2</sub> sol -RGO) coated surface was successfully prepared by one-pot electroless deposition on the steel substrate. The results show that the homogeneously formation of water-repellent RGO film covering on the coated surface leading to improve the corrosion resistance and high electrical conductivity of NiP-TiO<sub>2</sub>-RGO coated steel. The second part is the development of GO nanocomposite coated textile substrates to enhance the analytical performances of non-invasive colorimetric sensor. GO nanocomposite was incorporated on textile substrates including fabric and thread by coating and padding. The cotton fabric based sensor was successfully fabricated for sweat pH and lactate detection and it can directly apply onto the human skin for the simultaneous detection of pH and lactate during the physical exercise. The pH indicator gradually changed from red to blue as the pH increased, whereas the intensity of the purple color increased with the concentration of lactate in the sweat which can indicate the sweat pH in a range of 1-14 and the lactate level of 0-25 mM. As for the textiles, thread has been developed for non-invasive glucose and urea sensor. Thread is a promising microfluidic device for biosensor due to low volume of reagent and sample, fast reaction time and high sensitivity. This sensor can be used to identify the cut-off level of glucose (0.3 mM) and urea (65 mM) in human sweat. This sensor might be incorporated into clothes and accessories for the real-time and continuous monitoring of sweat biomarkers. This platform opens a new approach for non-invasive diagnosis in healthcare and it will be integrated with clothes and apparels for the users in the near future.

Field of Study: Nanoscience and Technology Student's Signature .....

Academic Year: 2018 Advisor's Signature .....

Co-advisor's Signature .....

## ACKNOWLEDGEMENTS

I would like to thank my thesis advisor and co-advisor, Dr. Nadhudda Rodthongkum and Professor Dr. Orawon Chailapakul for their supports and advices.

I would also like to thank to Miss Pranee Rattanawaleedirojn for her comment and suggestion about electroless plating experiment.

I would like to thank to Professor Dr. Juan P. Hinstroza from Cornell University, USA. for his support, encouragement and suggestion for my 8 months exchange student in his research group.

I am thankful to all the committee members, Associate Professor Dr. Vudhichai Parasuk, Assistant Professor Dr. Ratthapol Rangkupan, Assistant Professor Dr. Nutthita Chuankrerkkul, and Assistant Professor Dr. Sarute Ummartyotin for their comments and suggestions.

I am grateful to the financial supports from the financial support from the 100th Anniversary Chulalongkorn University Fund for Doctoral Scholarship and the 90th Anniversary of Chulalongkorn University Fund (Ratchadaphiseksomphot Endowment Fund) and also the Overseas Research Experience Scholarship for Graduate Student.

In addition, I am grateful to all members of my researcher group for their kindness and great friendship.

Finally, I would like to thank my family for their love and support throughout my life.

Nadtinan Promphet

## TABLE OF CONTENTS

	Page
ABSTRACT (THAI).....	iii
ABSTRACT (ENGLISH).....	iv
ACKNOWLEDGEMENTS.....	v
TABLE OF CONTENTS.....	vi
LIST OF FIGURES.....	x
LIST OF TABLES.....	xv
CHAPTER I INTRODUCTION.....	1
1.1 Introduction.....	1
1.2 Objectives.....	2
1.3 Scope of research.....	3
CHAPTER II THEORY AND LITERATURE SURVEY.....	4
2.1 Graphene and its derivatives.....	4
2.1.1 Graphene oxide.....	4
2.1.2 Reduce graphene oxide.....	4
2.2 Bio/Chemical sensors.....	5
2.3 Electrochemical sensor.....	6
2.3.1 Electrode surface modification.....	6
2.3.2 Potentiodynamic polarization.....	9
2.3.3 Cyclic voltammetry.....	10
2.4 Colorimetric sensor.....	10
2.4.1 Enzyme based colorimetric sensor.....	11

2.4.2 Non-invasive textile based colorimetric sensor .....	11
2.4.3 Sensor surface modification .....	12
2.4.3.1 Chitosan .....	12
2.4.3.2 Hydrogels .....	13
2.4.3.3 pH indicator .....	14
2.3 Non-invasive sweat biomarkers for bio/chemical sensor.....	16
2.3.1 Sweat pH.....	16
2.3.2 Lactate.....	16
2.3.3 Glucose.....	17
2.3.4 Urea.....	17
CHAPTER III EXPERIMENTAL .....	18
3.1 Chemicals and reagents.....	18
3.2 Instrument and equipment .....	20
3.3 Preparation of TiO <sub>2</sub> sol and NiP-TiO <sub>2</sub> sol-RGO coated steel surfaces .....	21
3.3.1 Synthesis of TiO <sub>2</sub> sol.....	21
3.3.2 Preparation of electroless NiP-TiO <sub>2</sub> sol-RGO plating bath .....	21
3.3.3 Preparation of NiP-TiO <sub>2</sub> sol-RGO coated steel by electroless plating.....	22
3.3.4 Electrochemical measurement.....	22
3.4 Preparation of textile colorimetric sensor .....	23
3.4.1 Fabrication of cotton fabric based colorimetric sensor for simultaneous sweat pH and lactate.....	23
3.4.1.1 Preparation of the chemical solution for each layer coating step	23
3.4.1.2 Fabrication process of cotton fabric based colorimetric sensor ...	24
3.4.1.3 Standard color chart of sweat pH and lactate sensor.....	25



3.4.1.4	Simultaneous detection of sweat pH and lactate on volunteers	25
3.4.1.5	Testing of the color fade of cotton fabric based sensor.....	25
3.4.2	Fabrication of cotton thread based colorimetric sensor for sweat glucose and urea .....	26
3.4.2.1	Preparation of cotton thread based colorimetric sensor for glucose and urea .....	26
3.4.2.2	Characterization of cotton thread based colorimetric sensor .....	27
3.4.3	Preparation of standard calibration of glucose and urea .....	27
CHAPTER IV	RESULTS AND DISCUSSION .....	28
4.1	Characterization of TiO <sub>2</sub> nanoparticles synthesized by sol-gel method .....	28
4.2	Optimization of NiP-TiO <sub>2</sub> sol-RGO coated surface .....	30
4.2.1	Effect of TiO <sub>2</sub> sol concentration.....	30
4.2.2	Effect of electroless deposition time .....	33
4.2.3	Effect of GO loading .....	35
4.3	Characterization of NiP-TiO <sub>2</sub> sol-RGO nanocomposite coated surface .....	37
4.3.1	Surface morphology characterization.....	37
4.3.2	Surface Wettability characterization.....	38
4.3.3	Corrosion resistance characterization .....	39
4.3.4	Electrical conductivity characterization .....	41
4.3.5	Electrochemical sensor application .....	42
4.4	Cotton fabric based colorimetric sensor for simultaneous sweat pH and lactate.....	43
4.4.1	Physical characterization of different layers of modified cotton .....	43
4.4.2	Chemical characterization of the layers .....	45
4.5	Sensor performance testing .....	46

4.5.1 Standard color chart of textile based pH sensor .....	46
4.5.2 Standard colorimetric chart of textile based lactate sensor .....	47
4.5.3 On-body trial results from volunteers.....	48
4.5.4 Testing the color fade of textile based sensor .....	50
4.6 Thread based colorimetric sensor for simultaneous sweat glucose and urea ..	50
4.6.1 Optimization of thread based colorimetric sensor .....	51
4.6.1.1 Effect of chitosan concentration.....	51
4.6.1.2 Effect of glucose oxidase volume .....	51
4.6.1.3 Effect of the hydrogel structure.....	52
4.6.1.4 Effect of graphene oxide loading.....	53
4.6.1.5 Optimization of phenol red .....	54
4.6.1.6 Optimization of ureases enzyme.....	55
4.7 Physical characterization of different layers of modified cotton thread.....	56
4.8 Chemical characterization of the modified sensing layer .....	58
4.8.1 FT-IR characterization.....	58
4.8.2 XPS characterization.....	58
4.9 Sensor performance testing .....	59
4.9.1 Standard color chart of cotton thread-based glucose sensor .....	59
4.9.2 Standard color chart of cotton thread-based urea sensor .....	60
4.9.3 Simultaneous detection of glucose and urea.....	61
CHAPTER V CONCLUSIONS .....	63
REFERENCES .....	64
VITA.....	75

## LIST OF FIGURES

	Page
<b>Figure 1.1</b> Schematic overview of this dissertation.....	3
<b>Figure 2.1</b> Schematic of GO and RGO formation from G (or graphite).....	5
<b>Figure 2.2</b> Schematic representation of the important component of the chemical sensor .....	5
<b>Figure 2.3</b> Schematic diagram of the electrochemical cell.....	6
<b>Figure 2.4</b> The cross-section SEM images of 1 layer of NiP coating (a) and 2 layers of NiP/NiP-TiO <sub>2</sub> coating (b) and linear sweep voltammograms of 1 layer NiP-TiO <sub>2</sub> electrode (gray line) and 2 layers NiP/NiP-TiO <sub>2</sub> electrode (black line) (c) .....	8
<b>Figure 2.5</b> Schematic experimental potentiodynamic polarization curve (solid curve) and Tafel plot for anodic and cathodic branches (dash curve) .....	9
<b>Figure 2.6</b> Triangular potential waveform (a) and cyclic voltammogram of a reversible redox process (b).....	10
<b>Figure 2.7</b> Schematic of the enzymatic reaction based colorimetric sensor.....	11
<b>Figure 2.8</b> Chemical structure of chitin and chitosan.....	12
<b>Figure 2.9</b> Chemical structure of methyl orange.....	14
<b>Figure 2.10</b> Chemical structure of bromocresol green.....	15
<b>Figure 2.11</b> Chemical structure of phenol red .....	15
<b>Figure 3.1</b> Schematic illustration of the overall of TiO <sub>2</sub> sol and NiP-TiO <sub>2</sub> sol-RGO coated steel surfaces.....	21
<b>Figure 3.2</b> Schematic illustration of a colorimetric sensor pattern design (a) and fabrication process of textile based colorimetric sensor for the simultaneous detection of sweat pH and lactate (b).....	24
<b>Figure 3.3</b> Schematic illustration of fabrication process of cotton thread based colorimetric sensor for the simultaneous detection of glucose and urea .....	27

<b>Figure 4.1</b>	TEM image (a), an electron diffraction pattern (b) and TEM-EDX spectra and of TiO <sub>2</sub> sol solution.....	28
<b>Figure 4.2</b>	TEM image (a), an electron diffraction pattern (b) and TEM-EDX spectra and of TiO <sub>2</sub> sol-GO solution.....	29
<b>Figure 4.3</b>	Photographs of NiP-TiO <sub>2</sub> sol-GO solution before electroless plating (a) and NiP-TiO <sub>2</sub> sol-RGO solution after finishing electroless plating process.....	29
<b>Figure 4.4</b>	Photographs of NiP (a), NiP-TiO <sub>2</sub> sol (b) and NiP-TiO <sub>2</sub> sol-RGO (c) coated steel surfaces .....	30
<b>Figure 4.5</b>	SEM images of NiP-TiO <sub>2</sub> sol-RGO composite coated steel surfaces with different amount of loaded TiO <sub>2</sub> sol ranging from 0 g L <sup>-1</sup> (a), 1.0 g L <sup>-1</sup> (b), 2.0 g L <sup>-1</sup> (c) and 4.0 g L <sup>-1</sup> (d) .....	31
<b>Figure 4.6</b>	Potentiodynamic polarization curves of NiP-TiO <sub>2</sub> sol-RGO coated steel surfaces with the different amount of TiO <sub>2</sub> sol loaded in 3.5 wt% NaCl aqueous solution .....	32
<b>Figure 4.7</b>	SEM images of NiP-TiO <sub>2</sub> sol-RGO coated steel surfaces with different plating times: 15 min (a), 30 min (b) and 45 min (c).....	33
<b>Figure 4.8</b>	Potentiodynamic polarization curves of NiP-TiO <sub>2</sub> sol-RGO composite coating with different plating time in 3.5 wt% NaCl aqueous solution.....	34
<b>Figure 4.9</b>	SEM images of NiP-TiO <sub>2</sub> sol-RGO composite coating with different amount of GO loaded including GO 0 g L <sup>-1</sup> (a), GO 0.5 g L <sup>-1</sup> (b), GO 1.0 g L <sup>-1</sup> (c). .....	35
<b>Figure 4.10</b>	Potentiodynamic polarization curves of NiP-TiO <sub>2</sub> sol-RGO composite coating with different amount GO of loaded in 3.5 wt% NaCl aqueous solution.....	36
<b>Figure 4.11</b>	SEM images of NiP (a), NiP-TiO <sub>2</sub> sol (b) and NiP-TiO <sub>2</sub> sol-RGO (c) composite coated steel surfaces and a SEM image of cross-section (d) and Raman spectrum of NiP-TiO <sub>2</sub> sol-RGO coating (e).....	38

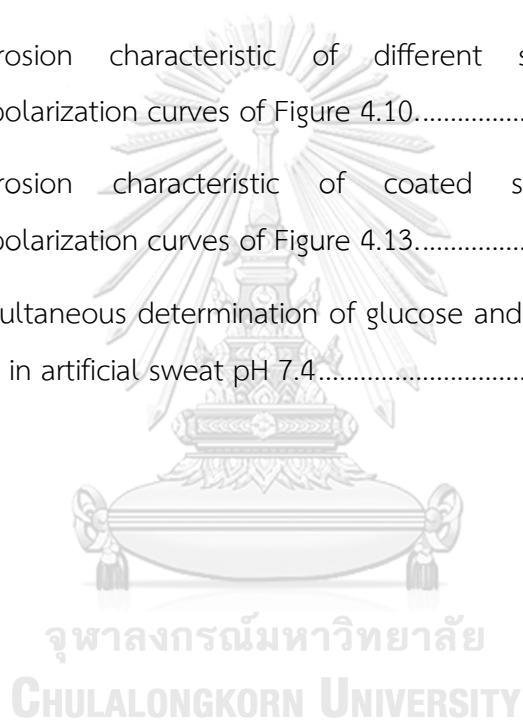
- Figure 4.12** The water drop images and contact angle results of the NiP, NiP-TiO<sub>2</sub> sol and NiP-TiO<sub>2</sub> sol-RGO coated surfaces, respectively. The error bars correspond to the standard deviation obtained from five measurements (n = 5)..... 39
- Figure 4.13** Potentiodynamic polarization curves of NiP (a), NiP-TiO<sub>2</sub> sol (b), and NiP-TiO<sub>2</sub> sol-RGO coated surfaces in 3.5 wt% NaCl aqueous solution ..... 40
- Figure 4.14** Relative conductivity of the NiP, NiP-TiO<sub>2</sub> sol and NiP-TiO<sub>2</sub> sol-RGO coated surfaces, respectively. The error bars correspond to the standard deviation obtained from five measurements (n = 5)..... 41
- Figure 4.15** Cyclic voltammograms of 1.5 mM glucose in 0.1 M NaOH using the unmodified, NiP-TiO<sub>2</sub> sol and NiP-TiO<sub>2</sub> sol-RGO electrodes ..... 42
- Figure 4.16** Photographs of unmodified cotton substrate (a), chitosan/cotton substrate (b), NaCMC-CTAB-indicator dyes/chitosan/cotton substrate (c), NaCMC hydrogel/CMC-CTAB-indicator/chitosan/ cotton substrate (d) and NaCMC hydrogel/CMC-CTAB-indicator/ chitosan/cotton substrate with the hydrophobic barrier (e) ..... 44
- Figure 4.17** FE-SEM images of cotton (a), chitosan/cotton (b), NaCMC-CTAB-indicator dyes/ chitosan (c) and NaCMC hydrogel/ NaCMC-CTAB indicator dyes/ chitosan/cotton (d). ..... 45
- Figure 4.18** FT-IR spectrum of the difference coated cotton layers. .... 46
- Figure 4.19** Standard color charts for textile based pH sensor (a) and L\* a\* b\* color model of pH in 0.1 M PBS solution (b). \* The value of L\* represents brightness (+ = lighter, - = darker) while the a\* and b\* represent the distant along the red-green (+ = redder, - = greener) and blue-yellow (+ = yellower, - = bluer) axis, respectively [108]. The error bars correspond to standard deviation obtained from five measurements (n=5) ..... 47
- Figure 4.20** Standard color charts of textile based lactate sensor in the concentration range of 0, 0.5, 2.5, 12.5 and 25 mM (a) and the plot of lactate

concentration versus the mean grey color intensity (b). The error bars correspond to standard deviation obtained from five measurements (n=5).....	48
<b>Figure 4.21</b> The textile based colorimetric of four volunteers after exercise for 30 minutes .....	49
<b>Figure 4.22</b> Photographs of the textile based sensor with (B)/ without CTAB (A) that soaking in PBS (pH 7.4) solution for 0, 30, and 60 minutes .....	50
<b>Figure 4.23</b> Thread-based sensor with different chitosan concentration (0 – 2 % w/v) at the glucose detection zone of 3 mM glucose. The error bars correspond to standard deviation obtained from five measurements (n=5).....	51
<b>Figure 4.24</b> Thread-based colorimetric sensor with different volume of glucose assay (4 – 16 $\mu$ L) at the glucose detection zone of 3 mM glucose. The error bars correspond to standard deviation obtained from five measurements (n=5) .....	52
<b>Figure 4.25</b> Thread-based sensor modified with chitosan (CS), chitosan hydrogel (CS Hydrogel), chitosan-graphene oxide (CS-GO) and chitosan graphene oxide hydrogel (CS-GO hydrogel) at the glucose detection zone of 3 mM glucose. The error bars correspond to standard deviation obtained from five measurements (n=3) .....	53
<b>Figure 4.26</b> Chitosan-graphene oxide hydrogel modified thread with different concentration of graphene oxide (0 – 0.5 $\text{mg mL}^{-1}$ ) at the glucose detection zone of 3 mM glucose. The error bars correspond to standard deviation obtained from five measurements (n=5).....	54
<b>Figure 4.27</b> Thread-based sensor with different concentration of phenol red (1 – 5 $\text{mg mL}^{-1}$ ) at the urea detection area of 60 and 120 mM urea. The error bars correspond to standard deviation obtained from five measurements (n=5) .....	55
<b>Figure 4.28</b> Thread-based sensor with different concentration of urease enzyme (0.03 – 0.17 $\text{mg mL}^{-1}$ ) at the urea detection zone of 60 and 120 mM urea. The error bars correspond to standard deviation obtained from five measurements (n=5) .....	56

- Figure 4.29** SEM images (low and high magnification) of cotton thread (a, b), chitosan-GO hydrogel coated thread (c, d), chitosan-GO hydrogel-glucose assay coated thread (e, f) and chitosan-GO hydrogel-urea assay coated thread (g, h). ..... 57
- Figure 4.30** FTIR spectra of different sensor layers of thread based colorimetric sensor ..... 58
- Figure 4.31** The XPS spectra of unmodified, chitosan, chitosan-GO hydrogel coated cotton threads ..... 59
- Figure 4.32** Standard color chart of thread-based glucose sensor in the concentration range of 0 – 3 mM (left) and the plot of glucose concentration versus the mean color intensity (right). The error bars correspond to standard deviation obtained from five measurements (n=5)..... 60
- Figure 4.33** Standard color chart of thread-based urea sensor in the concentration range of 0 – 180 mM (left) and the plot of urea concentration versus the mean color intensity (right). The error bars correspond to standard deviation obtained from five measurements (n=5)..... 61
- Figure 4.34** The thread based colorimetric sensor with simultaneous glucose and urea detection at low, medium and high concentration of analyte..... 62

## LIST OF TABLES

	Page
<b>Table 3.1</b> Bath composition and electroless plating condition .....	22
<b>Table 4.1</b> Corrosion characteristic of different surfaces obtained from potentiodynamic polarization curves of Figure 4.6 .....	32
<b>Table 4.2</b> Corrosion characteristics of different surfaces obtained from potentiodynamic polarization curves of Figure 4.8 .....	34
<b>Table 4.3</b> Corrosion characteristic of different surfaces obtained from potentiodynamic polarization curves of Figure 4.10 .....	36
<b>Table 4.4</b> Corrosion characteristic of coated surfaces obtained from potentiodynamic polarization curves of Figure 4.13 .....	40
<b>Table 4.5</b> Simultaneous determination of glucose and urea at low, medium and high concentration in artificial sweat pH 7.4 .....	62





# CHAPTER I

## INTRODUCTION

### 1.1 Introduction

Recently, graphene (G) and its derivatives, such as graphene oxide (GO) or reduced graphene oxide (RGO) have become the materials of interest to improve the analytical performances of bio/chemical sensors due to their unique properties, such as high electrical conductivity, high mechanical strength and large specific surface area [1, 2]. This dissertation focuses on the use of G and its nanocomposite for the development of bio/ chemical sensor (*i.e. electrochemical and colorimetric sensor*).

Electrochemical sensor is a versatile analytical device used for the detection of chemical and biological targets in a wide range of applications, such as food inspection, environmental monitoring and clinical diagnosis owing to its simplicity, rapid response, portability and inexpensiveness [3, 4]. The most important part of electrochemical sensor is a working electrode (sensing electrode), which reacts with the target analytes and then transfers the current and generates the detectable electrical signal. The working electrode is required to be high electrical conductivity, high stability and high corrosion resistance. Thus, design and selection of the suitable working electrode material is crucial since it mainly controls the overall performance of the electrochemical sensor.

Electroless nickel–phosphorus (NiP) coating is a well-known surface coating technique that has been used in various applications due to the high corrosion resistance of the coating. To further improve NiP coating properties, the incorporation of nanomaterials within NiP coating becomes an attractive approach [5, 6]. Recently, G has become the material of interest to integrate with NiP coating. Nonetheless, the direct dispersion of pure G into electroless NiP solution is still an important challenge, TiO<sub>2</sub> sol is selected to use for improvement of the homogeneity of the solution.

Therefore, the first part of this dissertation presents the development of GO incorporated into electroless NiP coating to improve the properties of metal substrate for electrochemical sensor application.

Recently, the non-invasive diagnosis has received a great attention for health monitoring application, because it can reduce the painful and risk factors from invasive diagnosis. In addition, non-invasive can be designed in the miniaturization for the comfortable wearable real-time and continuous monitoring. Textile based non-invasive chemical sensor has gained much attention due to the low-cost, lightweight and flexibility. Moreover, textile based sensor can be easily incorporated with clothes and accessories which can be used to develop wearable sensors. Cotton is outstanding textile substrate due to its natural fiber, high breathability, comfortability, and high absorbency. Two types of textiles including fabric and thread are interesting as a textile based sensor substrates. Thread can be fabricated the microfluidic device by the gap between fibers that generate thread capillary channel to make fluids flow through the thread.

Colorimetric sensor is an interesting analytical technique for self-monitoring because it is easy, inexpensive and the color change can read the signal by the naked eyes; however, the colorimetric sensors are less sensitivity and not easy to distinguish with the naked eyes. Therefore, nanomaterials have been used to improve qualitative measurement by eye. The second part of this research presents the development of GO nanocomposite on textile substrates to enhance the sensor performance for non-invasive colorimetric sensor.

Finally, this sensor is applied to detect the target analytes (*i.e. pH, lactate, glucose and urea*) in sweat sample. Sweat is known to be one type of biofluids comprising not only water but also electrolytes, metabolites, small molecules and proteins. These molecules in sweat contain valuable biological information about human health and they can be easily collected for the analyses by using non-invasive technique. Therefore, sweat is an attractive biofluids used for monitoring of personal's health.

## **1.2 Objectives**

1) To prepare G and its derivatives nanocomposite coated metal and textile substrates for improvement of their physical and chemical properties.

2) To apply these coated steel and textile substrates as the working electrodes in electrochemical sensors and non-invasive colorimetric sensor for targeted analyte detection.

### 1.3 Scope of research

This study will focus on the development of GO nanocomposites coated steel and textile substrates to improve their physical and chemical properties. Then, these GO nanocomposites coated steels and textile substrates will be used as the working electrodes in electrochemical sensors and non-invasive colorimetric sensor, respectively.

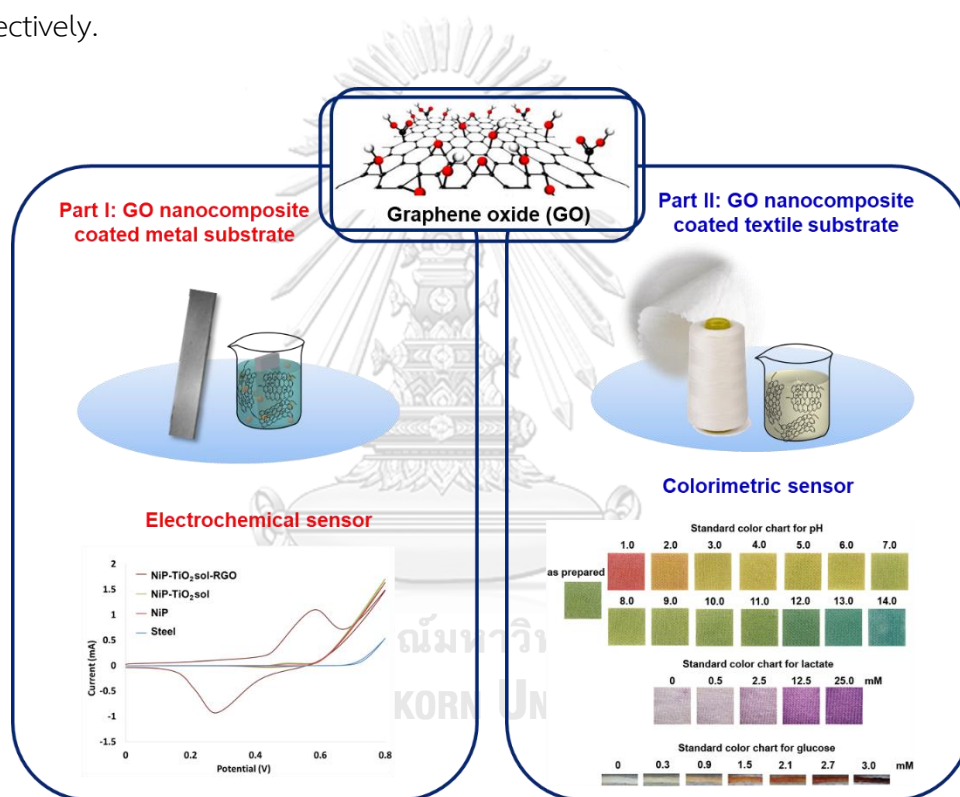


Figure 1.1 Schematic overview of this dissertation.

## CHAPTER II

### THEORY AND LITERATURE SURVEY

#### 2.1 Graphene and its derivatives

Graphene (G) is a two-dimensional single atom thick of  $sp^2$ -hybridized carbon material configured in a hexagonal (honeycomb-like) structure. G has become an interesting material for various applications such biomedical, environmental and food control applications [7].

G and its derivatives (*e.g. graphene oxide (GO), reduce graphene oxide (RGO), nitrogen dope graphene*) are the promising materials used in analytical chemistry, especially for the sensor applications due to its unique properties such as high surface area, excellent electrical conductivity, optical, thermal, catalytic properties [3]. These outstanding properties of G and its derivatives significantly improve the chemical sensor performances. Among all G derivatives, GO and RGO are the most interesting material due to the presence of aromatic ring, free  $\pi-\pi$  electron, and reactive functional group in their structure [7]. Therefore, the used of RGO and GO for sensor development including electrochemical and colorimetric sensors are focused in this dissertation.

##### 2.1.1 Graphene oxide

Graphene oxide (GO) is an oxidizing form of graphene which is an abundance oxygen functional groups (*i.e. hydroxyl (OH), epoxy (C-O-C), carbonyl (C=O) and carboxyl (COOH) species*) in its structure [8]. Therefore, GO is a water soluble with hydrophilic surface functionalities.

##### 2.1.2 Reduce graphene oxide

Reduce graphene oxide (RGO) is a G derivative which is transformation of GO to G by reduction process. The main reduction process that used to convert GO to G are the thermal, chemical and electrochemical processes [9]. In the reduction process, the oxygen function in GO are eliminated to form RGO.

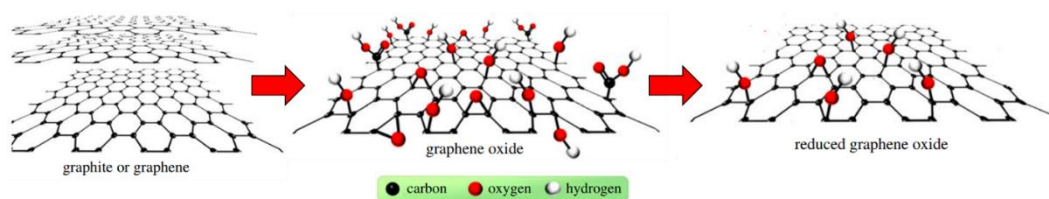


**Figure 2.1** Schematic of GO and RGO formation from G (or graphite) [9].

## 2.2 Bio/Chemical sensors

The definition of bio/chemical sensors is given by The International Union of Pure and Applied Chemistry as “a device that transforms chemical information, ranging from the concentration of a specific sample component to total composition analysis, into an analytically useful signal” [10]. Generally, the chemical sensor consists of two basic functional units: a recognition receptor and a transducer part. The receptor transforms the chemical information into a form of energy which is measured by the transducer, and then it was transformed into a useful analytical signal. If the receptor part of chemical sensors attaches with biological component (e.g. enzyme, antibody, DNA etc.), it is known as a biosensor. The important component of bio/chemical sensor is shown in Figure 2.2. Chemical sensor may be classified according to their transducer including optical device, electrochemical device, mass sensitive device, magnetic device, and thermometric device [11, 12]. Many types of chemical sensor are available, nonetheless, only electrochemical and colorimetric sensor are focused in this dissertation.

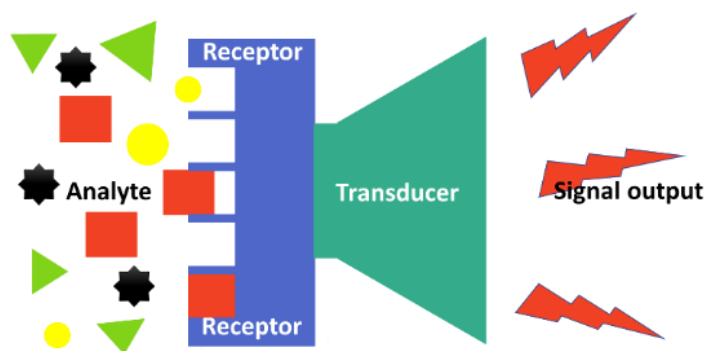


**Figure 2.2** Schematic representation of the important component of the chemical sensor.

## 2.3 Electrochemical sensor

Electrochemical detection is a sensitive analytical technique providing both qualitative and quantitative information. The electrochemical sensor offers wide applications in the detection of chemical and biological targets at the electrode-electrolyte interfaces. This technique is based on oxidation and reduction process of the electroactive species. In general, an electrochemical sensor consists of three-electrode system including working electrode (WE), counter electrode (CE), and reference electrode (RE) immersing in an electrolyte solution as shown in Figure 2.3. This sensor measures the produced electrical signal that is proportional to the analyte concentration. In the detection, working electrode is the most important part because the reaction of interest takes place at this electrode surface. Thus, the electrode should possess high electrical conductivity since the high conductivity of electrode allows for the high electron transfer and thus high sensor sensitivity. Also, the high corrosion resistance of the electrode offers a high stability during storage and allows for severe working conditions. Hence, design of the suitable electrode material is very important for enhancing of the sensor performances.

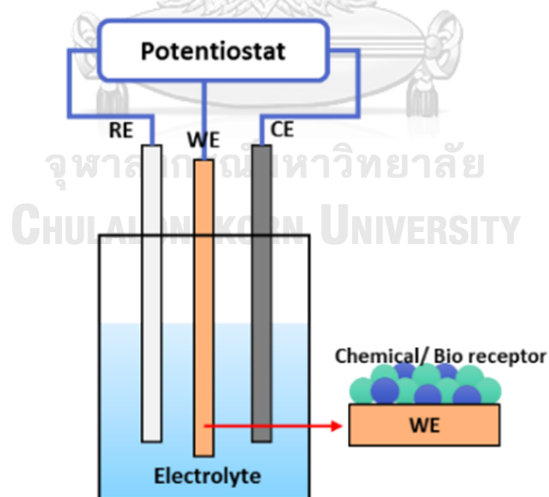


Figure 2.3 Schematic diagram of the electrochemical cell.

### 2.3.1 Electrode surface modification

Electroless plating is a well-known surface coating technique which is a chemical deposition of metal that has been used for various applications. Electroless

nickel-phosphorus (NiP) coating is an autocatalytic deposition of NiP alloy onto the substrate by controlled chemical reduction without applying of the electric current [6, 13]. Electroless NiP coating has been widely used to improve the surface properties of materials, such as corrosion resistance mechanical property and wear resistance of metallic substrates [13-15]. The incorporation of nanomaterials into conventional NiP coating has been developed as the functional surfaces.

Recently, NiP incorporated with titanium dioxide (TiO<sub>2</sub>) coated steel surfaces as working electrodes in electrochemical sensors have been reported.

TiO<sub>2</sub> is a promising nanomaterial for incorporation with NiP due to its own outstanding properties including hardness, corrosion resistance [16-18], wear resistance [18, 19], antimicrobial activity [20], photocatalytic property [21]. However, the self-agglomeration is a crucial problem of nanomaterial fabrication including TiO<sub>2</sub>, leading to poor dispersion and low homogeneity of the coating. To solve this problem, preparation of TiO<sub>2</sub> by using sol-gel method can enhance the dispersion of TiO<sub>2</sub> nanoparticles within NiP composite coating [22].

Shibli, S. *et al.* [23] developed NiP incorporated with TiO<sub>2</sub>-supported nano ruthenium dioxide (RuO<sub>2</sub>) composite coating on mild steel by using electroless plating process. This coating was used as a working electrode in an electrochemical sensor of ethanol. This system exhibited a rapid response time and high sensitivity towards ethanol detection.

Rattanawaleedirojn, P. *et al.* [5] prepared NiP incorporated with nano-TiO<sub>2</sub> sol by electroless deposition. This NiP-TiO<sub>2</sub> coated surface was applied for electrochemical sensor of sorbitol. The incorporation of TiO<sub>2</sub> into composite improved the electrocatalytic activity of NiP. To further improve the electrocatalytic oxidation of sorbitol, 2 layers of NiP/NiP-TiO<sub>2</sub> coating was applied as a working electrode. Figure 2.4 showed SEM images of this coating electrode including 1 layer of NiP-TiO<sub>2</sub> (Figure 2.4a) and 2 layers of NiP/NiP-TiO<sub>2</sub> (Figure 2b). The result of sorbitol detection showed that the 2 layers of composite coating improved electrochemical sensitivity compared with 1 layer of NiP-TiO<sub>2</sub> sol coating (Figure 2.4c).

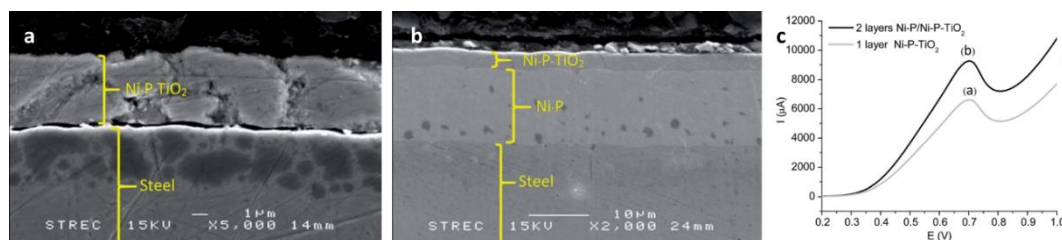


**Figure 2.4** The cross-section SEM images of 1 layer of NiP coating (a) and 2 layers of NiP/NiP-TiO<sub>2</sub> coating (b) and linear sweep voltammograms of 1 layer NiP-TiO<sub>2</sub> electrode (gray line) and 2 layers NiP/NiP-TiO<sub>2</sub> electrode (black line) (c) [5].

Considering about the material properties, high corrosion resistance and high electrical conductivity are the two important factors required for various applications, especially for a working electrode for an electrochemical sensor. Thus, development of composite coating material providing such properties will be focused in this work. G has become a promising material for coating applications owing to its outstanding properties, such as high mechanical property, good barrier property and high electrical conductivity [1]. Several G based composite coatings that used to improve electrical conductivity and corrosion resistance have been previously reported.

Chang, K.-C., et al. [24] developed epoxy/G composite coating by using nanocasting technique. The dispersion of G layers in the composite acts as the barrier to protect gas permeation leading to improved corrosion resistance of this coating.

Liu, X.-W. *et al.* [25] synthesized metal-G hybrid materials via electroless deposition. The metal nanoparticle such as Ag, Au, Pd, Pt and Cu have been synthesized on the G surface with the homogeneous size distribution. Among all, Pt-G hybrid showed good electrocatalytic activity towards methanol oxidation.

Nonetheless, G is not easily dispersed in the NiP electroless bath. Therefore, GO is an attractive material to use for coating application. Owing to the hydrophilic group in their structure that make GO easily dispersed in the NiP electroless solution. However, the presence of hydroxyl and carboxylic group in GO structure leads to reduce catalytic activity and electron transfer process [26, 27]. Therefore, this study focuses on reducing GO to RGO by chemical reduction using one-step NiP electroless plating.



In the application, this coated surface is might be used for the various applications which are required the good corrosion resistance and high electrical conductivity, especially for the electrochemical sensor application.

In this dissertation, two electrochemical methods which are potentiodynamic polarization and cyclic voltammetry are used to study the electrochemical electrode properties.

### 2.3.2 Potentiodynamic polarization

Potentiodynamic polarization is electrochemical technique that used to study corrosion resistance behavior [28]. In the potentiodynamic measurement, the applied potential is increased with time while the current is constantly monitored. The information obtained from the plots of applied potential ( $E_{\text{appl}}$ ) versus log current ( $\log i$ ) that are called Tafel plots (Figure 2.5) [29]. Generally, the highest corrosion resistance of coated steel surface was demonstrated with the highest value of corrosion potential ( $E_{\text{corr}}$ ) and the lowest value of corrosion current ( $i_{\text{corr}}$ ), respectively.

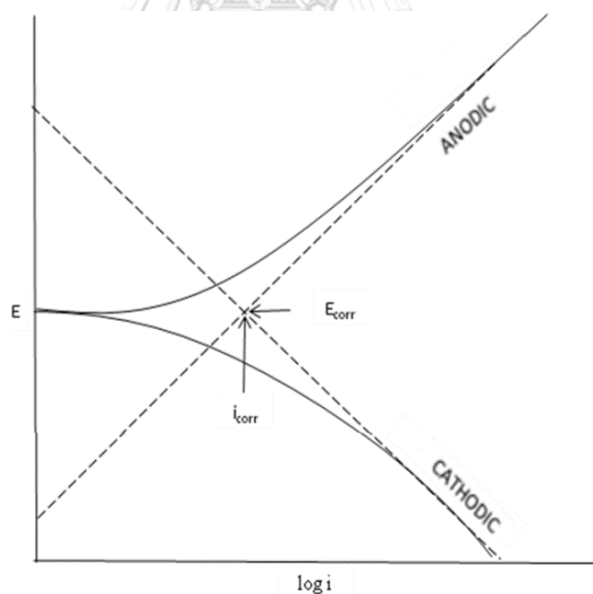


**Figure 2.5** Schematic experimental potentiodynamic polarization curve (solid curve) and Tafel plot for anodic and cathodic branches (dash curve) [30].

### 2.3.3 Cyclic voltammetry

Cyclic voltammetry (CV) is one of the most widely used electrochemical techniques for electroanalytical study. This technique provides useful information about the thermodynamics of redox processes, the kinetics of heterogeneous electron transfer reactions, and coupled chemical reactions or adsorption processes. In this technique, the potential (V) is applied to the working electrode with a triangular potential waveform (Figure 2.6a). The result obtained from the plots of applied potential versus the current is called a cyclic voltammogram (Figure 2.6b) [31].

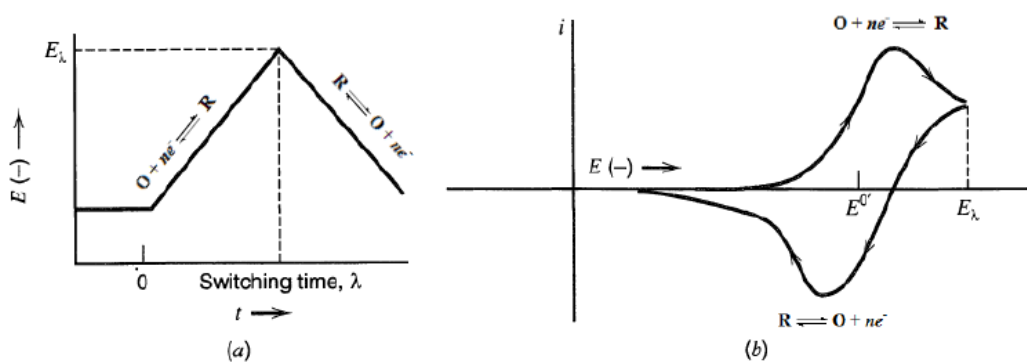


**Figure 2.6** Triangular potential waveform (a) and cyclic voltammogram of a reversible redox process (b) [32].

### 2.4 Colorimetric sensor

A colorimetric sensor is a subset of optical sensors that are device-based on color change when the device detects the target analyte of interest. The colorimetric sensor undergoes a color change that is detectable by a “naked eye” and, more precisely, by the spectrophotometer or colorimetric measurement. This sensor is widely used for medical diagnosis because of its typically inexpensive and easy-to-assess nature. In colorimetric detection, two general signal motifs are considered as (1) a change in intensity at a certain wavelength, thus watching a color appear or fade and (2) monitoring a change in the maximum absorption wavelength, thus watching a color change into a new color [33].

### 2.4.1 Enzyme based colorimetric sensor

The enzymatic reaction based colorimetric sensor is used. The reaction occurs when the analyte react with the specific enzyme that produces hydrogen peroxide ( $H_2O_2$ ). Then, the chromogenic agent are oxidized with  $H_2O_2$  and peroxidase that result in the chromogenic agent change color (Figure 2.7).

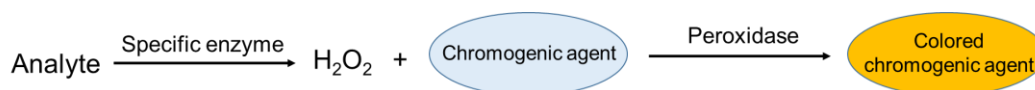


**Figure 2.7** Schematic of the enzymatic reaction based colorimetric sensor.

### 2.4.2 Non-invasive textile based colorimetric sensor

Non-invasive analysis has received a great attention for health monitoring, because of the key advantages of non-invasive analysis that can reduced a painful and risk factors from invasive diagnostic process. In addition, non-invasive can be designed in the miniaturization for the comfortable wearable real-time and continuous monitoring. Several groups have developed wearable sensors devices based on non-invasive analysis with different design such as eyeglass [34], contact lenses [35, 36], wristband [37], mouthguard [1], glove [38], tattoo [39-41]. Those of non-invasive wearable sensors were directly contacted with human body, therefore the wearable sensor substrates shall be light weight, flexible, stretchable, comfortable and biocompatible. Various substrates including paper [42], textile [43-45], synthetic polymer [40, 46, 47] have been used for non-invasive sensor fabrication. Among all, textile has gained much attention for colorimetric sensor due to its low-cost, light-weight, flexibility, and biocompatibility [48]. Moreover, the textile based electrode can be easily incorporated with cloth and accessories which can be used to develop wearable sensor. For wearable sensor in healthcare application, colorimetric sensors have advantages over other techniques (i.e. electrochemical sensor) as easy to used and inexpensive because the colorimetric sensor can read the signal by using a naked eye.

### 2.4.3 Sensor surface modification

To improved sensitivity of textile based colorimetric sensor, GO nanocomposite is used. For example, Figueredo et al. [49] prepared GO modified microfluidic paper based analytical device ( $\mu$ PADs) sensors for glucose colorimetric detection. This modified  $\mu$ PADs enhance the analytical performance of glucose determination. These colorimetric sensors are might be integrated with flexible/stretchable substrates or clothes for wearable sensor application.

#### 2.4.3.1 Chitosan

Recently, the incorporation of chitosan on the sensor surface as enzyme immobilization supporter in colorimetric sensors have been reported.

Chitosan is poly [-(1-4)-2-amino-2-deoxy- $\beta$ -D-glucopyranose] which is a cationic biopolymer obtained from deacetylation process of chitin. The presence of amine and hydroxyl functional groups in their structure that created the functionalization active site [50]. Moreover, chitosan exhibits biocompatible, biodegradable, non-toxic and low cost material [51].

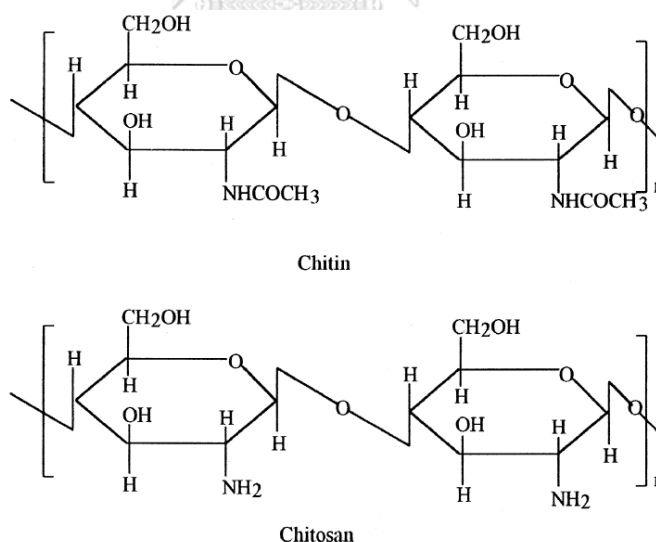


**Figure 2.8** Chemical structure of chitin and chitosan [52].

Gabriel et al. [53] fabricated the  $\mu$ PAD with chitosan for the determination of glucose and uric acid. The modification of chitosan on the paper surface improved the direct electron transfer between an enzyme and a reactive surface leading to

improve the color uniformity and intensity in the glucose and uric acid detection areas. Then, this research group continuously developed this chitosan modified paper based device platform for non-invasive tear glucose monitoring. This device showed high sensitivity and detectability with real sample [54].

Ragavan et al. [50] developed the paper based colorimetric sensor by using chitosan modified paper surface for  $H_2O_2$  detection. This work, chitosan mimicked peroxidase enzyme property to react the chromogenic agent and  $H_2O_2$ . The chitosan based colorimetric sensor showed a high sensitivity for  $H_2O_2$  detection.

Ezati et al. [55] prepared cellulose paper coated chitosan and incorporated alizarin pH indicator for minced beef spoilage monitoring. This cellulose-chitosan-pH indicator based sensor was attached on food packaging. This sensor can distinguish the quality of minced beef during storage.

Xu et al. [56] fabricated a chitosan based pH and  $O_2$  dual sensor. This work, chitosan was used as a matrix for sensitive dye immobilization. This sensor showed good sensitivity for both pH and  $O_2$  detection.

#### 2.4.3.2 Hydrogels

Hydrogel is the hydrophilic polymer with a three dimensional network structure that can absorb a large amount of water or biological fluids [51]. Hydrogel can be divided into chemical and physical gels based on the crosslinking method. Physical gels are formed by molecular self-assembly via ionic or hydrogen bonds while chemical gels are bond by covalent bonds [57]. In bio/chemical sensor application, hydrogels are a protection and coating function of sensor. For example, the hydrogel can be used as sensing element immobilization matrix that is a protection function of hydrogels. Moreover, hydrogel provide good environment to preserve an active and functional structure of enzyme and biomolecule [58]. The used of hydrogels in bio/ chemical sensing application have been reported.

Nam et al. [59] developed colorimetric sensor by using Griess assay immobilized on a hydrogel modified glass fiber strips superimposed the for nitrite ions detection. This colorimetric hydrogel sensor showed a good sensitivity with the detection limit of  $10 \mu M$  and rapid analysis within a few seconds.

Li et al. [60] prepared a label-free urease coupled colloidal crystal hydrogel biosensor by using a monolayer polystyrene array embedded into the urease-modified hydrogel for the urea and urease inhibitor phenyl phosphorodiamidate (PPD) detection. The detection of urea and PPD can be observed by naked eyes. The incorporation of hydrogel enhanced the reproducibility and selectivity of the system.

Lim et al. [61] fabricated hydrogel based on poly(acrylic acid) (PAAc) polymer for hepatitis B core antigen (HBcAg) detection. This hydrogel sensor exhibited specificity of bio-interface towards HBcAg, low cost of operation, rapid and label-free detection.

Zhang et al. [62] prepared GO/ chitosan nanocomposite hydrogel by water evaporation induced self-assembly and subsequent physical crosslink in alkaline solution. This GO/ chitosan hydrogel exhibited strong mechanical properties that act as the promising material for biomedical applications such as artificial muscle, tissue engineering, biosensor and wound dressing.

#### 2.4.3.3 pH indicator

**Methyl orange (MO)** is an orange powder azo dye which contains azo group (two phenyl rings linked by a N=N double bond) in the structure. The color change at pH 3.1 (red) to pH 4.4 (yellow). Thus, at pH of 3.1 or lower the MO molecule is protonated and at pH higher than 4.4 the MO molecule is deprotonated as the sulfonate anion (Figure 2.9) [63, 64].

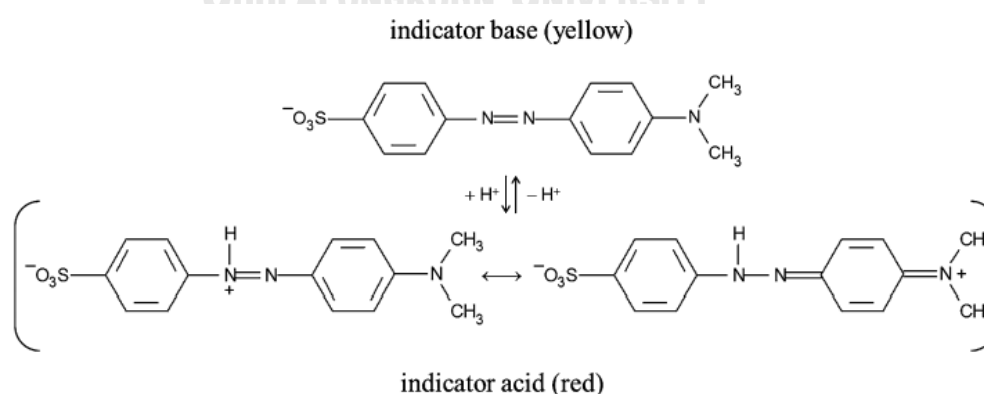


**Figure 2.9** Chemical structure of methyl orange [63].

**Bromocresol green (BCG)** is a sulfonephthalein dye with a green powder in acidic form. The color change at pH 3.8 (yellow) to pH 5.4 (blue-green). Therefore, at pH below 3.8, the BCG is protonated form which is yellow color while at pH above 5.6 the BCG is deprotonated form which is blue-green color (Figure 2.10) [63, 64].

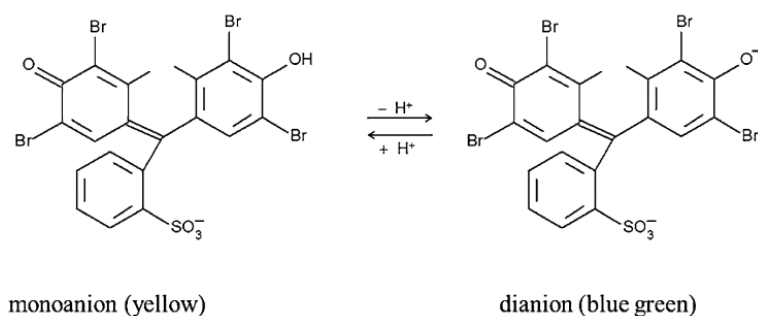


**Figure 2.10** Chemical structure of bromocresol green [63].

**Phenol red** is a red crystals sulfonephthalein dye. The color changing from yellow to red at pH range 6.8 to 8.2. And above pH 8.2, the color change into bright pink. The phenol red structure shows in Figure 2.11 [64].

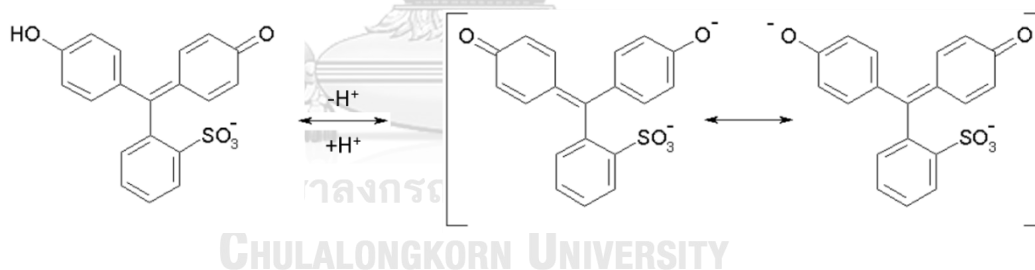


**Figure 2.11** Chemical structure of phenol red [65].

Curto et al. [66] fabricated microfluidic based on ionic liquid polymer gels (ionogel) for sweat pH monitoring. The pH indicators including bromophenol blue, bromocresol green, bromocresol purple and bromothymol blue incorporated retained the pH indicator on the ionogels. This sweat pH colorimetric sensor can detect sweat pH by naked eyes.

Soni et al. [67] developed non-invasive glucose sensor by using co-immobilization of glucose oxidase and pH indicator on filter paper. This glucose

colorimetric sensor can detect the glucose in saliva sample by using smartphone. This glucose colorimetric sensor showed the good sensitivity.

### 2.3 Non-invasive sweat biomarkers for bio/chemical sensor

The body fluids such as tear, saliva, sweat, and skin interstitial fluid contain abundant health information because it is composed of small amounts of substances, such as electrolytes, metabolites, small molecule and protein which are the crucial biomarkers in human body fluids [11, 68]. Sweat is a transparent biological fluid with slightly acidic (pH range 4.0 – 6.8) produced by sweat gland (*i.e. eccrine and apocrine*) [69]. It is composed of water as the main content and small amounts of substances, such as electrolytes (*e.g. sodium, chloride, potassium, calcium*), metabolites (*e.g. lactate, creatinine, glucose, uric acid*), small molecule (*e.g. amino acid, cortisol*), and protein (*e.g. interleukins, tumor necrosis factor, neuropeptide*) which are the crucial biomarkers in human sweat [11, 68]. The human sweat contain abundant health information since the sweat biomarkers can reveal the health status, such as sodium, potassium, lactate, and calcium level in sweat, which are the important indicators of hydration status [70], cystic fibrosis (CF) [71, 72], physical stress and bone mineral loss [73], respectively. Therefore, human sweat is a suitable alternative biological fluid used for monitoring of person's health status. In this dissertation, we focus on four analyte including pH, lactate, glucose and urea.

#### 2.3.1 Sweat pH

Sweat pH is an important parameter to evaluate body condition as the increase of sweat pH can indicate the enhancement of human sweat rate. Furthermore, it has been reported that human sweat pH is directly related to an increase of sodium concentration and hence it can indicate dehydration status [74, 75].

#### 2.3.2 Lactate

Lactate is a biomarker used to evaluate performance as lactate is a direct product of anaerobic metabolism [76]. In the anaerobic process, stored glycogen in the muscles is consumed to produce energy and lactate via cellular metabolism [41, 77]. The accumulation of lactate in the muscles causes soreness, pain and muscle



fatigue [77, 78]. Sweat lactate can also serve as a sensitive marker of tissue viability and may provide warning for pressure ischemia, reflecting the insufficient oxidative metabolism [79].

### 2.3.3 Glucose

Glucose is an important biomarker because it can reveal diabetes disease. Diabetes is one of the most non-communication chronic diseases in Thailand's healthcare system [80]. In 2017, The international Diabetes Federation projects that the number of Thai people with diabetes in 2040 will increase to 8.2 million [80, 81]. Moreover, People with diabetes for a long term cause a risk of complications such as cardiovascular disease, blindness, kidney failure and lower limb amputation. Diabetes complications, especially kidney failure is responsible for huge dialysis cost [82, 83]. Therefore, urea monitoring that indicated the kidney disease is also important.

### 2.3.4 Urea

Urea is the product of nitrogen metabolism in human. Urea can provide the information of renal function and diagnosis of various kidney and liver disorder. The high concentration of urea can cause kidney failure [84, 85].

## CHAPTER III

### EXPERIMENTAL

#### 3.1 Chemicals and reagents

- 3.1.1 Highly concentrated graphene oxide solution (Graphene Supermarket (New York, USA))
- 3.1.2 Titanium diisopropoxide bis(acetylacetonate) (TIAA; 75 wt% in isopropanol) (Sigma-Aldrich (Missouri, USA))
- 3.1.3 1, 3-propanediol (98 wt %) (ACROS organic (New Jersey, USA))
- 3.1.4 Lactic Acid (88 wt %) (Lobachemie (Mumbai, india))
- 3.1.5 Tri-sodium citrate dehydrate (Carlo Erba reagent (Milano, Italy))
- 3.1.6 Ammonium sulphate, nickel (II) sulphate (Carlo Erba reagent (Milano, Italy))
- 3.1.7 Sodium hypophosphite, absolute ethanol (Carlo Erba reagent (Milano, Italy))
- 3.1.8 Hydrochloric acid (Carlo Erba reagent (Milano, Italy))
- 3.1.9 Sodium hydroxide pellets, isopropanol (Ajax Finechem (New South Wales, Australia))
- 3.1.10 Thiourea (Ajax Finechem (New South Wales, Australia))
- 3.1.11 Scoured and bleached knitted cotton fabric (163 g/m<sup>2</sup>) (Sinsaene Co.,Ltd (Bangkok, Thailand))
- 3.1.12 Screen-printed ink (expantex ink) (Chiyaboon brother group Co., Ltd (Bangkok, Thailand))
- 3.1.13 Candle wax (Somjai Co., Ltd (Bangkok, Thailand))
- 3.1.14 Chitosan from squid pen (DD = 85%, Mw 800,000) (Biolifeland (Bangkok, Thailand))
- 3.1.15 Sodium carboxymethylcellulose (NaCMC) (Mw 250,000) (Sigma-Aldrich (St. Louis, MO, USA))
- 3.1.16 Phosphate buffer saline (PBS) (Sigma-Aldrich (St. Louis, MO, USA))
- 3.1.17 Bromocresol green (Sigma-Aldrich (St. Louis, MO, USA))
- 3.1.18 Methyl orange (Sigma-Aldrich (St. Louis, MO, USA))

- 3.1.19 Cetyltrimethylammonium bromide (CTAB) (Sigma-Aldrich (St. Louis, MO, USA))
- 3.1.20 Lactate oxidase (LOx) (from *Aerococcus*) (Sigma-Aldrich (St. Louis, MO, USA))
- 3.1.21 Horseradish peroxidase (HRP) (Sigma-Aldrich (St. Louis, MO, USA))
- 3.1.22 4-aminoantipyrin (4-AAP) (Sigma-Aldrich (St. Louis, MO, USA))
- 3.1.23 N-Ethyl-N-(2-hydroxy-3-sulfoethyl)-3-methylaniline, sodium salt, dihydrate (TOOS) (Sigma-Aldrich (St. Louis, MO, USA)).
- 3.1.24 Aluminium chloride ( $AlCl_3$ ) was obtained from Ajax Finechem (New South Wales, Australia).
- 3.1.25 Acetic acid (Carlo Erba reagent (Milano, Italy))
- 3.1.26 Citric acid (Carlo Erba reagent (Milano, Italy))
- Part II: GO nanocomposite coated textile substrate for colorimetric sensor
- 3.1.27 Cotton thread (D-M-C®/BLANC) (Bangkok, Thailand)
- 3.1.28 candle wax (Bangkok, Thailand)
- 3.1.29 Glucose Oxidase from *Aspergillus niger*, Type II,  $\geq 15,000$  units/g solid (GOx) (Sigma-Aldrich (St. Louis, MO, USA))
- 3.1.30 Peroxidase from horseradish (HRP) (Sigma-Aldrich (St. Louis, MO, USA))
- 3.1.31 Phosphate buffered saline tablet (PBS) (Sigma-Aldrich (St. Louis, MO, USA))
- 3.1.32 D-(+)-Trehalose dihydrate (Sigma-Aldrich (St. Louis, MO, USA))
- 3.1.33 Potassium iodide (KI) (Sigma-Aldrich (St. Louis, MO, USA))
- 3.1.34 Urea (Sigma-Aldrich (St. Louis, MO, USA))
- 3.1.35 Urease from *Canavalia ensiformis* (Jack bean) (Sigma-Aldrich (St. Louis, MO, USA))
- 3.1.36 Phenol red (Sigma-Aldrich (St. Louis, MO, USA))
- 3.1.37 D-(+)-Glucose (99.5%) (Sigma-Aldrich (St. Louis, MO, USA))
- 3.1.38 Chitosan (medium molecular weight) (Sigma-Aldrich (St. Louis, MO, USA))

### 3.2 Instrument and equipment

- 3.2.1 JEM-2100 transmission electron microscope (TEM) (Japan Electron Optics Laboratory Co., Ltd, Japan)
- 3.2.2 JSM-6400 field emission scanning electron microscope (Japan Electron Optics Laboratory Co., Ltd, Japan)
- 3.2.3 200-k1 goniometer (Rame-hart Instrument, USA) using a static sessile drop method.
- 3.2.4 The 4-point probe (2400-C Keithley Instruments, Inc. USA)
- 3.2.5  $\mu$ AUTOLAB Type III potentiostat (Metrohm Siam Company Ltd.)
- 3.2.6 JSM-7610F field emission scanning electron microscope (FESEM) with energy dispersive spectroscopy capabilities (Japan Electron Optics Laboratory Co., Ltd, Japan)
- 3.2.7 Fourier transform infrared spectroscopy (PerkinElmer Spectrum One LabX, USA)
- 3.2.8 Portable spectrophotometer (Datacolor CHECK3, Datacolor, USA)
- 3.2.9 Scanning electron microscope and energy dispersive X-ray spectrometer (SEM-EDS (JSM-IT500HR, Japan Electron Optics Laboratory Co., Ltd, Japan)).
- 3.2.10 X-ray photoelectron spectroscopy (XPS (Axis ultra DLD, Kratos)).

## Part I: GO nanocomposite coated metal substrate for electrochemical sensor

### 3.3 Preparation of $\text{TiO}_2$ sol and NiP- $\text{TiO}_2$ sol-RGO coated steel surfaces

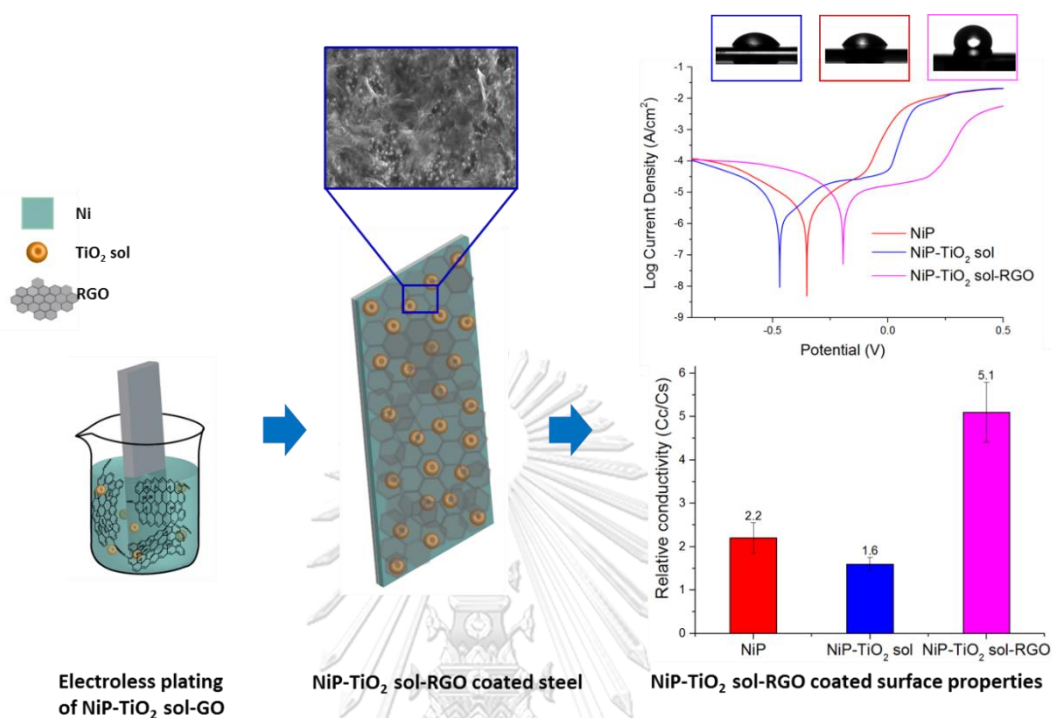


**Figure 3.1** Schematic illustration of the overall of  $\text{TiO}_2$  sol and NiP- $\text{TiO}_2$  sol-RGO coated steel surfaces

#### 3.3.1 Synthesis of $\text{TiO}_2$ sol

The method used for preparation of  $\text{TiO}_2$  sol was previously described [86, 87]. Initially, 0.025 mol of TIAA and 0.025 mol of 1,3 propanediol were mixed together and refluxed at  $85\text{ }^\circ\text{C}$  for 60 min with continuous magnetic stirring. Then, the obtained solution was adjusted to a final volume of 25 mL by isopropanol. Finally, the obtained 1 M of  $\text{TiO}_2$  sol was kept as a stock solution.

#### 3.3.2 Preparation of electroless NiP- $\text{TiO}_2$ sol-RGO plating bath

Initially,  $\text{TiO}_2$  sol was added into deionized water and then sonicated at a room temperature of  $30\pm 2\text{ }^\circ\text{C}$  for 10 min. Then,  $\text{TiO}_2$  sol and GO solution were mixed together by an ultrasonicator for 30 min. The  $\text{TiO}_2$  sol-GO solution was used to prepare an electroless NiP solution. The preparation details of electroless NiP solution has been described in the previous report [87]. The electroless bath

composition is shown in Table 3.1. The complexing agent (lactic acid), ammonium sulphate, nickel sulphate, thiourea and sodium hypophosphite were sequentially added into TiO<sub>2</sub> sol-GO solution. Then, pH of the NiP-TiO<sub>2</sub> sol-GO solution was adjusted to 6.5 using 10% sodium hydroxide solution and sonicated for 2 h prior to use.

**Table 3.1** Bath composition and electroless plating condition.

Bath composition	Electroless plating condition
TiO <sub>2</sub> sol	0, 1, 2, 4 g L <sup>-1</sup> *
GO	0, 0.1, 0.5, 1 g L <sup>-1</sup>
Lactic acid	40.5 g L <sup>-1</sup>
Ammonium sulphate (NH <sub>4</sub> ) <sub>2</sub> SO <sub>4</sub>	30 g L <sup>-1</sup>
Nickel (II) sulphate (NiSO <sub>4</sub> ·6H <sub>2</sub> O)	39.5 g L <sup>-1</sup>
Thiourea	0.8 ppm
Sodium hypophosphite (NaH <sub>2</sub> PO <sub>2</sub> ·H <sub>2</sub> O)	20 g L <sup>-1</sup>
Plating time	15, 30, 45 min
pH	6.5
Bath temperature	80±2 °C

\* The concentration of TiO<sub>2</sub> sol in g L<sup>-1</sup> calculated from a molecular weight of TiO<sub>2</sub>.

### 3.3.3 Preparation of NiP-TiO<sub>2</sub> sol-RGO coated steel by electroless plating

The steel substrate (20 x 20 x 2 mm<sup>3</sup>) was mechanically polished by 1200-grit abrasive SiC paper, degreased with 10% NaOH solution at 60±2 °C for 10 min and pickled in 14% HCl solution at a room temperature for 10 min and rinsed with deionized water. The as prepared steel substrate was immersed into electroless NiP-TiO<sub>2</sub> sol-RGO solution bath at a temperature of 80±2 °C with continuous magnetic stirring. After the electroless deposition process, the NiP-TiO<sub>2</sub> sol-RGO coated steel was thoroughly rinsed with deionized water and air dried. The obtained coated steel surfaces were kept in the desiccator at a room temperature prior to use.

### 3.3.4 Electrochemical measurement

All the electrochemical measurements were performed on a μAUTOLAB Type III potentiostat (Metrohm Siam Company Ltd.) controlled with General Purpose

Electrochemical System (GPES) software. A three electrode system consists of Pt wire as a counter electrode, Ag/AgCl as a reference electrode and a coated surface steels as a working electrode. The corrosion resistance of the coated steel was studied by potentiodynamic polarization (Tafel plot) measurement using 3.5 wt% NaCl solution with the scanning potential in a range of - 0.8 to + 0.5 V at a scan rate of 100 mV s<sup>-1</sup>.

## Part II: GO nanocomposite coated textile substrate for colorimetric sensor

### 3.4 Preparation of textile colorimetric sensor

As for this section, the colorimetric sensor was prepared with two types of textiles including fabric and thread.

#### 3.4.1 Fabrication of cotton fabric based colorimetric sensor for simultaneous sweat pH and lactate

Figure 3.2 shows the design (Figure 3.2a) and the fabrication process (Figure 3.2b) of sweat pH and lactate colorimetric sensor.

##### 3.4.1.1 Preparation of the chemical solution for each layer coating step

###### *Chitosan solution*

2% w/v chitosan was dissolved in 1% v/v acetic acid under the continuous magnetic stirring for overnight. Then, 5%w/w citric acid was added into the chitosan solution.

###### *Mixed indicator dye*

1%w/v Bromocresol green (BCG) and 1%w/v methyl orange (MO) were dissolved in 5%w/v ethanol and deionized water, respectively. Then, BCG and MO were mixed at 1:1 ratio under continuous stirring for 15 minutes and then 0.5% CTAB was added into the mixed indicator under continuous stirring for 15 minutes. The as-prepared indicator-CTAB solution was used to dissolve 2.5%w/v NaCMC for overnight. Next, 5%w/w citric acid was added to NaCMC-CTAB-indicator solution.

###### *CMC solution*

2.5%w/v Sodium carboxymethyl cellulose (NaCMC) was dissolved in deionized water under continuous magnetic stirring for overnight.

### *Lactate colorimetric assay*

This lactate assay solution contains 1 mg mL<sup>-1</sup> HRP, 50 mM 4-AAP, 10 mM TOOS and 50 unit mL<sup>-1</sup> LOx.

#### *3.4.1.2 Fabrication process of cotton fabric based colorimetric sensor*

The chitosan solution was used to coat on the cotton substrate and padding by padding machine. The wet cotton fabric was dried at 100 °C for 180 sec and then was cured at 180 °C for 30 sec. The second layer, the detection area of the sweat pH sensor was fabricated via screen-printing. The mixture of two indicator dyes was screen-printed on the cotton substrate which was previously coated with chitosan. The substrate was cured at 170 °C for 150 sec. For the third layer, NaCMC was coated onto the NaCMC-CTAB-indicator/ chitosan coated cotton substrate. The substrate was immersed into AlCl<sub>3</sub> to create a NaCMC hydrogel structure via chemical crosslinking. After assembly of the three layers, the detection area for pH was soaked in deionized water 3 times to eliminate the excess of indicator dyes and dried at 100 °C for 300 sec. A hydrophobic material was screen-printed onto the coated textile to separate channel between the pH and the lactate detection zones. To fabricate lactate detection area, 50 μL of lactate assay was spotted onto the coated cotton substrate

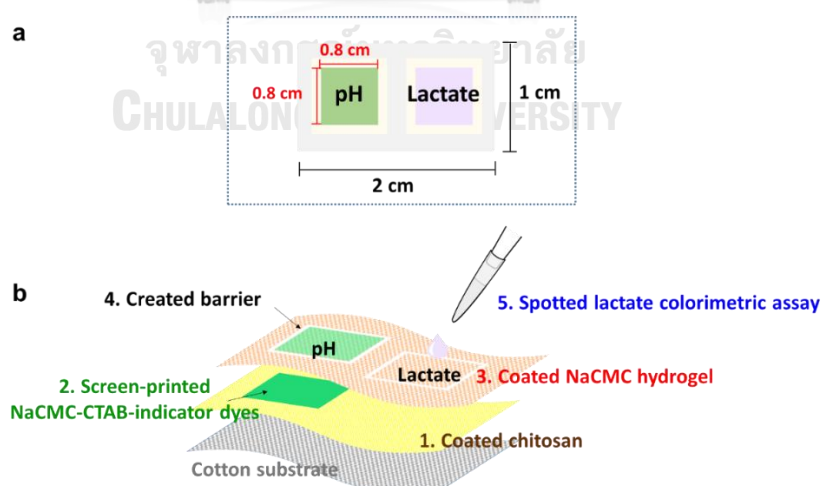


**Figure 3.2** Schematic illustration of a colorimetric sensor pattern design (a) and fabrication process of textile based colorimetric sensor for the simultaneous detection of sweat pH and lactate (b).



#### *3.4.1.3 Standard color chart of sweat pH and lactate sensor*

To prepare standard calibration charts of pH and lactate, phosphate buffer saline (PBS) with varying pH values (pH 1 to pH 14) and lactate concentrations were prepared. The standard solutions were dropped in the pH and the lactate detection areas and the color changes were captured using a camera. The color was quantified using a portable spectrophotometer and ImageJ software.

The ImageJ software was used to make the standard calibration curve of lactate sensor. For this software, the image of color change was transfers into grey color (32-bit). Then, the 32-bit grey scale of the image was inverted. Since, the dark spot in grayscale give the lower value than bright spot. The calibration of these values will be a negative slope. Therefore, this image was inverted to get a positive slope. Then, the invert image was measured and obtained the mean color intensity value. Finally, the lactate calibration curve was obtained from the linear plot of concentration versus mean color intensity value.

#### *3.4.1.4 Simultaneous detection of sweat pH and lactate on volunteers*

Textile based sweat pH and lactate sensor was combined with plaster and directly patch onto the human skin before exercise. After that, the portable spectrometer was used to analyte the pH and lactate values of this textile sensor. Moreover, this sensor can be readily read by the naked eyes by comparing with the standard color chart.

#### *3.4.1.5 Testing of the color fade of cotton fabric based sensor*

The color fade of textile based sensor was studied by soaking the as prepared sensor in PBS (pH 7.4) solution for 0, 30, and 60 minutes. The color fade of textile based sensor was observed and captured.

### 3.4.2 Fabrication of cotton thread based colorimetric sensor for sweat glucose and urea

#### 3.4.2.1 Preparation of cotton thread based colorimetric sensor for glucose and urea

Figure 3.3 shows the sensor fabrication process. Firstly, GO was dispersed in 1% w/v acetic acid by using an ultrasonicator for 30 min. The chitosan was dissolved in GO solution under continuous magnetic stirring. This solution was used to coat thread by soaking for 1 hr and air dried for 1 hr. Then, the coated thread was soaked in 1% NaOH for 1 hr and thoroughly rinsed with the deionized water and air dried [62].

To prepare the detection area, two pieces of the coated threads were used and then the hydrophobic area was created at the end of the coated thread by wax dipping. The glucose and lactate detection zones were prepared individually on each piece of the coated thread. For glucose detection, 4  $\mu\text{L}$  of mixed enzymatic solution (GOx: HRP; 120 : 30 unit  $\text{mL}^{-1}$  in 0.1 M PBS, pH 6) was spotted on the glucose detection zone of the coated thread and dried at the room temperature for 15 min. Then, the 4  $\mu\text{L}$  of chromogenic substrate (0.6 M KI and 0.3 M trehalose in DI water) was spotted on the glucose detection zone and dried at the room temperature for 15 min [88]. For urea detection, 4  $\mu\text{L}$  of urease (33.75 mg  $\text{mL}^{-1}$  in 0.1 M PBS, pH 7.4) was spotted on the urea detection zone and dried at the room temperature for 15 min. Then, 4  $\mu\text{L}$  of phenol red (2 mg  $\text{mL}^{-1}$  in DI water) was spotted on the urea detection zone and dried at room temperature for 15 min [85]. Then, the glucose and urea were combined together to use for the simultaneous detection.

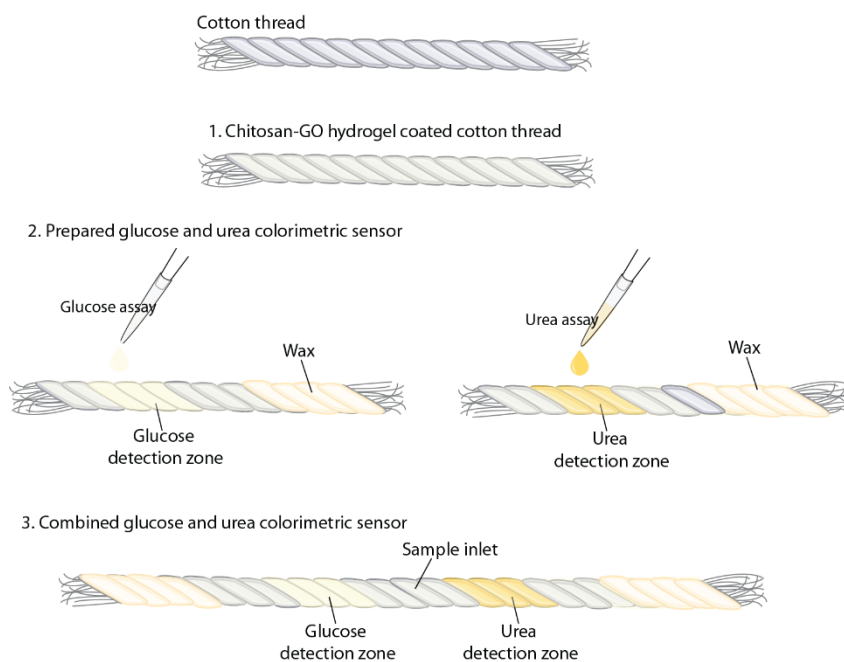


**Figure 3.3** Schematic illustration of fabrication process of cotton thread based colorimetric sensor for the simultaneous detection of glucose and urea.

#### 3.4.2.2 Characterization of cotton thread based colorimetric sensor

The surface morphology of thread based sensor was characterized by a scanning electron microscope and energy dispersive X-ray spectrometer (SEM-EDS (JSM-IT500HR, Japan Electron Optics Laboratory Co., Ltd, Japan)). The chemical modification of thread sensors was investigated by fourier transform infrared spectroscopy (FTIR (PerkinElmer Spectrum One LabX, USA)) was carried out in a range of  $400\text{-}4000\text{ cm}^{-1}$  and X-ray photoelectron spectroscopy (XPS (Axis ultra DLD, Kratos)).

#### 3.4.3 Preparation of standard calibration of glucose and urea

To prepare the standard calibration chart of glucose and urea, various concentration of glucose and urea were prepared in 0.1 M PBS. The standard solution was dropped in glucose and urea detection areas. The color change was captured by using a mobile phone camera with the macro lens. The standard calibration curve for semi-quantitative, the photo of color change was analyzed by an ImageJ software (National Institute of Health, USA) to measure mean grey color intensity. Then, the grey color intensity was plotted versus the analyte standard concentration.

## CHAPTER IV

### RESULTS AND DISCUSSION

#### Part I: GO nanocomposite coated metal substrate for electrochemical sensor

##### 4.1 Characterization of TiO<sub>2</sub> nanoparticles synthesized by sol-gel method

In this study, TiO<sub>2</sub> nanoparticles were synthesized by sol-gel method as same as the previous study [87]. The morphology of TiO<sub>2</sub> sol characterized by TEM is shown in Figure 4.1a. A TEM image demonstrates the uniform spherical shape of TiO<sub>2</sub> nanoparticle with the size distribution in a range of 70-180 nm and TiO<sub>2</sub> nanoparticles show homogeneous dispersion without aggregation. An electron diffraction pattern of TiO<sub>2</sub> nanoparticle is illustrated an amorphous diffraction pattern (Figure 4.1b) due to the organic branch in TiO<sub>2</sub> sol structure. The characteristic peaks of TiO<sub>2</sub> from TEM-EDX analysis (Figure 4.1c) indicated the TiO<sub>2</sub> nanoparticles was successfully prepared.

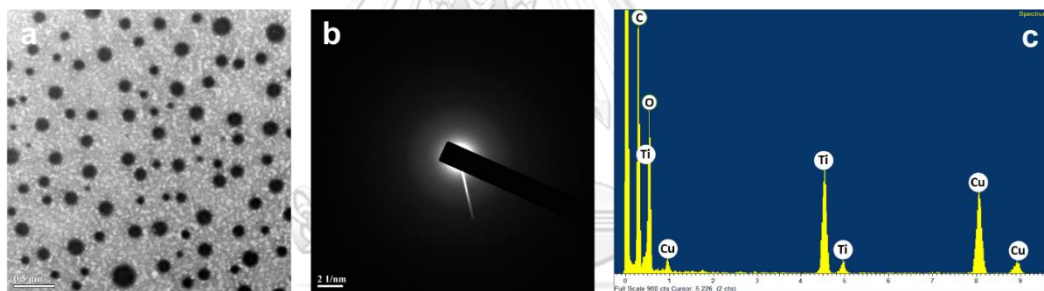


**Figure 4.1** TEM image (a), an electron diffraction pattern (b) and TEM-EDX spectra and of TiO<sub>2</sub> sol solution.

TiO<sub>2</sub> sol was used incorporation with GO in nickel plating solution in a one-pot electroless process. The NiP-TiO<sub>2</sub> sol-GO solution shows the more homogenous dispersion compared with the NiP-GO solution. A TEM image of TiO<sub>2</sub> sol-GO solution showed the intercalation of TiO<sub>2</sub> sol in the GO layers (Figure 4.2a). This suggested that the TiO<sub>2</sub> sol acts like a stabilizing agent to improve GO dispersion in NiP solution, leading to increase preparation reproducibility of surface coating. An electron diffraction pattern of TiO<sub>2</sub> sol-GO solution (Figure 4.2b) showed a hexagonal pattern, a crystalline ordered characteristic of GO sheet [89]. The TEM-EDX analysis of TiO<sub>2</sub> sol-GO solution (Figure 4.2c) showed the characteristic peaks similar to the TiO<sub>2</sub> sol.

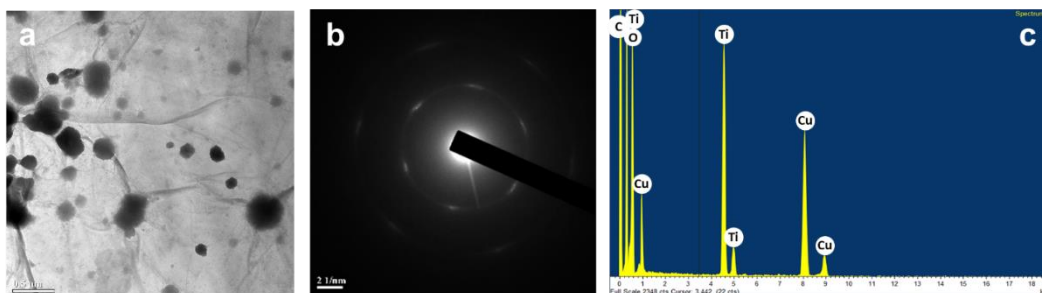


**Figure 4.2** TEM image (a), an electron diffraction pattern (b) and TEM-EDX spectra and of  $\text{TiO}_2$  sol-GO solution.

In the electroless plating process, GO can be reduced by both chemical reduction and thermal reduction. It has been previously reported that sodium hypophosphite ( $\text{NaH}_2\text{PO}_2$ ) is capable of reducing both  $\text{Ni}^{2+}$  and GO [6]. Furthermore, GO can be reduced by thermal reduction at the electroless plating bath temperature [90]. To confirm that GO is completely reduced to RGO, we can obviously notice the immiscible RGO sheets floated onto the surfaced of electroless plating solution after electroless process about 3 minutes (Figure 4.3) due to the hydrophilic property of GO turn to hydrophobic property of RGO.

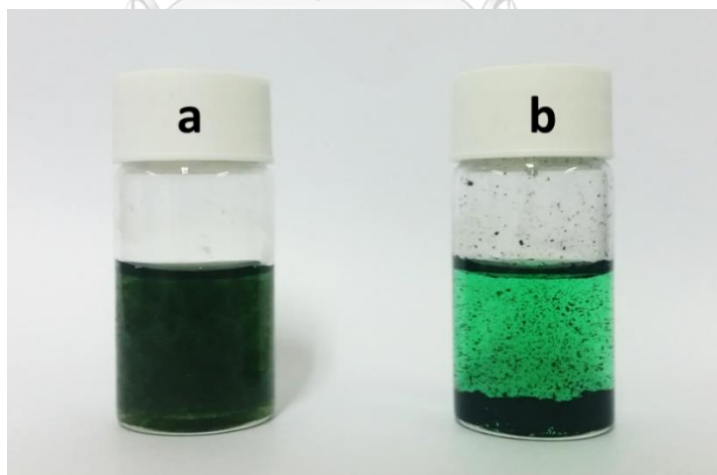


**Figure 4.3** Photographs of  $\text{NiP-TiO}_2$  sol-GO solution before electroless plating (a) and  $\text{NiP-TiO}_2$  sol-RGO solution after finishing electroless plating process.

## 4.2 Optimization of NiP-TiO<sub>2</sub> sol-RGO coated surface

The NiP, NiP-TiO<sub>2</sub> sol, NiP-TiO<sub>2</sub> sol-GO solutions were used for electroless plating onto the steel surface. The important parameters controlling the coated surface properties including the amount of TiO<sub>2</sub> sol, electroless plating time, amount of GO were investigated and optimized. In the preliminary study, the electrochemical measurement was used to evaluate the corrosion resistant and SEM was used to investigate the surface morphology of the nanocomposite coated surfaces. The photographs of coated surfaces obtained from electroless plating of NiP, NiP-TiO<sub>2</sub> sol and NiP-TiO<sub>2</sub> sol-GO solution were shown in Figure 4.4a-c. The results showed that both surfaces of NiP (Figure 4.4a) and NiP-TiO<sub>2</sub> sol (Figure 4.4b) were bright and shiny, whereas the NiP-TiO<sub>2</sub> sol-RGO coating (Figure 4.4c) showed black with non-shiny surface due to G coverage on the surface. However, in the experiment, the electroless plating of TiO<sub>2</sub> sol-GO solution cannot be coated on the steel. This result revealed that NiP electroless plating play an important role in the TiO<sub>2</sub> sol-GO co-deposition onto steel surface.

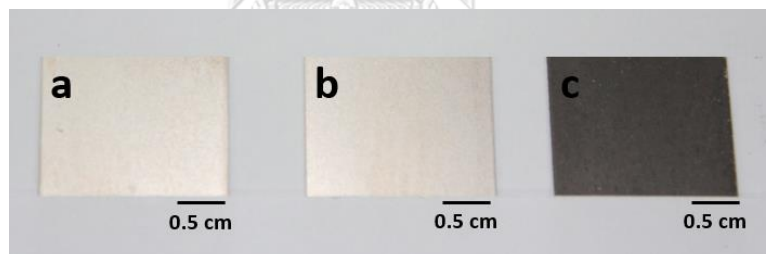


**Figure 4.4** Photographs of NiP (a), NiP-TiO<sub>2</sub> sol (b) and NiP-TiO<sub>2</sub> sol-RGO (c) coated steel surfaces.

### 4.2.1 Effect of TiO<sub>2</sub> sol concentration

From the previous mention, TiO<sub>2</sub> sol play an importance role on the GO dispersion. Therefore, an optimal proportion of TiO<sub>2</sub> sol was studied as the first parameter. Amount of TiO<sub>2</sub> sol was optimized from 0-4.0 g L<sup>-1</sup> with GO 0.5 g L<sup>-1</sup> and 45 minutes of coating time. The result showed that the concentration of TiO<sub>2</sub> sol at 1.0 g L<sup>-1</sup> was an optimal condition for electroless NiP plating. Due to the high uniformity and high homogeneity of the surface compared to the other

concentration of  $\text{TiO}_2$  sol (Figure 4.5). It has been previously reported that the interaction between  $\text{TiO}_2$  nanoparticles and GO sheet prevents the reaggregation of GO sheets [91]. Therefore, these results suggested that the intercalation of  $\text{TiO}_2$  sol in GO layers lead to enhance GO dispersion and prevent self-agglomeration of GO sheets.

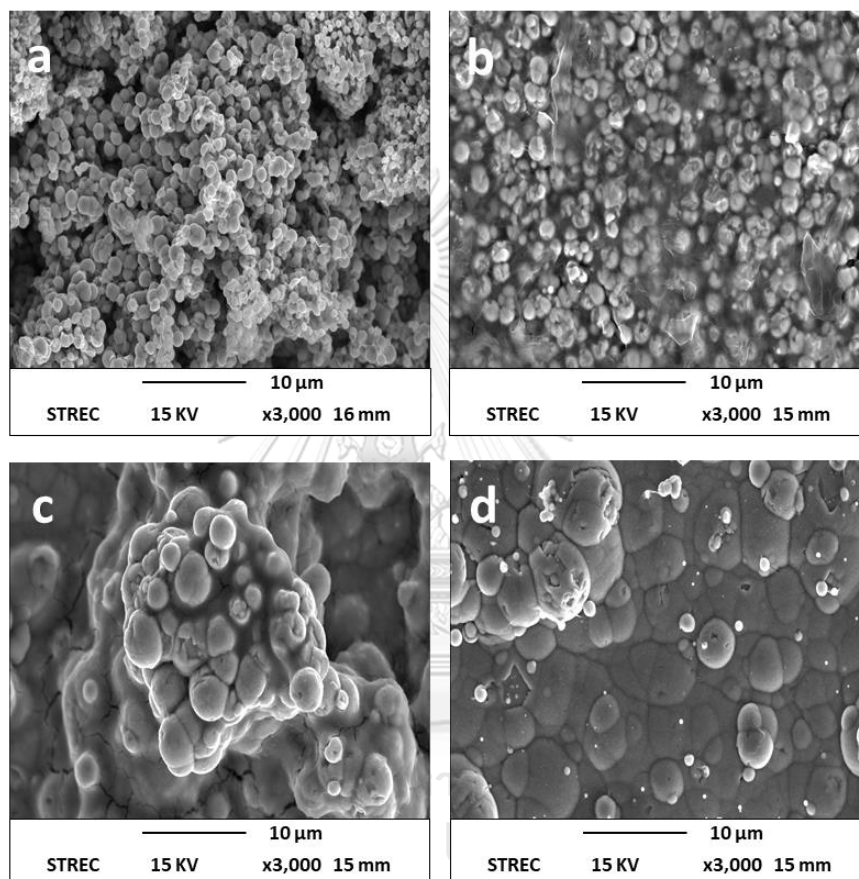


**Figure 4.5** SEM images of NiP- $\text{TiO}_2$  sol-RGO composite coated steel surfaces with different amount of loaded  $\text{TiO}_2$  sol ranging from  $0 \text{ g L}^{-1}$  (a),  $1.0 \text{ g L}^{-1}$  (b),  $2.0 \text{ g L}^{-1}$  (c) and  $4.0 \text{ g L}^{-1}$  (d).

Moreover, the results obtained from potentiodynamic polarization measurements show that the concentration of  $\text{TiO}_2$  sol  $1.0 \text{ g L}^{-1}$  provide the passive layers to protect the surfaces from corrosion (Figure 4.6). The  $E_{\text{corr}}$  and  $I_{\text{corr}}$  values from polarization curves are shown in Table 4.1. Therefore,  $1.0 \text{ g L}^{-1}$  of  $\text{TiO}_2$  sol loading was selected for the further experiments.

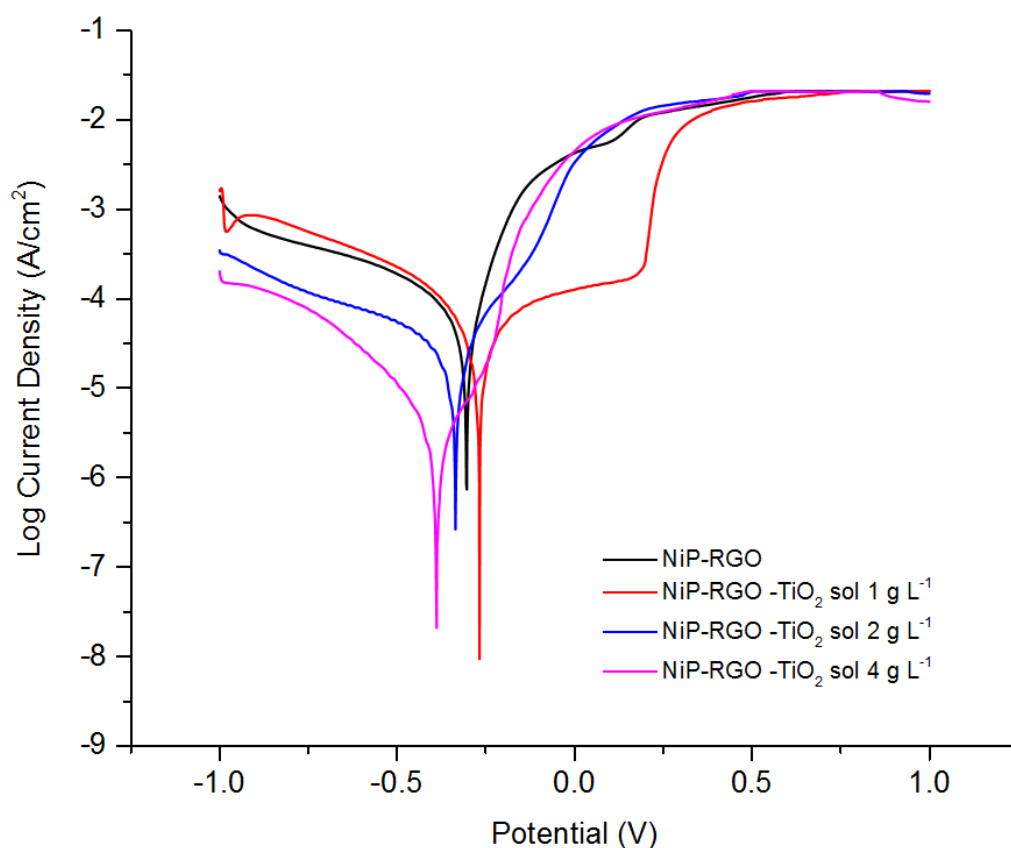


**Figure 4.6** Potentiodynamic polarization curves of NiP-TiO<sub>2</sub> sol-RGO coated steel surfaces with the different amount of TiO<sub>2</sub> sol loaded in 3.5 wt% NaCl aqueous solution.

**Table 4.1** Corrosion characteristic of different surfaces obtained from potentiodynamic polarization curves of Figure 4.6.

Surface	$E_{\text{corr}}$ vs Ag/AgCl (V)	$i_{\text{corr}}$ ( $\mu\text{A cm}^{-2}$ )
NiP-RGO	-0.30	63.1
NiP-RGO -TiO <sub>2</sub> sol 1 g L <sup>-1</sup>	-0.26	16.5
NiP-RGO -TiO <sub>2</sub> sol 2 g L <sup>-1</sup>	-0.34	12.5
NiP-RGO -TiO <sub>2</sub> sol 4 g L <sup>-1</sup>	-0.4	26.3



#### 4.2.2 Effect of electroless deposition time

The electroless deposition time was investigated and optimized with GO 0.5 g L<sup>-1</sup> and TiO<sub>2</sub> sol 1.0 g L<sup>-1</sup>. The deposition time was varied from 15 to 45 minutes (Figure 4.7). NiP-TiO<sub>2</sub> sol-RGO with plating duration for 15 minutes shows uniformity of RGO films with the intercalation of Ni nanoparticles onto RGO layer. When the deposition time was increased to 30 minutes, RGO films on the coated surface was increased and Ni was not observed in RGO layers. For 45 minutes of coating process, the NiP-TiO<sub>2</sub> sol-RGO surface shows the large clusters of Ni without RGO films covering the surfaces.

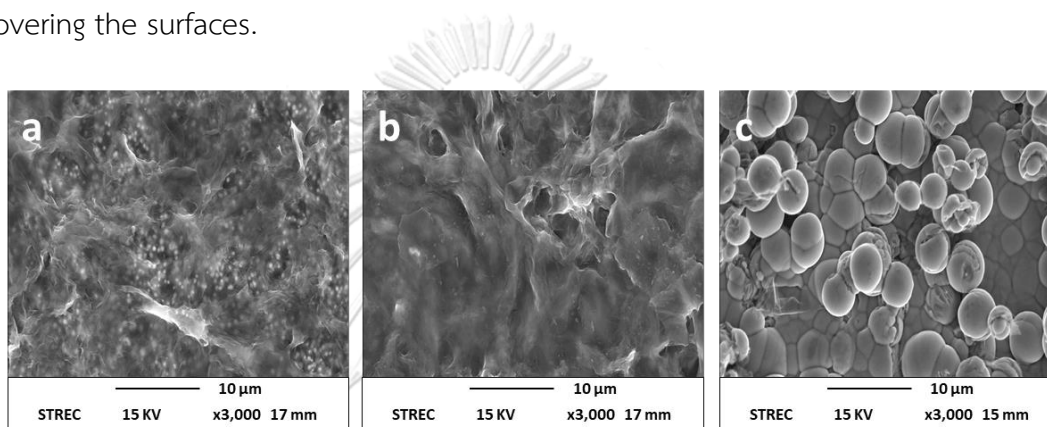


**Figure 4.7** SEM images of NiP-TiO<sub>2</sub> sol-RGO coated steel surfaces with different plating times: 15 min (a), 30 min (b) and 45 min (c).

For the corrosion resistant testing by electrochemical measurements, the results show that 15 minutes of deposition time exhibits the highest corrosion resistance (Figure 4.8). The  $E_{corr}$  and  $I_{corr}$  values from polarization curves are presented in Table 4.2. This suggested that the restacking of RGO at a too long time possibly interfere the NiP deposition process leading to a loose structure of NiP with larger nodules, resulting in the low corrosion resistance of coated surfaces. Thus, 15 minutes of plating was chosen for the next experiments.

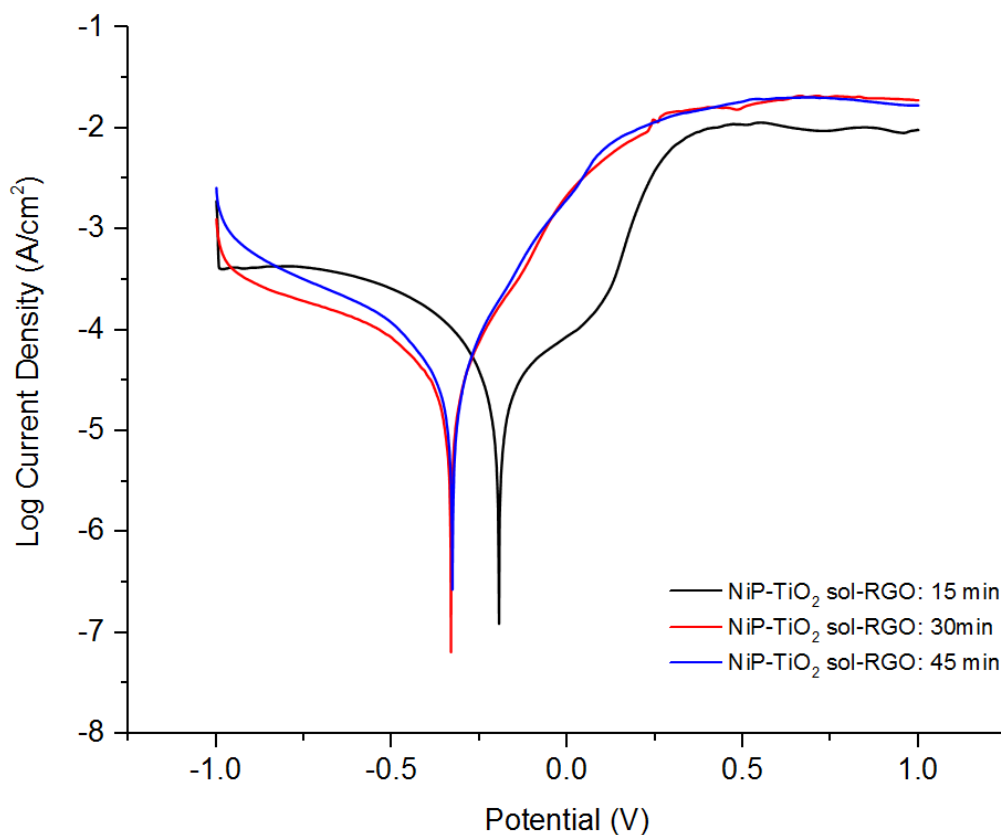


**Figure 4.8** Potentiodynamic polarization curves of NiP-TiO<sub>2</sub> sol-RGO composite coating with different plating time in 3.5 wt% NaCl aqueous solution.

**Table 4.2** Corrosion characteristics of different surfaces obtained from potentiodynamic polarization curves of Figure 4.8.

Surface	$E_{\text{corr}}$ vs Ag/AgCl (V)	$i_{\text{corr}}$ ( $\mu\text{A cm}^{-2}$ )
NiP-TiO <sub>2</sub> sol RGO: 15 min	-0.20	31.6
NiP-TiO <sub>2</sub> sol RGO: 30 min	-0.34	63.0
NiP-TiO <sub>2</sub> sol RGO: 45 min	-0.34	66.0

### 4.2.3 Effect of GO loading

The NiP-TiO<sub>2</sub> sol-RGO composite with different amount of GO loading in a range of 0-1.0 g L<sup>-1</sup> was investigated and optimized as demonstrated in Figure 4.9a-c. The results show that RGO films increased when the amount of GO increases and fully covered with a uniformity on the surfaces at the concentration of GO 0.5 g L<sup>-1</sup> (Figure 4.9b.). Moreover, we observed that the Ni particle size was decreased into nanoscale when the GO concentration increased from 0.1 to 0.5 g L<sup>-1</sup> due to the increasing of number of GO sheet nucleation sites and this phenomenon has been reported in the previous study [92]. As shown in Figure 4.9c, NiP-TiO<sub>2</sub> sol-RGO composite using 1.0 g L<sup>-1</sup> GO loading reveals the thick RGO films with random pores on the coated surface. Moreover, RGO sheets might slipped at too high GO concentration, leading to the less coating reproducibility.

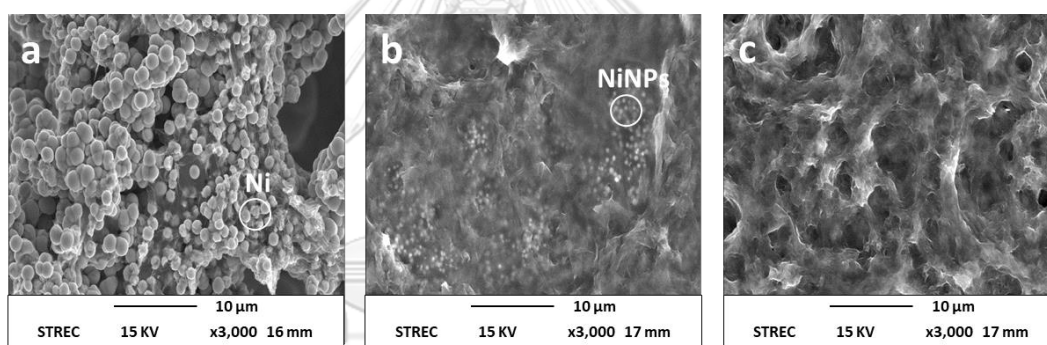


**Figure 4.9** SEM images of NiP-TiO<sub>2</sub> sol-RGO composite coating with different amount of GO loaded including GO 0 g L<sup>-1</sup> (a), GO 0.5 g L<sup>-1</sup> (b), GO 1.0 g L<sup>-1</sup> (c).

As for the corrosion behavior, the best corrosion protection of coated surface was demonstrated the highest and lowest value of corrosion potential ( $E_{\text{corr}}$ ) and corrosion current density ( $I_{\text{corr}}$ ), respectively. The results show that  $E_{\text{corr}}$  value of NiP-TiO<sub>2</sub> sol-RGO composite shifts to positive potential (Figure 4.10) and the  $I_{\text{corr}}$  value of NiP-TiO<sub>2</sub> sol-RGO composites decreases when amount of GO increases from 0-0.5 g L<sup>-1</sup> (Table 4.3). From the results confirmed that the incorporation of RGO on surfaces can improve the corrosion resistance of coated surfaces. This suggested that, the RGO incorporated NiP-TiO<sub>2</sub> sol matrices act as a barrier to protect the penetration of O<sub>2</sub>, H<sub>2</sub>O and harmful ions (i.e. H<sup>+</sup>, OH<sup>-</sup>, Cl<sup>-</sup>) [93-95]. However, the  $I_{\text{corr}}$  value of NiP-TiO<sub>2</sub>

sol-RGO composite increases and the  $E_{\text{corr}}$  value of NiP-TiO<sub>2</sub> sol-RGO composite slightly shifts to negative potential when the amount of GO more than 0.5 g L<sup>-1</sup>. This is probably caused by the pores of RGO films on the coated surface, leading to crack initiation and delamination of the deposited surface. Thus, NiP-TiO<sub>2</sub> sol plating bath with 0.5 g L<sup>-1</sup> of GO was selected for the further studies.

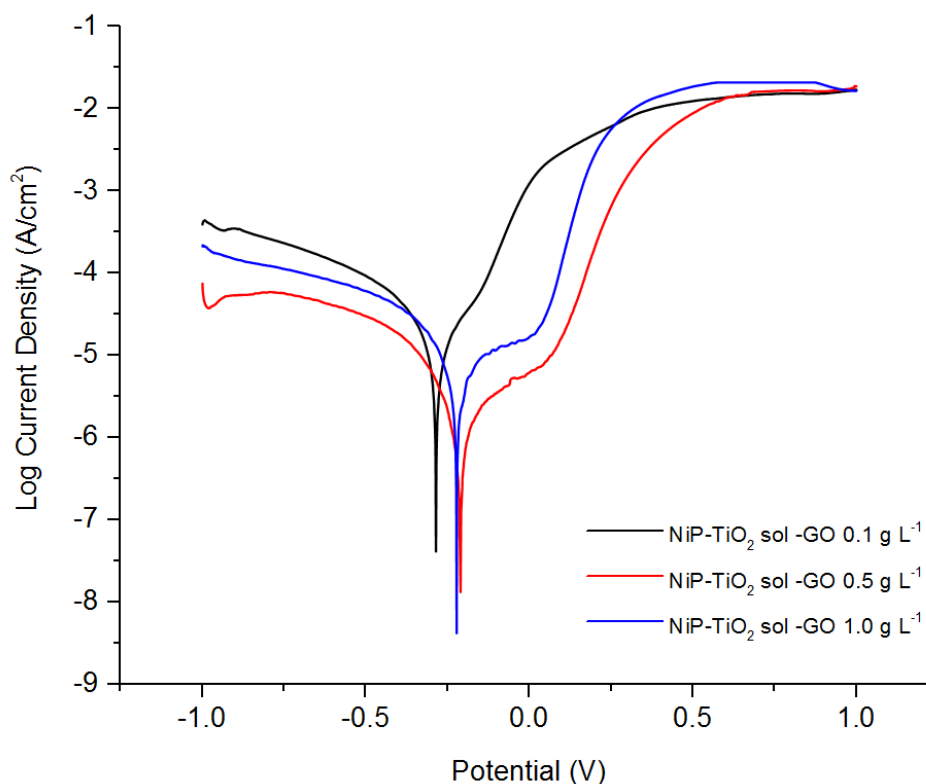


**Figure 4.10** Potentiodynamic polarization curves of NiP-TiO<sub>2</sub> sol-RGO composite coating with different amount GO of loaded in 3.5 wt% NaCl aqueous solution.

**Table 4.3** Corrosion characteristic of different surfaces obtained from potentiodynamic polarization curves of Figure 4.10.

Surface	$E_{\text{corr}}$ vs Ag/AgCl (V)	$i_{\text{corr}}$ ( $\mu\text{A cm}^{-2}$ )
NiP-TiO <sub>2</sub> sol 1 g/L-GO 0.10 g L <sup>-1</sup>	-0.28	5.0
NiP-TiO <sub>2</sub> sol 1 g/L-GO 0.50 g L <sup>-1</sup>	-0.21	1.9
NiP-TiO <sub>2</sub> sol 1 g/L-GO 1.00 g L <sup>-1</sup>	-0.22	3.01

### 4.3 Characterization of NiP-TiO<sub>2</sub> sol-RGO nanocomposite coated surface

#### 4.3.1 Surface morphology characterization

After the all parameters of NiP-TiO<sub>2</sub> sol-RGO coated surfaces were optimized. The optimal conditions including 1.0 g L<sup>-1</sup> TiO<sub>2</sub> sol, 0.5 g L<sup>-1</sup> GO and 15 minutes of plating were used for electroless plating process. The morphology of NiP-TiO<sub>2</sub> sol-RGO nanocomposite coated surface was characterized by SEM. Figure 4.11 shows SEM images of NiP, NiP-TiO<sub>2</sub> sol and NiP-TiO<sub>2</sub> sol-RGO coated surfaces, respectively. The surface morphology of NiP exhibits a nodular structure with the small grain inside as shown in Figure 4.11a. From Figure 4.11b, the NiP-TiO<sub>2</sub> sol surface morphology shows the smaller nodular and more homogeneous than NiP coated surface. The SEM image of NiP-TiO<sub>2</sub> sol-RGO as Figure 4.11c reveals a uniformity and homogeneity of the coated surface. This is probably caused by the intercalation of TiO<sub>2</sub> sol in GO layers acted like a stabilizing agent in the solution. Moreover, the Ni nanoparticles are well-dispersed and uniformly on RGO films and a typical wrinkle of RGO sheets on the coated surfaces can be clearly observed. From NiP-TiO<sub>2</sub> sol-RGO surface morphology, the Ni nanoparticles could link RGO sheet via Ni-C  $\sigma$  bond, leading to multiple-layer structure (sandwich structure) formation [96]. In addition, Figure 4.11d showed a cross-sectional morphology of NiP-TiO<sub>2</sub> sol-RGO coating, which showed the two step electroless deposition mechanism. Initially, NiP-TiO<sub>2</sub> sol was deposited with high adhesion onto the steel surface as a bottom layer ( $\sim 2.8 \mu\text{m}$ ), then NiP-TiO<sub>2</sub> sol-RGO layer ( $\sim 21.3 \mu\text{m}$ ) was deposited on top of NiP-TiO<sub>2</sub> sol. In this layer, NiP-TiO<sub>2</sub> sol was intercalated with RGO layers acting as an adhesive for RGO coating. Moreover, the existing of RGO on the coated surface is characterized by Raman spectrum. Figure 4.11e showed two characteristic peaks (G: 1580 cm<sup>-1</sup> and D: 1350 cm<sup>-1</sup>) The higher intensity ratio of D and G band ( $I_D/I_G$ ) indicate the increased defects in GO structure caused by the elimination of oxygen functional group during the reduction process [97, 98].

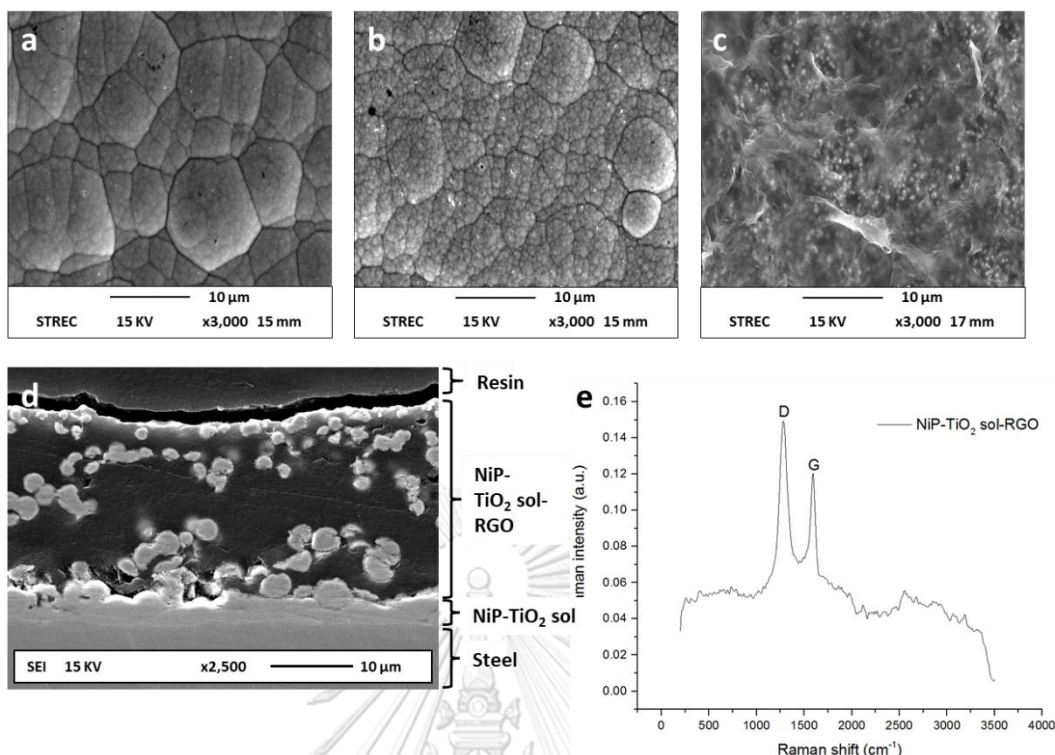


**Figure 4.11** SEM images of NiP (a), NiP-TiO<sub>2</sub> sol (b) and NiP-TiO<sub>2</sub> sol-RGO (c) composite coated steel surfaces and a SEM image of cross-section (d) and Raman spectrum of NiP-TiO<sub>2</sub> sol-RGO coating (e).

### 4.3.2 Surface wettability characterization

Water contact angle (WCA) measurement is a well-known technique for surface characterization. Normally, the coated surfaces wettability considered by the contact angle between water and surface. When water and surface interact with small contact angle ( $< 90^\circ$ ), the surface is high wettability (hydrophilic). While large contact angle ( $> 90^\circ$ ), indicating that the surface is low wettability (hydrophobic). In this work, the wettability of NiP-TiO<sub>2</sub>-RGO coated surface was evaluated and compared with NiP and NiP-TiO<sub>2</sub> sol coated surface. The water drop images and contact angle results are illustrated in Figure 4.12. The NiP and NiP-TiO<sub>2</sub> sol coated surfaces show a hydrophilic surface with a WCA value of  $61.1 \pm 1.36^\circ$  and  $66.82 \pm 2.18^\circ$ , respectively. However, the NiP-TiO<sub>2</sub> sol-RGO coating is a hydrophobic surface with a WCA value of  $114.12 \pm 1.52^\circ$  due to the incorporation and the fully covered of RGO on the coated surfaces. Since the water-repelling properties of NiP-TiO<sub>2</sub> sol-RGO

hydrophobic surfaces lead to the protection of this coated surface from the water wettability and thus corrosion.

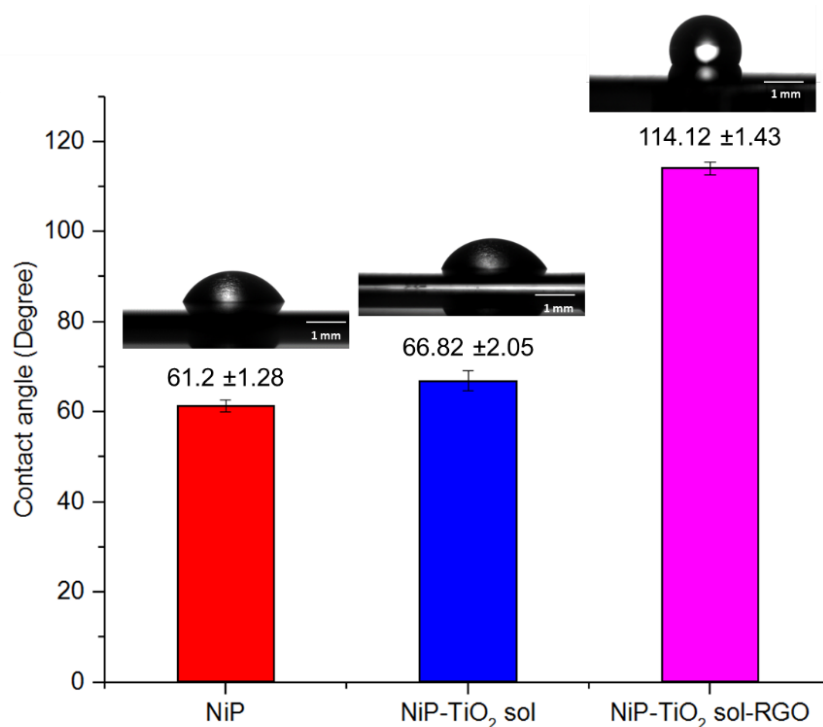


**Figure 4.12** The water drop images and contact angle results of the NiP, NiP-TiO<sub>2</sub> sol and NiP-TiO<sub>2</sub> sol-RGO coated surfaces, respectively. The error bars correspond to the standard deviation obtained from five measurements (n = 5).

### 4.3.3 Corrosion resistance characterization

To evaluate the corrosion resistance performance of NiP-TiO<sub>2</sub> sol-RGO coated surfaces, the electrochemical measurement was used. The potentiodynamic polarization curves of NiP-TiO<sub>2</sub> sol-RGO composite coating compared with steel, NiP and NiP-TiO<sub>2</sub> sol are shown in Figure 4.13. The  $E_{\text{corr}}$  and  $I_{\text{corr}}$  values from polarization curves are presented in Table 4.4. The results show that the  $I_{\text{corr}}$  of NiP-TiO<sub>2</sub> sol-RGO (5.0  $\mu\text{A}/\text{cm}^2$ ) coated surface is significantly lower than steel surface (39.8  $\mu\text{A}/\text{cm}^2$ ). However, the all coated surfaces; NiP, NiP-TiO<sub>2</sub> sol, and NiP-TiO<sub>2</sub> sol-RGO provide a comparable  $I_{\text{corr}}$ , indicating that the coated surfaces have a similar corrosion rate. As for the corrosion potential,  $E_{\text{corr}}$  value of NiP-TiO<sub>2</sub> sol-RGO coated surface shifts to a positive potential and exhibits the highest positive  $E_{\text{corr}}$  compared to the NiP, NiP-TiO<sub>2</sub>

sol and steel surfaces. This suggested that the coverage of RGO films on surface act as a passive layer to decrease oxygen permeability and protect electron and ion transport between the surface and the electrolyte [99-101].

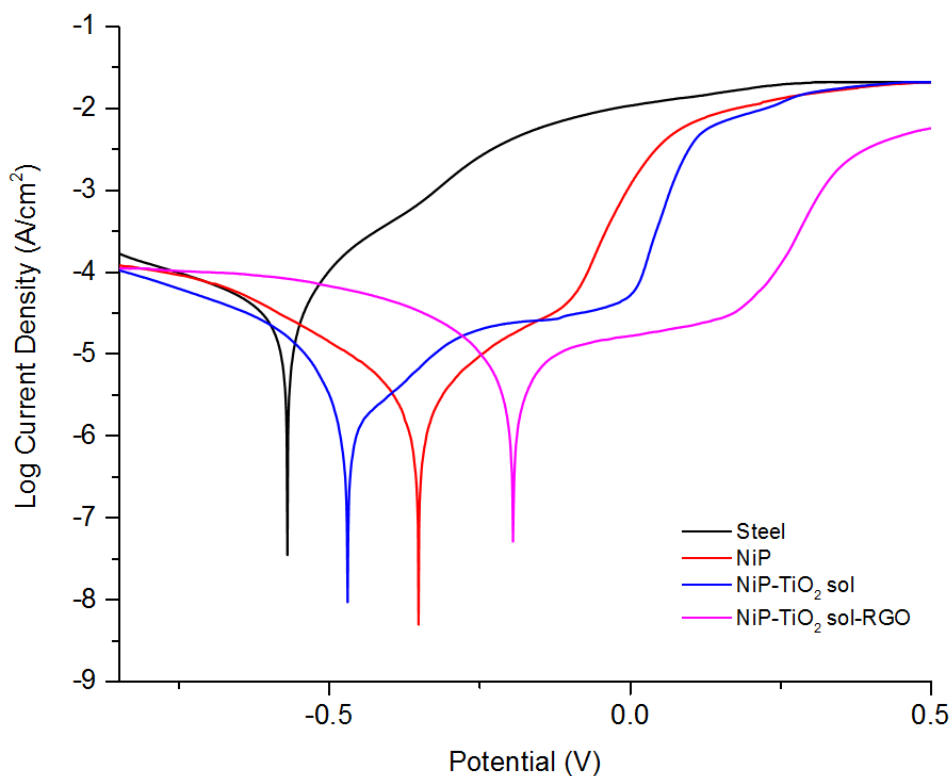


**Figure 4.13** Potentiodynamic polarization curves of NiP (a), NiP-TiO<sub>2</sub> sol (b), and NiP-TiO<sub>2</sub> sol-RGO coated surfaces in 3.5 wt% NaCl aqueous solution.

**Table 4.4** Corrosion characteristic of coated surfaces obtained from potentiodynamic polarization curves of Figure 4.13.

Surface	$E_{\text{corr}}$ vs Ag/AgCl (V)	$i_{\text{corr}}$ ( $\mu\text{A cm}^{-2}$ )
Steel	-0.54	39.8
NiP	-0.35	5.4
NiP-TiO <sub>2</sub> sol	-0.48	5.6
NiP-TiO <sub>2</sub> sol-RGO	-0.19	5.0



#### 4.3.4 Electrical conductivity characterization

For the electrical conductivity measurement, the coated surfaces were characterized by using a four point probe equipment. The relative electrical conductivity  $C_c/C_s$  was shown to indicate the electrical conductivity enhancement, where  $C_c$  represents the measured electrical conductivity of the coated surface and  $C_s$  represents the measured electrical conductivity of steel [1]. Since the electrical resistivity of NiP increases when phosphorus content increases [102], the relative conductivity of NiP is slightly lower than the steel surface (Figure 4.14). The conductivity of NiP-TiO<sub>2</sub> sol coated surface was significantly reduced compared to NiP. Because the semi-conductor property of TiO<sub>2</sub> sol may hinder the electron mobility on the surface, leading to low conductivity of NiP-TiO<sub>2</sub> sol coated surfaces. On the other hand, the relative conductivity of NiP-TiO<sub>2</sub> sol-RGO coated surface shows the highest electrical conductivity compared to NiP and NiP-TiO<sub>2</sub> sol coated surfaces. This suggests that the incorporation of RGO onto the coated surface leads to an improvement in the surface conductivity.

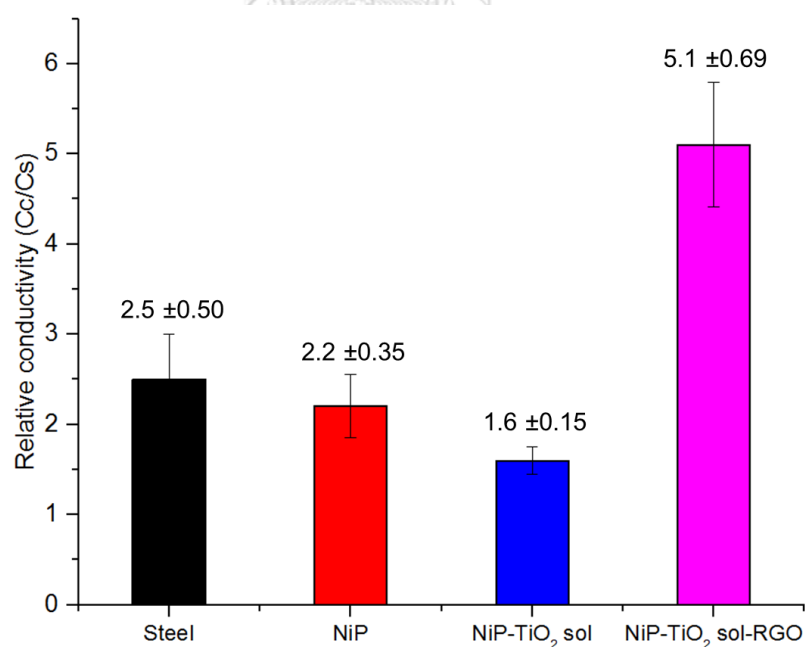


**Figure 4.14** Relative conductivity of the NiP, NiP-TiO<sub>2</sub> sol and NiP-TiO<sub>2</sub> sol-RGO coated surfaces, respectively. The error bars correspond to the standard deviation obtained from five measurements ( $n = 5$ ).

#### 4.3.5 Electrochemical sensor application

This NiP-TiO<sub>2</sub> sol-RGO coated steel surfaces was applied for non-enzymatic glucose detection by using cyclic voltammetry. Three difference electrodes are unmodified, NiP-TiO<sub>2</sub> sol and NiP-TiO<sub>2</sub> sol-RGO electrodes are shown in Figure 4.15. The current response of NiP-TiO<sub>2</sub> sol-RGO electrode was higher than on an unmodified and NiP-TiO<sub>2</sub> sol electrodes. This suggest that the NiP-TiO<sub>2</sub> sol-RGO composite act as enzyme mimicking catalyst and facilitated electron transfer process in the system.

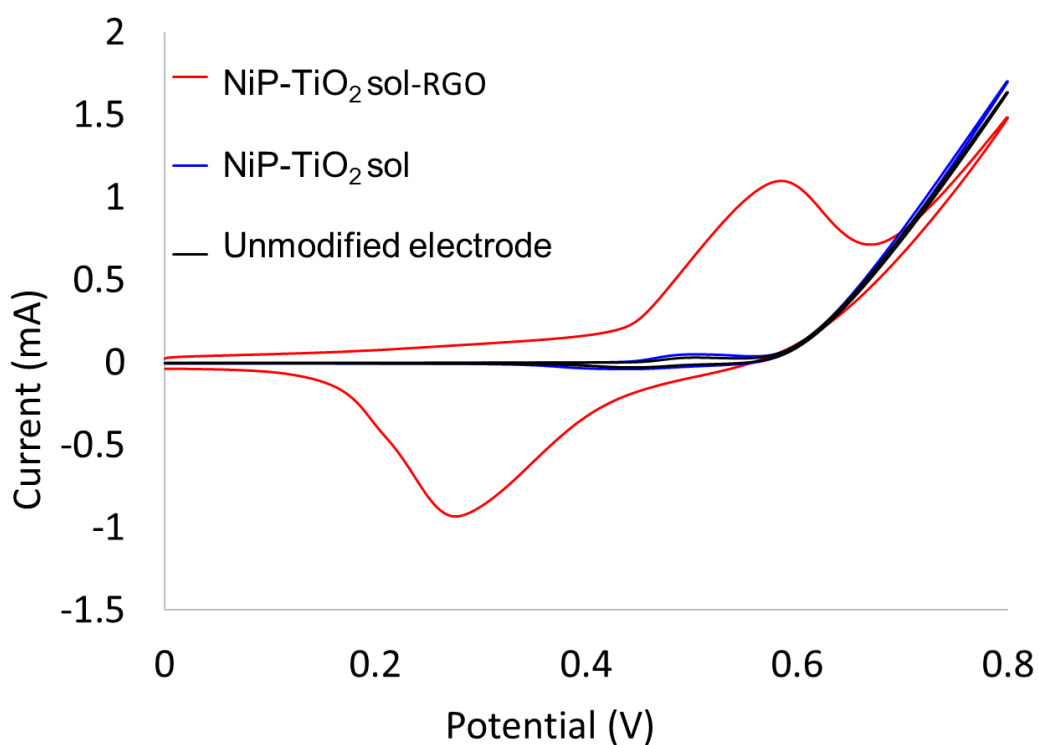


**Figure 4.15** Cyclic voltammograms of 1.5 mM glucose in 0.1 M NaOH using the unmodified, NiP-TiO<sub>2</sub> sol and NiP-TiO<sub>2</sub> sol-RGO electrodes.

## Part II: GO nanocomposite coated textile substrate

### 4.4 Cotton fabric based colorimetric sensor for simultaneous sweat pH and lactate

#### 4.4.1 Physical characterization of different layers of modified cotton

The photographs showing the appearance of different layers of the modified cotton based sensors are shown in Figure 4.16, which include the unmodified cotton substrate (Figure 4.16a), chitosan/cotton substrate (Figure 4.16b), NaCMC-CTAB-indicator dyes /chitosan /cotton substrate (Figure 4.16c), NaCMC hydrogel/CMC-CTAB-indicator/chitosan/cotton substrate (Figure 4.16d) and NaCMC hydrogel/CMC-CTAB-indicator/ chitosan/cotton substrate with the hydrophobic barrier (Figure 4.16e). The cotton substrate shows the bright white color (Figure 4.16a) and when the chitosan is coated on the cotton, it became yellowish (Figure 4.16b). The chitosan film was coated as a first layer to serve as a the dye fixator due to the interaction between positively charged amino groups of chitosan and negatively charged groups of the indicator dyes [52, 103, 104]. The presence of CTAB as the cationic surfactant in the second layer showed the blue-green color (Figure 4.16c) and served the adsorption and indicator dye fixation on the textile substrate. NaCMC hydrogel was added to create a hydrogel network on the top of the sensor and it can be seen in yellow-green color (Figure 4.16d). The hydrogel layer was used for enzyme entrapment and to provide long-term stability of the lactate oxidase and increased the amount of enzyme loading [105]. This hydrogel also used for the sweat absorption onto this sensor, and preconcentrated the analyte. The Figure 4.16e showed the hydrophobic barrier boundary between pH (yellow-green area) and lactate (white area) detection zone on the textile based colorimetric sensor.

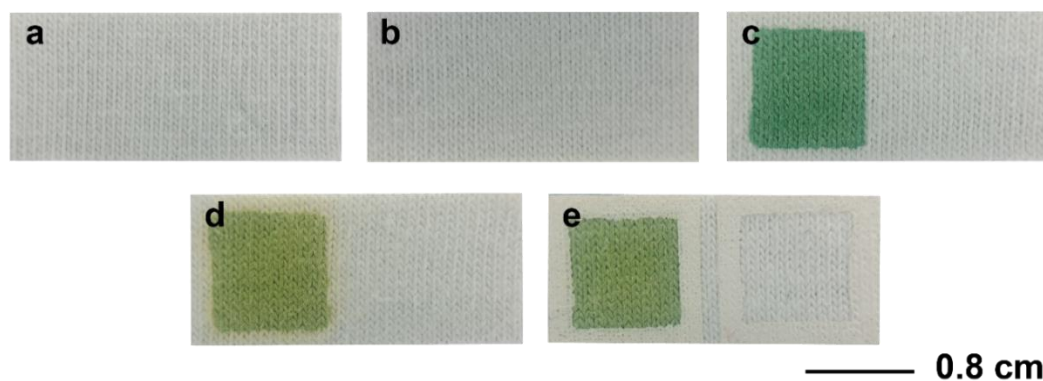


**Figure 4.16** Photographs of unmodified cotton substrate (a), chitosan/cotton substrate (b), NaCMC-CTAB-indicator dyes/chitosan/cotton substrate (c), NaCMC hydrogel/CMC-CTAB-indicator/chitosan/ cotton substrate (d) and NaCMC hydrogel/CMC-CTAB-indicator/ chitosan/cotton substrate with the hydrophobic barrier (e).

The morphologies of cotton were characterized by FE-SEM. The surface morphology of cotton substrate showed a smooth fiber surface with an average diameter of  $12.7 \pm 2.5 \mu\text{m}$  as shown in Figure 4.17a. For chitosan coated cotton substrate, Figure 4.17b shows the rougher surface and uniform thin film layer of chitosan on the substrate without aggregation on the fibers whereas the coated of NaCMC-CTAB-indicator dyes on the chitosan/cotton substrate observed the NaCMC-CTAB-indicator dyes film with random aggregation on the cotton substrate as shown in Figure 4.17c, which is possibly caused by the negatively charged indicator dyes selectively bind to the oppositely charged group on the surface of the cotton fibers. The FE-SEM image of NaCMC hydrogel coated substrate (Figure 4.17d) reveals the thicker hydrogel films with the cracked surface on the coated substrate.

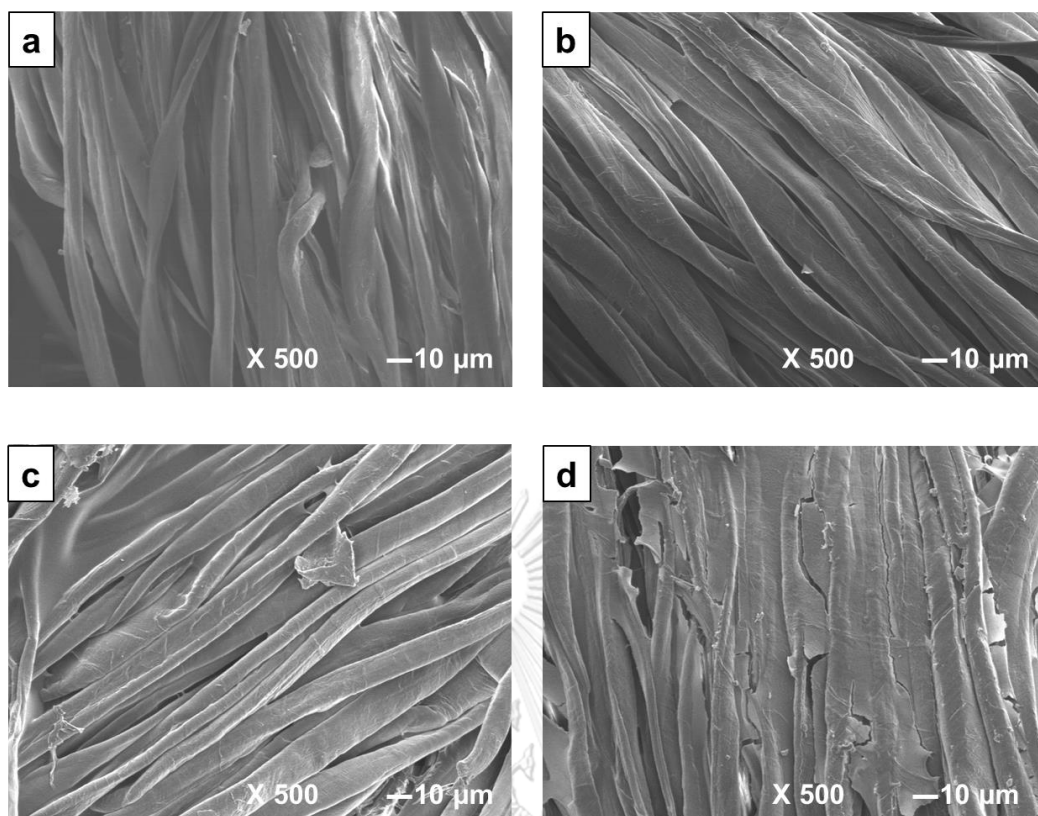


**Figure 4.17** FE-SEM images of cotton (a), chitosan/cotton (b), NaCMC-CTAB-indicator dyes/ chitosan (c) and NaCMC hydrogel/ NaCMC-CTAB indicator dyes/ chitosan/cotton (d).

#### 4.4.2 Chemical characterization of the layers

FT-IR spectroscopy was used to chemically characterize the different layers of modified cottons in a range of  $400 - 4000 \text{ cm}^{-1}$  as shown in Figure 4.18. The FT-IR spectrum of an unmodified cotton substrate shows the characteristic peaks of cellulose, which is the main component of cotton at  $3297$ ,  $2899$  and  $1640 \text{ cm}^{-1}$  corresponding to O-H bond, C-H bond and  $\text{CH}_2$  group [106]. The FT-IR spectrum of chitosan coated cotton shows peaks at  $3334 \text{ cm}^{-1}$  related to N-H bond [104]. For the NaCMC-CTAB-indicator/ chitosan and NaCMC hydrogel/ NaCMC-CTAB-indicator/ chitosan coated textiles, the spectra were very similar to the chitosan coated cotton substrate. FT-IR spectra of all modified layers showed a similar peak to the cotton due to low quantity of each component presenting on the sensor surface.

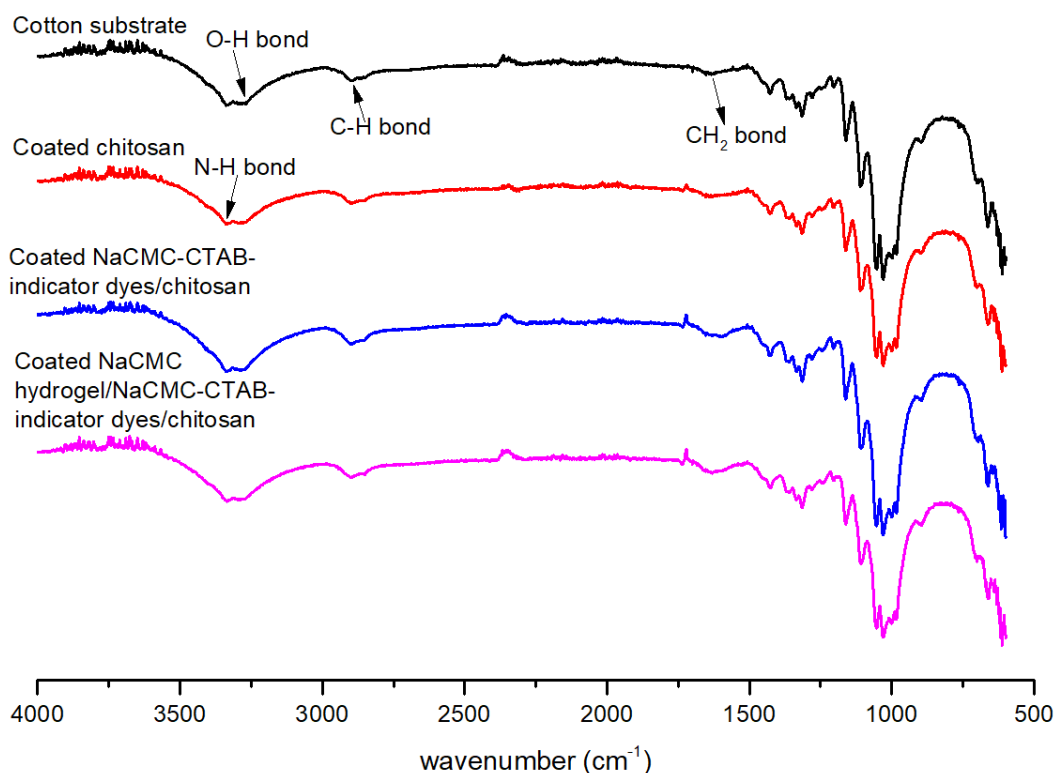
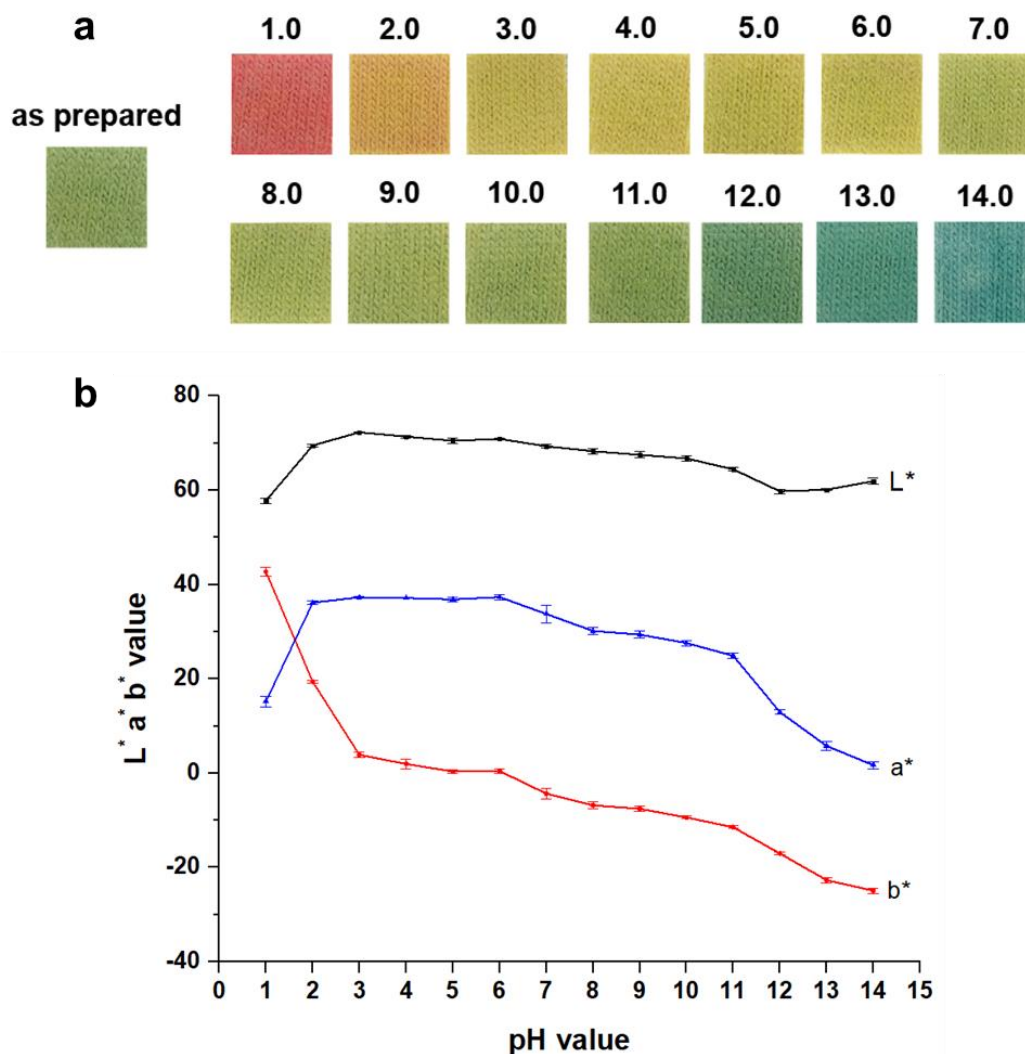


Figure 4.18 FT-IR spectrum of the difference coated cotton layers.

## 4.5 Sensor performance testing

### 4.5.1 Standard color chart of textile based pH sensor

As for the sweat pH detection, a mixed indicator dye containing methyl orange and bromocresol green was used to modify the detection zone which change in color over a pH range defined by their  $pK_a$  values [66]. The response of color change of this cotton based sensor depends on the pH of the analyte solution shown in Figure 4.19a. The color change of pH based colorimetric sensor developed in this study can be clearly divided into 7 domains including pH 1, pH 2, pH 3-6, pH 7, pH 8-10, pH 11-13 and pH 14 depending on the change of the slope of Figure 4.19b. This textile based colorimetric sensor can distinguish the pH color change cover the typical pH range (4.0 – 7.0) of normal status of human sweat [69, 74, 75, 107]. In term of application of this sweat pH sensor on human skin, the higher pH indicates the higher sweat rate and metabolism rate, which is the crucial information for evaluate the physiological conditions related to the performances of individual and more important for the athletes.



**Figure 4.19** Standard color charts for textile based pH sensor (a) and  $L^* a^* b^*$  color model of pH in 0.1 M PBS solution (b). \* The value of  $L^*$  represents brightness (+ = lighter, - = darker) while the  $a^*$  and  $b^*$  represent the distant along the red-green (+ = redder, - = greener) and blue-yellow (+ = yellower, - = bluer) axis, respectively [108]. The error bars correspond to standard deviation obtained from five measurements (n=5).

#### 4.5.2 Standard colorimetric chart of textile based lactate sensor

The intensity of color sensor visibly increases as a direct function of lactate concentration as shown in Figure 4.20. It should be noted that the lactate concentration in human sweat depends on the metabolism of the person and it varies to a maximal level at around 10 - 12 mM [45]. Thus, this sensor can potentially

be used to differentiate between the normal (< 12.5 mM) and the high ( $\geq$  12.5 mM) lactate level in the human sweat, which is an important threshold value to indicate the cramp and muscle fatigue during the exercise.

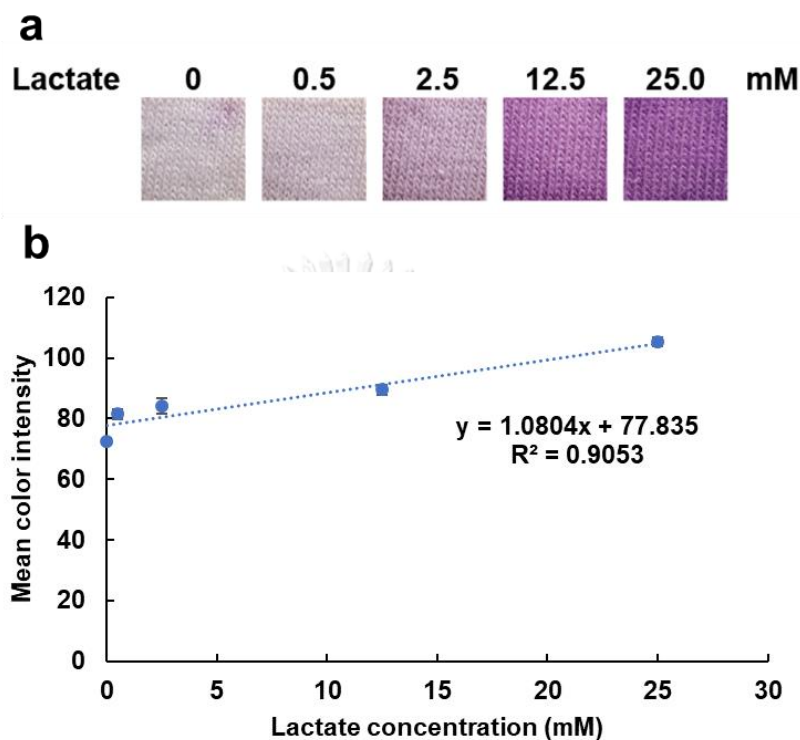


**Figure 4.20** Standard color charts of textile based lactate sensor in the concentration range of 0, 0.5, 2.5, 12.5 and 25 mM (a) and the plot of lactate concentration versus the mean grey color intensity (b). The error bars correspond to standard deviation obtained from five measurements ( $n=5$ ).

#### 4.5.3 On-body trial results from volunteers

This textile based colorimetric sensor was applied for the simultaneous detection of sweat pH and lactate in human during exercise. This sensor was directly patched on the abdomen skin of the volunteers ( $n \geq 3$ ) before they went running. After 30 minutes, this textile sensor was collected, and the colors were compared with the standard color chart. The color of both detection areas including sweat pH and lactate obviously changed after the exercise (Figure 4.21). The color of sweat pH detection area of all volunteers was changed into green. The result indicating a



sweat pH value of all volunteers are approximately 8-10 compared with the standard pH chart (Figure 4.19a), it possibly caused by the higher sweat rate and metabolism rate. For lactate detection the intensity of color increased depending on the personal metabolism indicating the fitness of each individual person. The volunteer 1 has a normal lactate level approximately 13 mM. While, the volunteer 2 and 3 has the highest lactate concentration approximately 60 and 64 mM, respectively (Figure 4.21) compared with the standard chart of lactate (Figure 4.20a-b). These results suggest that after running for 30 minutes, the body status (*i.e. metabolism, dehydration and sweat rate*) of the volunteer 2 and 3 might has muscle fatigue due to the excess of lactate in the muscle. This textile based colorimetric sensor provide a real-time monitoring of sweat pH and lactate and it can be directly patched on the skin without irritation. Along with the unique properties of textile sensor, which is durable, breathable, comfortable and flexible, it might be a novel platform for evaluating the body performances of human during exercise, especially for the athletes.

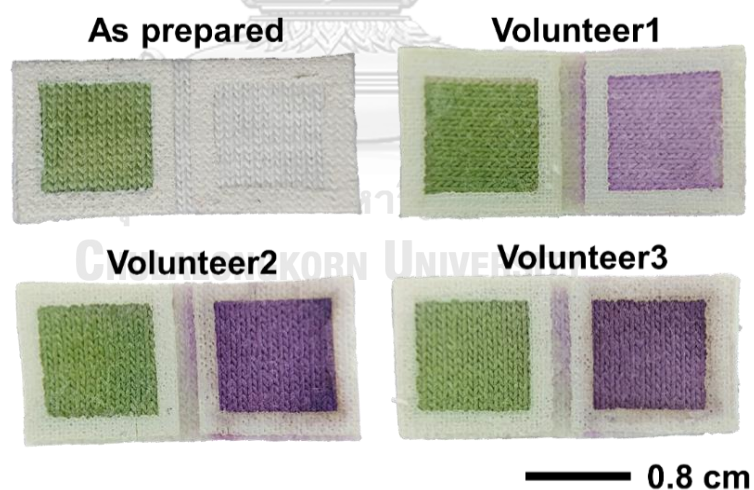


**Figure 4.21** The textile based colorimetric of four volunteers after exercise for 30 minutes.

#### 4.5.4 Testing the color fade of textile based sensor

This textile based sensor was fabricated for sweat pH and lactate detection in the sport applications. The color fade indicating the durability of sensor is the most important factor. For example, if the athlete has a high sweat rate, it will wash out the sensing element of this textile sensor during the exercise leading to the color fade and error in color readout signal. In this study, CTAB was added into the mixed indicator dyes as a sensing element of sweat pH. The results showed that the pH sensing element of the sensor without CTAB was washed out after 30 minutes whereas the pH sensing of the sensor with CTAB still exists onto the textile based colorimetric sensor after 60 minutes (Figure 4.22). This verifying that the adding of CTAB into the indicator dyes increased the dye adsorption on the textile substrate due to the interaction between cation of surfactant and anion of indicator dyes leading to the incorporation of indicator dye molecules into the micellar structures [109].

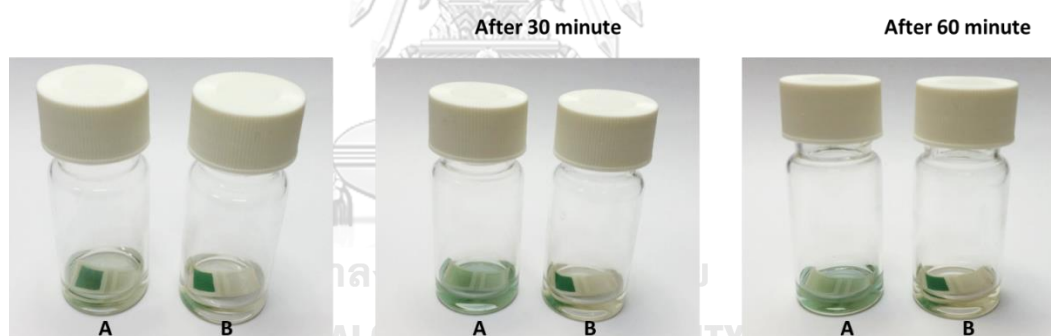


**Figure 4.22** Photographs of the textile based sensor with (B)/ without CTAB (A) that soaking in PBS (pH 7.4) solution for 0, 30, and 60 minutes.

#### 4.6 Thread based colorimetric sensor for simultaneous sweat glucose and urea

In this work, we optimized this sensor system based on glucose detection because the cut-off level of glucose in sweat is lower than urea. Therefore, the key parameters including chitosan concentration, GO concentration, coating structure were optimized on glucose.

#### 4.6.1 Optimization of thread based colorimetric sensor

##### 4.6.1.1 Effect of chitosan concentration

Chitosan was chosen as an immobilized enzyme supporter in order to improve the color intensity for enzyme-based sensor. Figure 4.23 showed the photographs of thread based sensor at the glucose detection area with difference concentration of chitosan. The color intensity of glucose was increased when the chitosan concentration increases from 0 to 1 % w/v and the color intensity decrease afterwards. This is probably caused by the uniformity of chitosan film on the cotton thread surface. Thus, 1% w/v chitosan was chosen for all further experiments.

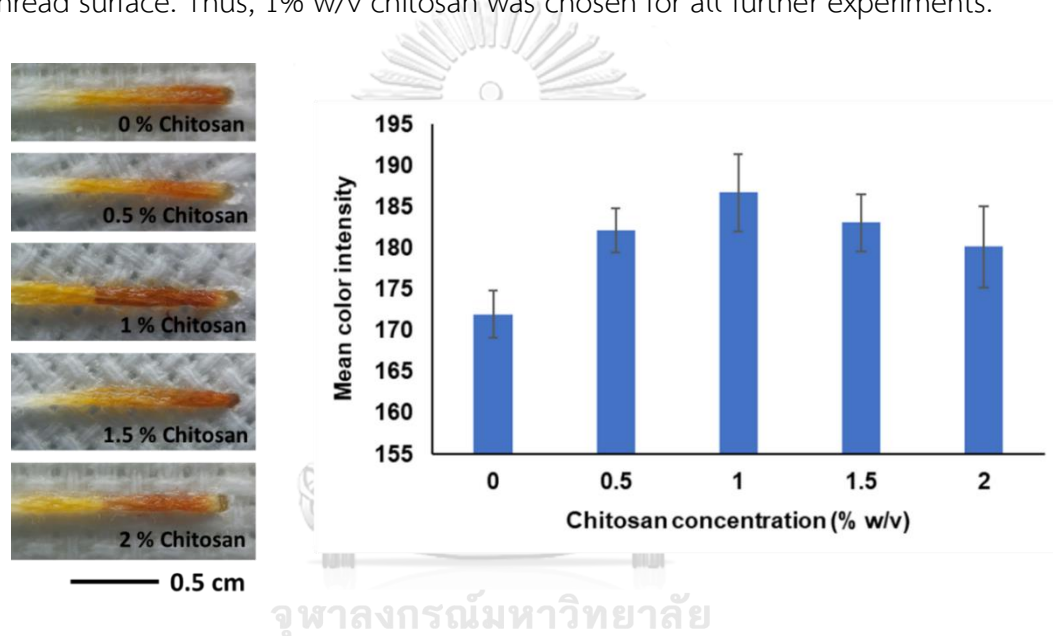


**Figure 4.23** Thread-based sensor with different chitosan concentration (0 – 2 % w/v) at the glucose detection zone of 3 mM glucose. The error bars correspond to standard deviation obtained from five measurements (n=5).

##### 4.6.1.2 Effect of glucose oxidase volume

The volume of glucose assay was optimized. The thread based colorimetric sensor was prepared by using the different volume of glucose assays in a range of 4 to 16  $\mu\text{L}$ . This modified thread based sensor was tested with 3 mM of glucose. The result showed that the color intensity of this sensor increases when the volume of chitosan increases from 4 to 12  $\mu\text{L}$  (Figure 4.24). However, the color intensity of the

assay volume between 8  $\mu\text{L}$  and 12  $\mu\text{L}$  are not significantly different. To reduce cost of this sensor system, 8  $\mu\text{L}$  of glucose assay was chosen for the further studies.

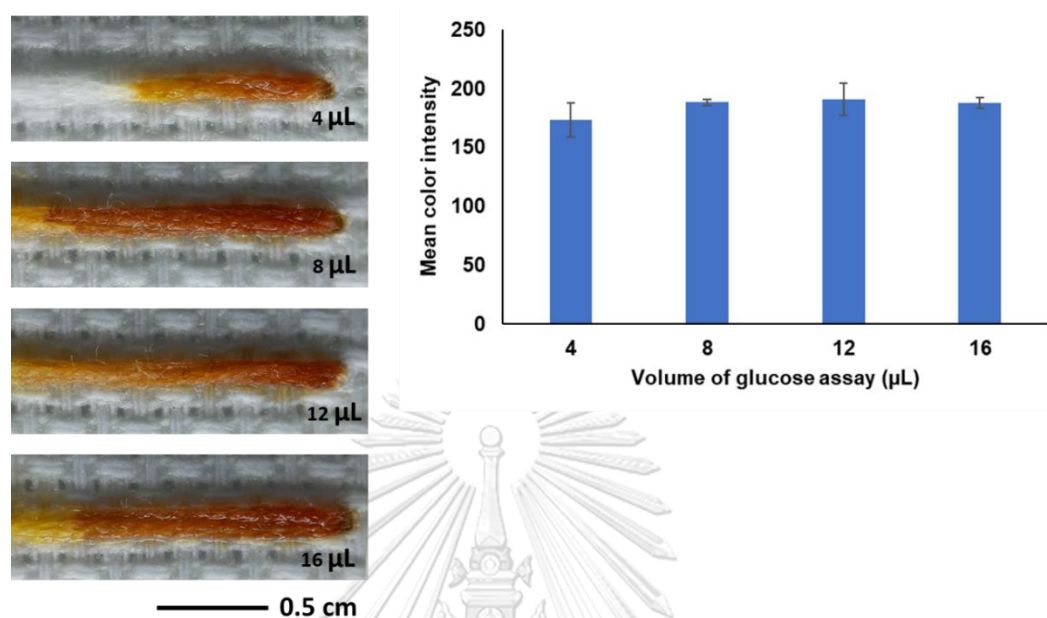


**Figure 4.24** Thread-based colorimetric sensor with different volume of glucose assay (4 – 16  $\mu\text{L}$ ) at the glucose detection zone of 3 mM glucose. The error bars correspond to standard deviation obtained from five measurements ( $n=5$ ).

#### 4.6.1.3 Effect of the hydrogel structure

To improve the sensitivity of this sensor, GO was incorporated with the chitosan. The result showed that CS-GO modified thread can enhance the color intensity of this sensor (Figure 4.25). This is probably cause by the incorporated of GO on the thread leading to increased surface area of enzyme immobilization of this thread based colorimetric sensor. In addition, the chitosan and chitosan-GO was prepared as the hydrogel structure on the thread. The result showed that the CS-GO hydrogel exhibited the highest color intensity of glucose sensor. This probably cause by the water absorption property of the hydrogel.

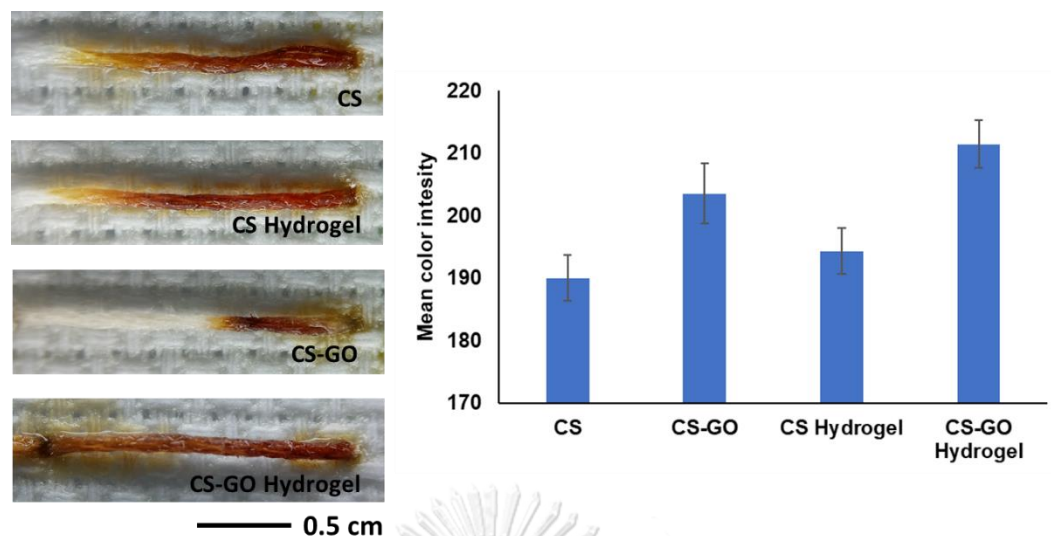


**Figure 4.25** Thread-based sensor modified with chitosan (CS), chitosan hydrogel (CS Hydrogel), chitosan-graphene oxide (CS-GO) and chitosan graphene oxide hydrogel (CS-GO hydrogel) at the glucose detection zone of 3 mM glucose. The error bars correspond to standard deviation obtained from five measurements (n=3)

#### 4.6.1.4 Effect of graphene oxide loading

The previous experiments suggested that the chitosan-GO hydrogel modified thread showed the highest color intensity of glucose detection. Therefore, the concentration of graphene oxide was optimized and systematically investigated. Figure 4.26 showed the chitosan-GO hydrogel modified thread with different concentrations of graphene oxide in a range of 0- 0.5 mg mL<sup>-1</sup>. The color intensity of this system increases from 0 to 0.01 mg mL<sup>-1</sup> of GO. This suggesting that GO was incorporated with thread leading to increase the surface functional active group for enzyme immobilization. When the concentration of GO is more than 0.01 mg mL<sup>-1</sup>, resulting in the decreasing of color intensity of this system. This is probably caused by the agglomeration of GO. Thus, 0.01 mg mL<sup>-1</sup> of GO loading was chosen for the further experiments.

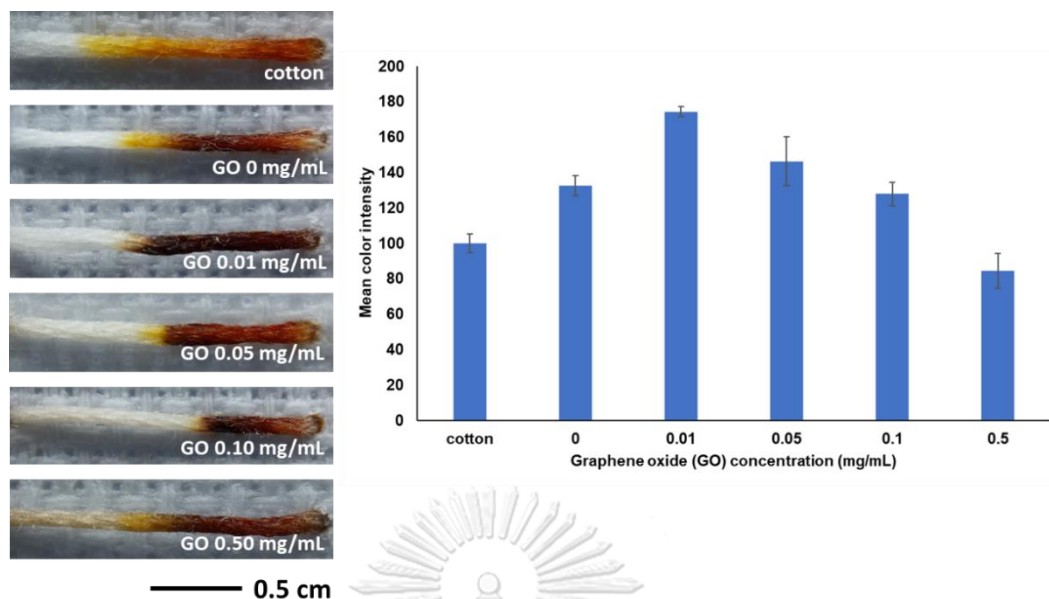


**Figure 4.26** Chitosan-graphene oxide hydrogel modified thread with different concentration of graphene oxide ( $0 - 0.5 \text{ mg mL}^{-1}$ ) at the glucose detection zone of 3 mM glucose. The error bars correspond to standard deviation obtained from five measurements ( $n=5$ ).

#### 4.6.1.5 Optimization of phenol red

The concentration of phenol red was systematically optimized. This urea sensor aims to distinguish normal and abnormal level of urea. So, this sensor was used to test urea at 60 and 120 mM. The results showed that  $2 \text{ mg mL}^{-1}$  of phenol red can significantly differentiated urea between 60 and 120 mM (Figure 4.27). Therefore,  $2 \text{ mg mL}^{-1}$  of phenol red was chosen for the further experiments.

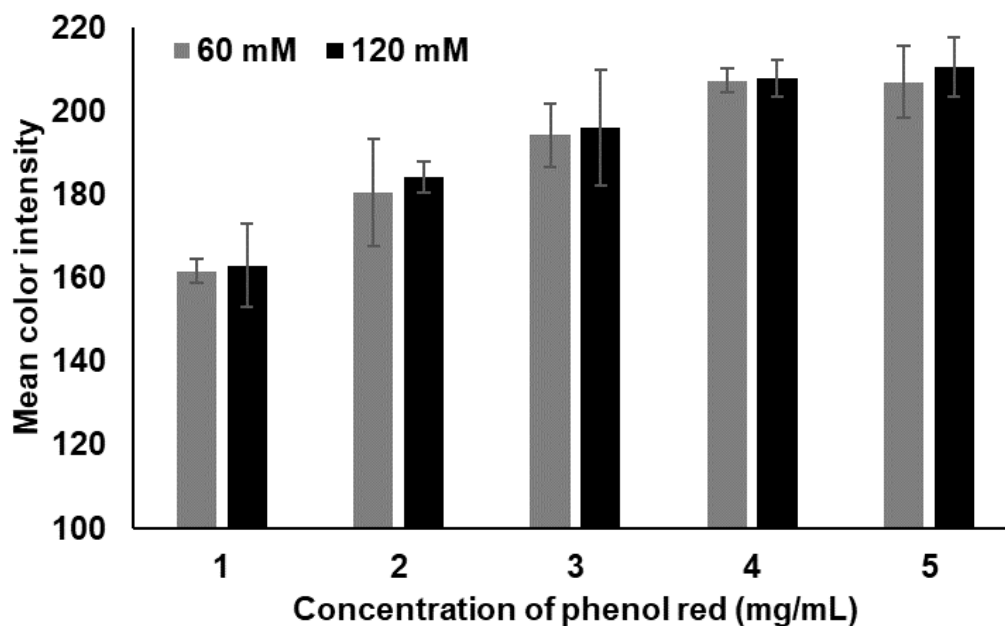
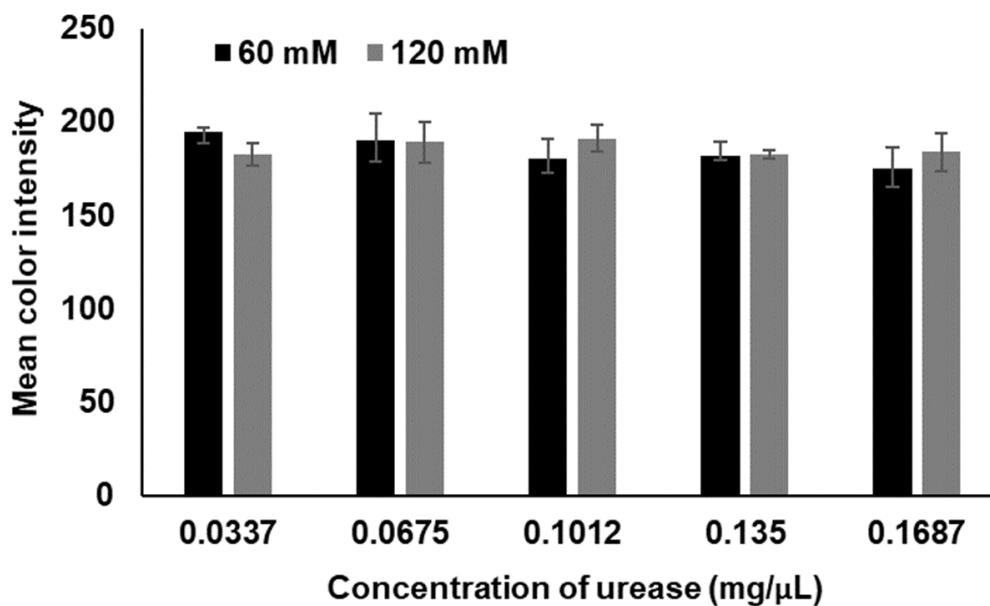


Figure 4.27 Thread-based sensor with different concentration of phenol red (1 – 5  $\text{mg mL}^{-1}$ ) at the urea detection area of 60 and 120 mM urea. The error bars correspond to standard deviation obtained from five measurements ( $n=5$ ).

#### 4.6.1.6 Optimization of ureases enzyme

The concentration of urease enzyme was optimized. The result showed that  $0.1012 \text{ mg } \mu\text{L}^{-1}$  of urease enzyme was clearly differentiated urea between 60 and 120 mM (Figure 4.28). Hence,  $0.1012 \text{ mg } \mu\text{L}^{-1}$  of urease enzyme was chosen for the further experiments.



**Figure 4.28** Thread-based sensor with different concentration of urease enzyme ( $0.03 - 0.17 \text{ mg mL}^{-1}$ ) at the urea detection zone of 60 and 120 mM urea. The error bars correspond to standard deviation obtained from five measurements ( $n=5$ ).

#### 4.7 Physical characterization of different layers of modified cotton thread

The morphologies of the thread surface were characterized by SEM. Figure 4.29a, b showed the unmodified cotton thread, which is smooth fibers surface with loosely threaded. The chitosan-GO coated cotton thread observed thin coated film of chitosan-GO composite coated on the thread Figure 4.29c, d. The enzymatic assay coating (*i.e. glucose and urea assay*) on the thread surface showed a thicker coated film as shown in Figure 4.29f-h.



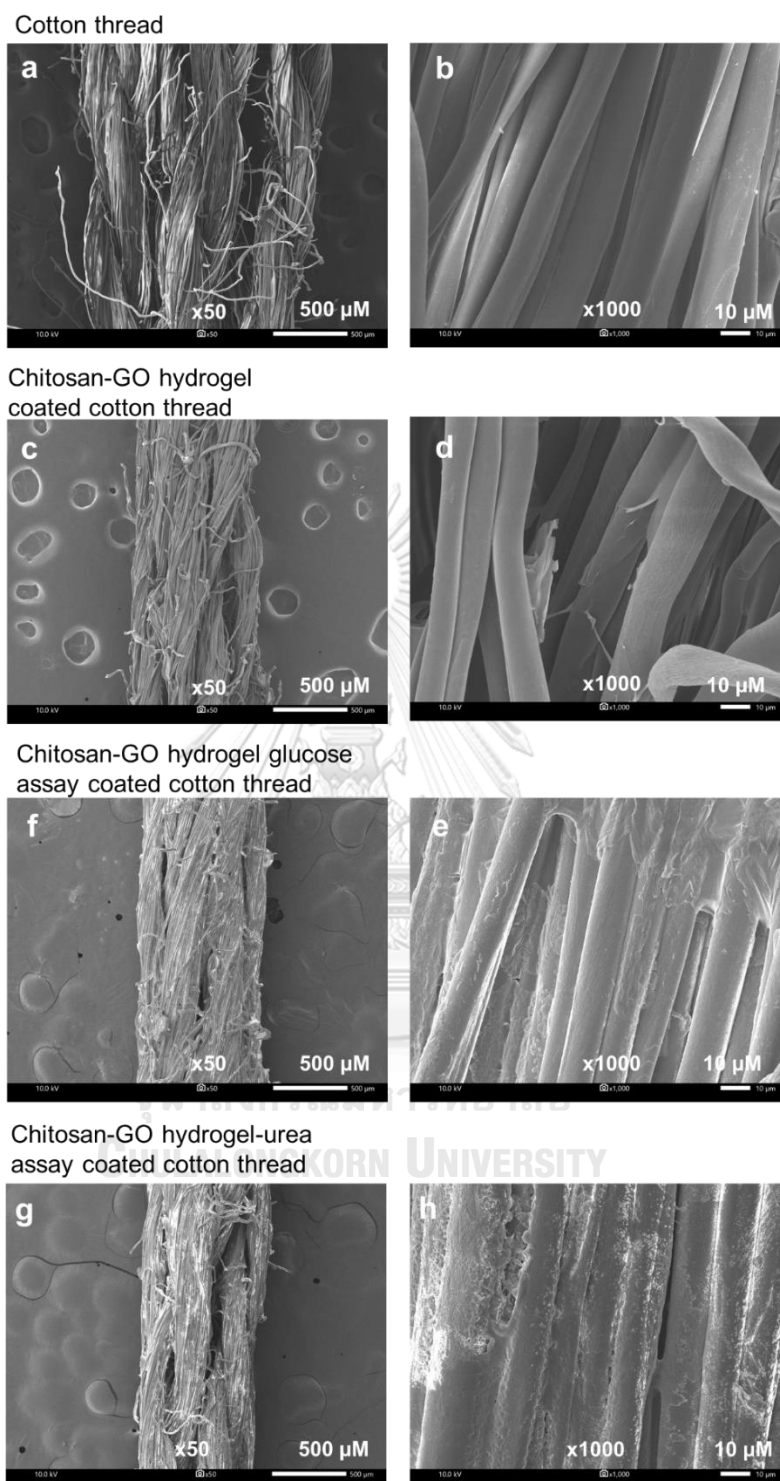


**Figure 4.29** SEM images (low and high magnification) of cotton thread (a, b), chitosan-GO hydrogel coated thread (c, d), chitosan-GO hydrogel-glucose assay coated thread (e, f) and chitosan-GO hydrogel-urea assay coated thread (g, h).

## 4.8 Chemical characterization of the modified sensing layer

### 4.8.1 FT-IR characterization

Figure 4.30 shows the FTIR spectra of the unmodified and the chitosan-GO hydrogel coated cotton thread. The peak at  $3300\text{ cm}^{-1}$  which is related to the stretching vibration of the hydroxyl groups displays significantly broader characteristic when the thread was coated with chitosan-GO solution. This could be caused by electrostatic interaction between chitosan and GO [110, 111]. FT-IR spectra of coated layer showed a similar peak to the cotton thread because of small amount of coating layer on the thread surface.

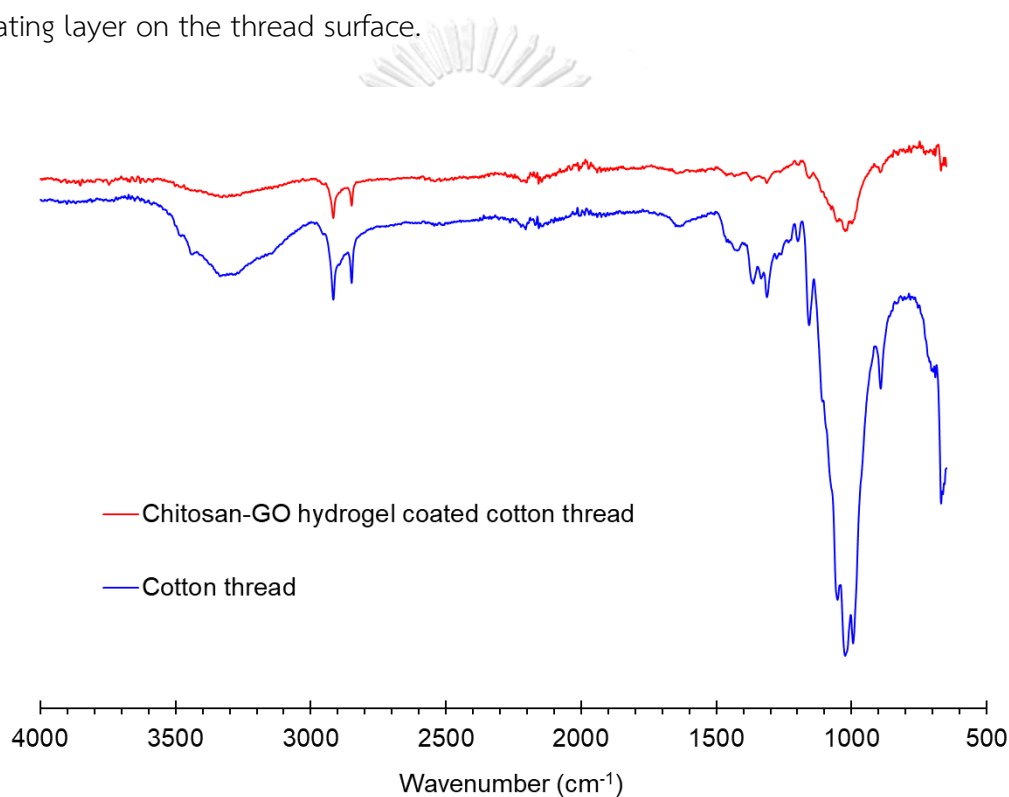


**Figure 4.30** FTIR spectra of different sensor layers of thread based colorimetric sensor.

### 4.8.2 XPS characterization

Figure 4.31 shows the XPS spectra of the unmodified, chitosan coated, and chitosan-GO hydrogel coated cotton thread. The carbon and oxygen peaks of all thread samples (*i.e. unmodified, chitosan and chitosan-GO hydrogel coated cotton thread*) are observed as shown in Figure 4.31. For the chitosan and chitosan-GO

hydrogel coated cotton thread, the nitrogen peak was observed indicating that the chitosan film was formed on the cotton thread (Figure 4.31e, h) [112]. The chitosan-GO hydrogel coated cotton thread showed a higher oxygen peak at  $532.2 \pm 0.3$  which is related to the oxygen-containing function groups on the GO structure (Figure 4.31g) [113].

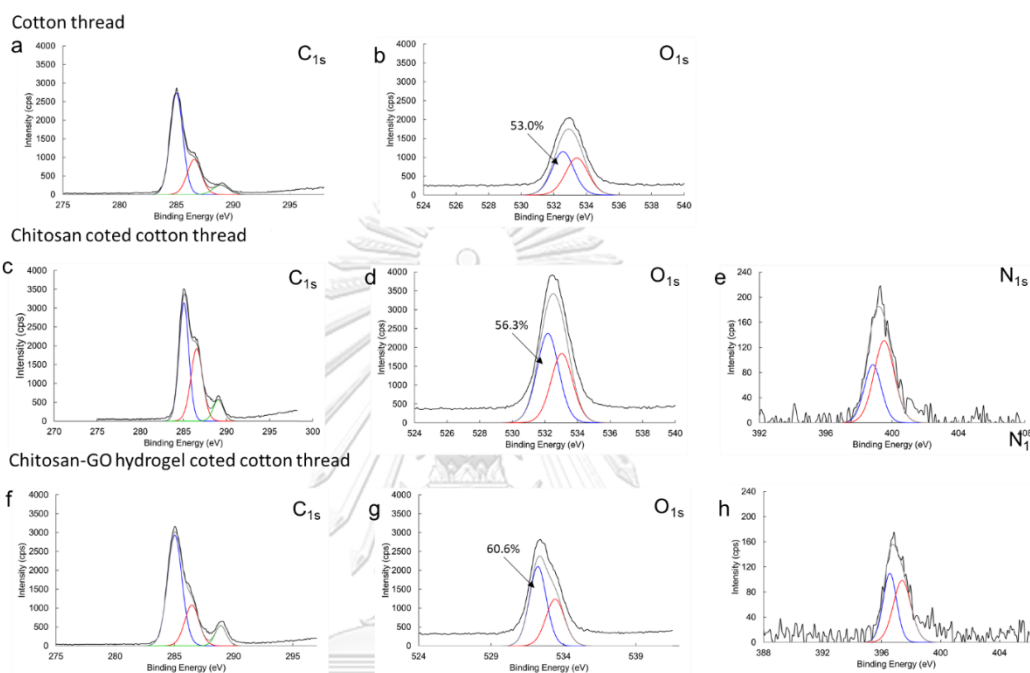


**Figure 4.31** The XPS spectra of unmodified, chitosan, chitosan-GO hydrogel coated cotton threads.

## 4.9 Sensor performance testing

### 4.9.1 Standard color chart of cotton thread-based glucose sensor

The color intensity of glucose sensor is directly proportional to the glucose concentration as shown in Figure 4.32. The linear range was found to be 0 – 3 mM with a correlation coefficient ( $R^2$ ) of 0.9916. The result showed that this sensor can detect glucose in a range of 0 – 3 mM that is the glucose level in sweat (0.277 – 1.11 mM) [114].

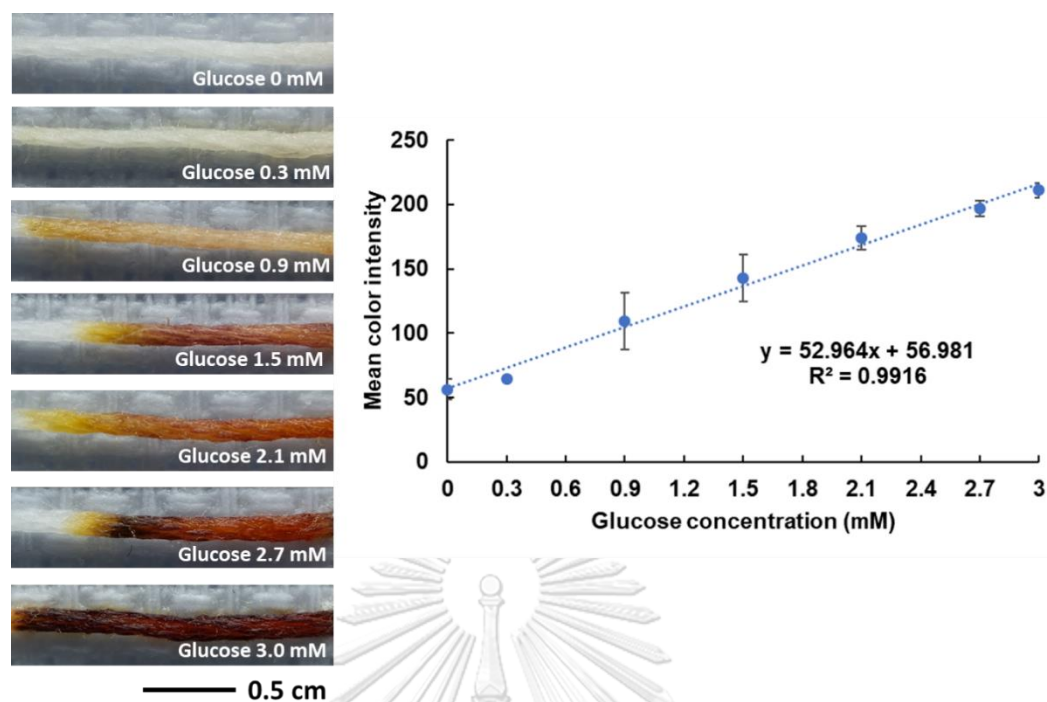


**Figure 4.32** Standard color chart of thread-based glucose sensor in the concentration range of 0 – 3 mM (left) and the plot of glucose concentration versus the mean color intensity (right). The error bars correspond to standard deviation obtained from five measurements (n=5)

#### 4.9.2 Standard color chart of cotton thread-based urea sensor

This color intensity of urea sensor is linearly proportional with the urea concentration as shown in Figure 4.33. However, the correlation coefficient ( $R^2$ ) is smaller number that the relationship is not strong enough to use for the quantitative analysis. From the result, the thread-based urea sensor can be differentiated urea between 30 and 60 mM. This suggesting that the sensor can distinguish between the normal (< 65 mM) and abnormal level of urea (>65 mM). Therefore, this urea sensor is suitable for the urea screening.

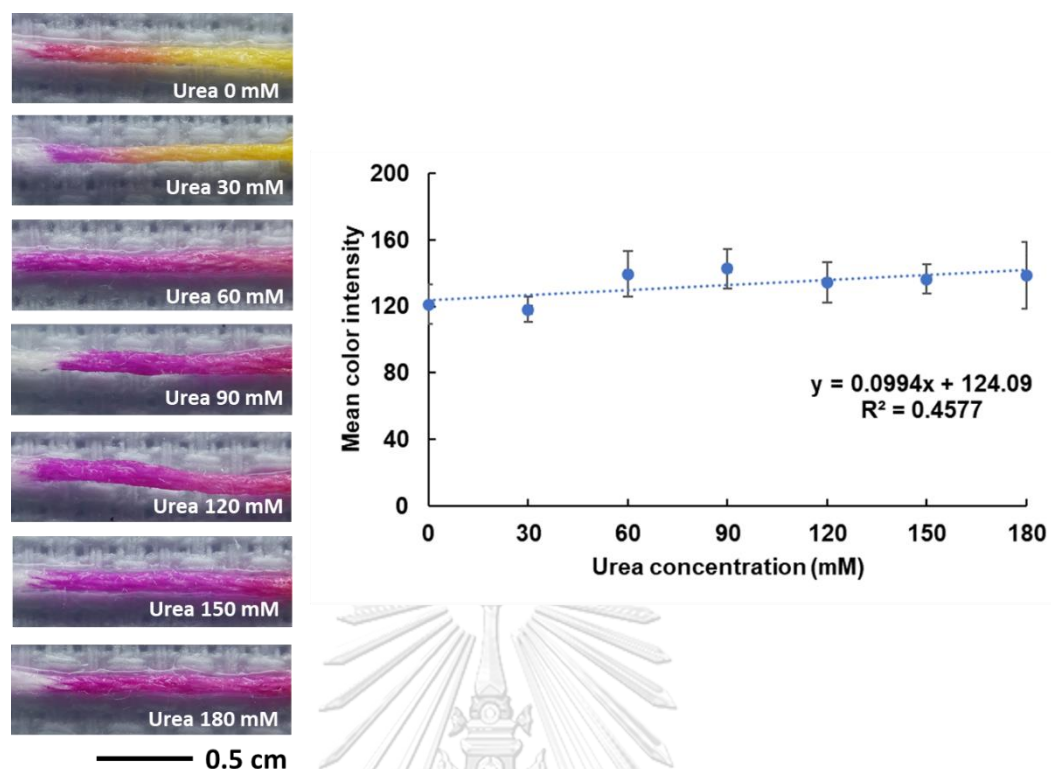


**Figure 4.33** Standard color chart of thread-based urea sensor in the concentration range of 0 – 180 mM (left) and the plot of urea concentration versus the mean color intensity (right). The error bars correspond to standard deviation obtained from five measurements ( $n=5$ )

#### 4.9.3 Simultaneous detection of glucose and urea

This thread based colorimetric sensor was applied for the simultaneous detection of glucose and urea in the artificial sweat pH 7.4 as shown Figure 4.34. The different concentration of mixed glucose and urea was added into the artificial sweat that cover low, medium and high concentration of analytes. This color change of thread sensor was compared with the standard color chart as shown in Table 4.5. This suggesting that this sensor can be used for the detection of both qualitative and quantitative of glucose while urea can detect only qualitative.

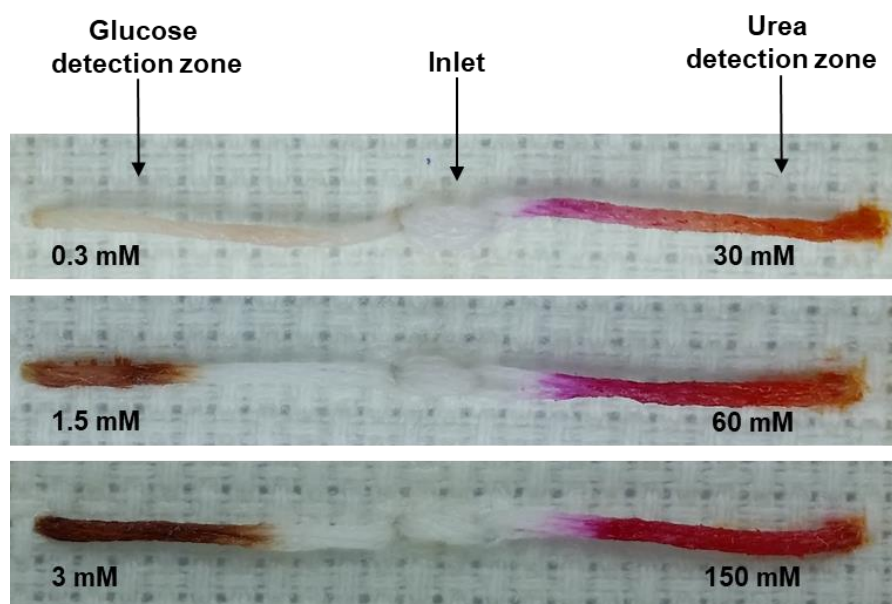


**Figure 4.34** The thread based colorimetric sensor with simultaneous glucose and urea detection at low, medium and high concentration of analyte.

**Table 4.5** Simultaneous determination of glucose and urea at low, medium and high concentration in artificial sweat pH 7.4

Mixed glucose and urea sample	Glucose (mM)		Urea (mM)	
	Qualitative	Quantitative	Qualitative	Quantitative
0.3 mM glucose-30 mM urea	≈0.3	0.3048±7.57	<60	N/A
1.5 mM glucose-60 mM urea	≈1.5	1.5053±26.58	>60	N/A
3.0mM glucose-150 mM urea	≈3.0	2.8598±6.87	>60	N/A

## CHAPTER V

### CONCLUSIONS

This study, G and GO nanocomposite was successfully prepared and applied for chemical sensor application to improve both electrochemical and colorimetric sensitivity that can be concluded into two parts as follows:

#### **Part I: GO nanocomposite coated metal substrate for electrochemical sensor**

The NiP-TiO<sub>2</sub> sol-RGO was successfully prepared by one-step electroless deposition process. The incorporation of RGO with the well-dispersed and homogeneous covering on the substrate exhibited a high electrical conductivity and high corrosion resistance. Moreover, this coated surface showed a hydrophobic surface which enhance anti-corrosion property, which is potentially useful for various applications that requires anti-corrosion and high electrical conductivity such as energy storage device, electronic circuit and electrochemical sensor.

#### **Part II: GO nanocomposite coated textile substrate**

A novel platform of non-invasive textile based colorimetric sensor was developed for the simultaneous detection of marker in sweat (*i.e.* pH, lactate, glucose and urea) to obtain the individual health information. The cotton fabric sensor can qualitatively detect both sweat pH and lactate based on the color change by the naked eyes compared to the standard color chart. The incorporation of mixed MO and BCG indicator dyes and lactate enzymatic assay into cotton substrate can differentiate the sweat pH and lactate level change in human sweat. Also, the cotton thread sensor can detect both glucose and urea based on colorimetric analysis. The incorporation of chitosan-GO hydrogel on the cotton thread was used to enhance the enzyme immobilization on the surface leading to enhance the sensitivity of the sensor. Moreover, thread based colorimetric sensor can created the microfluidic device by itself and reduced the volume of reagent and sample.

This textile based sensor will be further applied with sportswear such as shirt, wristband, which might be an alternative tool for screening step in sport and medical diagnosis leading to improvement of sport performance and decrease of medical diagnosis costs in the future.

## REFERENCES



จุฬาลงกรณ์มหาวิทยาลัย  
**CHULALONGKORN UNIVERSITY**



1. Kim, J., et al., Wearable salivary uric acid mouthguard biosensor with integrated wireless electronics. *Biosensors and Bioelectronics*, 2015. **74**: p. 1061-1068.
2. Kuila, T., et al., Recent advances in graphene-based biosensors. *Biosensors and Bioelectronics*, 2011. **26**(12): p. 4637-4648.
3. Wang, J., Nanomaterial-based electrochemical biosensors. *Analyst*, 2005. **130**(4): p. 421-426.
4. Harper, A. and M.R. Anderson, Electrochemical Glucose Sensors—Developments Using Electrostatic Assembly and Carbon Nanotubes for Biosensor Construction. *Sensors*, 2010. **10**(9).
5. Rattanawaleedirojn, P., et al., TiO<sub>2</sub> sol-embedded in electroless Ni-P coating: a novel approach for an ultra-sensitive sorbitol sensor. *RSC Adv.*, 2016. **6**(73): p. 69261-69269.
6. Sadhir, M.H., et al., Comparison of in situ and ex situ reduced graphene oxide reinforced electroless nickel phosphorus nanocomposite coating. *Applied Surface Science*, 2014. **320**: p. 171-176.
7. Lee, X.J., et al., Review on graphene and its derivatives: Synthesis methods and potential industrial implementation. *Journal of the Taiwan Institute of Chemical Engineers*, 2019. **98**: p. 163-180.
8. McDonald, M.P., et al., Spectroscopy and Microscopy of Graphene Oxide and Reduced Graphene Oxide, in *Graphene Oxide: Reduction Recipes, Spectroscopy, and Applications*, W. Gao, Editor. 2015, Springer International Publishing: Cham. p. 29-60.
9. Banerjee Arghya, N., Graphene and its derivatives as biomedical materials: future prospects and challenges. *Interface Focus*, 2018. **8**(3): p. 20170056.
10. Hulanicki, A., S. Geab, and F. Ingman, Chemical sensors definitions and classification *Pure & Appl. Chem* 1991. **63**(9): p. 1247-1250.
11. Bandodkar, A.J. and J. Wang, Non-invasive wearable electrochemical sensors: a review. *Trends in Biotechnology*, 2014. **32**(7): p. 363-371.
12. Bănică, F.-G., What are Chemical Sensors?, in *Chemical Sensors and Biosensors*. 2012, John Wiley & Sons, Ltd. p. 1-20.
13. Schlesinger, M., Electroless deposition of nickel, in *Modern Electroplating*, M. Schlesinger and M. Paunovic, Editors. 2010, John Wiley & Sons, Inc.

14. Balaraju, J.N., Kalavati, and K.S. Rajam, Influence of particle size on the microstructure, hardness and corrosion resistance of electroless Ni-P-Al<sub>2</sub>O<sub>3</sub> composite coatings. *Surf. Coat. Technol.*, 2006. **200**(12-13): p. 3933-3941.
15. Novakovic, J. and P. Vassiliou, Vacuum thermal treated electroless NiP-TiO<sub>2</sub> composite coatings. *Electrochim. Acta* 2009. **54**(9): p. 2499-2503.
16. Novakovic, J. and P. Vassiliou, Vacuum thermal treated electroless NiP-TiO<sub>2</sub> composite coatings. *Electrochimica Acta*, 2009. **54**(9): p. 2499-2503.
17. Niksefat, V. and M. Ghorbani, Mechanical and electrochemical properties of ultrasonic-assisted electroless deposition of Ni-B-TiO<sub>2</sub> composite coatings. *Journal of Alloys and Compounds*, 2015. **633**: p. 127-136.
18. Makkar, P., R.C. Agarwala, and V. Agarwala, Chemical synthesis of TiO<sub>2</sub> nanoparticles and their inclusion in Ni-P electroless coatings. *Ceram. Int.*, 2013. **39**(8): p. 9003-9008.
19. Makkar, P., R.C. Agarwala, and V. Agarwala, Wear characteristics of mechanically milled TiO<sub>2</sub> nanoparticles incorporated in electroless Ni-P coatings. *Adv. Powder Technol.*, 2014. **25**(5): p. 1653-1660.
20. Zhao, Q., et al., Antibacterial characteristics of electroless plating Ni-P-TiO<sub>2</sub> coatings. *Appl. Surf. Sci.*, 2013. **274**: p. 101-104.
21. Xiong, L., G.Q. Zhang, and H.G. Pan, Study on the preparation of Ni-P-TiO<sub>2</sub> coatings by electroless plating and its photocatalytic properties. *Adv. Mater. Res.*, 2011. **311-313**: p. 319-322.
22. Chen, W., W. Gao, and Y. He, A novel electroless plating of Ni-P-TiO<sub>2</sub> nano-composite coatings. *Surf. Coat. Technol.*, 2010. **204**(15): p. 2493-2498.
23. Shibli, S.M.A., N.D. Suma, and V.S. Dilimon, Development of TiO<sub>2</sub>-supported RuO<sub>2</sub> composite-incorporated Ni-P electrodes for amperometric measurement of ethanol. *Sensors and Actuators B: Chemical*, 2008. **129**(1): p. 139-145.
24. Chang, K.-C., et al., Room-temperature cured hydrophobic epoxy/graphene composites as corrosion inhibitor for cold-rolled steel. *Carbon*, 2014. **66**(Supplement C): p. 144-153.

25. Liu, X.-W., et al., Fabrication of metal-graphene hybrid materials by electroless deposition. *Carbon*, 2011. **49**(2): p. 477-483.
26. Wu, H., et al., Preparation of Ni-P-GO composite coatings and its mechanical properties. *Surface and Coatings Technology*, 2015. **272**: p. 25-32.
27. Hu, Q.-h., et al., Synthesis of Ni/graphene sheets by an electroless Ni-plating method. *New Carbon Materials*, 2012. **27**(1): p. 35-41.
28. Jakub, T., et al., Comparison of Electrochemical Methods for the Evaluation of Cast AZ91 Magnesium Alloy. *Materials*, 2016. **9**(925).
29. *Materials Evaluation and Engineering, I. Handbook of Analytical Methods for Materials*. [cited 2019 25 May]; Available from: <https://www.primeadvertising.com/publications/MEE/MEE2016Handbook/html5/index.html?page=1&noflash>.
30. Natarajan, K.A. *Advances in Corrosion Engineering Advances in Corrosion Engineering* [cited 2019 25 May]; Available from: <https://nptel.ac.in/courses/113108051/module2/lecture10.pdf>.
31. Wang, J., *Study of Electrode Reactions and Interfacial Properties. Analytical Electrochemistry*, 2006.
32. Bard, A.J.a.F., L.R., *Electrochemical methods : fundamentals and applications*, ed. 2. 2001, the United States of America: John Wiley & Sons, Inc.
33. Bicker, K.L., S.L. Wiskur, and J.J. Lavigne, *Colorimetric Sensor Design, in Chemosensors*. 2011, John Wiley & Sons, Inc. p. 275-295.
34. Sempionatto, J.R., et al., Eyeglasses based wireless electrolyte and metabolite sensor platform. *Lab on a Chip*, 2017. **17**(10): p. 1834-1842.
35. Elsherif, M., et al., Wearable Contact Lens Biosensors for Continuous Glucose Monitoring Using Smartphones. *ACS Nano*, 2018. **12**(6): p. 5452-5462.
36. Tseng, R.C., et al., Contact-Lens Biosensors. *Sensors (Basel, Switzerland)*, 2018. **18**(8): p. 2651.
37. Gao, W., et al., Fully integrated wearable sensor arrays for multiplexed in situ perspiration analysis. *Nature*, 2016. **529**: p. 509.

38. Mishra, R.K., et al., Wearable Flexible and Stretchable Glove Biosensor for On-Site Detection of Organophosphorus Chemical Threats. *ACS Sensors*, 2017. **2**(4): p. 553-561.
39. Bandodkar, A.J., et al., Tattoo-based potentiometric ion-selective sensors for epidermal pH monitoring. *Analyst*, 2013. **138**(1): p. 123-128.
40. Koh, A., et al., A soft, wearable microfluidic device for the capture, storage, and colorimetric sensing of sweat. *Science Translational Medicine*, 2016. **8**(366): p. 366ra165.
41. Jia, W., et al., Electrochemical Tattoo Biosensors for Real-Time Noninvasive Lactate Monitoring in Human Perspiration. *Analytical Chemistry*, 2013. **85**(14): p. 6553-6560.
42. Anastasova, S., et al., A wearable multisensing patch for continuous sweat monitoring. *Biosensors and Bioelectronics*, 2017. **93**: p. 139-145.
43. Promphet, N., et al., Non-invasive textile based colorimetric sensor for the simultaneous detection of sweat pH and lactate. *Talanta*, 2019. **192**: p. 424-430.
44. Caldara, M., et al., Optical monitoring of sweat pH by a textile fabric wearable sensor based on covalently bonded litmus-3-glycidoxypropyltrimethoxysilane coating. *Sensors and Actuators B: Chemical*, 2016. **222**: p. 213-220.
45. Baysal, G., et al., Microfluidic device on a nonwoven fabric: A potential biosensor for lactate detection. *Textile Research Journal*, 2014. **84**(16): p. 1729-1741.
46. Martín, A., et al., Epidermal Microfluidic Electrochemical Detection System: Enhanced Sweat Sampling and Metabolite Detection. *ACS Sensors*, 2017. **2**(12): p. 1860-1868.
47. Chang, Y.-T., et al., Flexible direct-growth CNT biosensors. *Biosensors and Bioelectronics*, 2013. **41**: p. 898-902.
48. Xu, M., D. Obodo, and V.K. Yadavalli, The design, fabrication, and applications of flexible biosensing devices. *Biosensors and Bioelectronics*, 2019. **124-125**: p. 96-114.

49. Figueredo, F., et al., Enhanced Analytical Performance of Paper Microfluidic Devices by Using Fe<sub>3</sub>O<sub>4</sub> Nanoparticles, MWCNT, and Graphene Oxide. *ACS Applied Materials & Interfaces*, 2016. **8**(1): p. 11-15.
50. Ragavan, K.V., et al., Chitosan as a peroxidase mimic: Paper based sensor for the detection of hydrogen peroxide. *Sensors and Actuators B: Chemical*, 2018. **272**: p. 8-13.
51. Aminabhavi, T.M. and S.P. Dharupaneedi, 12 - Production of chitosan-based hydrogels for biomedical applications, in *Chitosan Based Biomaterials Volume 1*, J.A. Jennings and J.D. Bumgardner, Editors. 2017, Woodhead Publishing. p. 295-319.
52. Ravi Kumar, M.N.V., A review of chitin and chitosan applications. *Reactive and Functional Polymers*, 2000. **46**(1): p. 1-27.
53. Gabriel, E.F.M., et al., Highly sensitive colorimetric detection of glucose and uric acid in biological fluids using chitosan-modified paper microfluidic devices. *Analyst*, 2016. **141**(15): p. 4749-4756.
54. Gabriel, F.E., et al., Paper-Based Colorimetric Biosensor for Tear Glucose Measurements. *Micromachines*, 2017. **8**(4).
55. Ezati, P., H. Tajik, and M. Moradi, Fabrication and characterization of alizarin colorimetric indicator based on cellulose-chitosan to monitor the freshness of minced beef. *Sensors and Actuators B: Chemical*, 2019. **285**: p. 519-528.
56. Xu, W., et al., Simultaneous color sensing of O<sub>2</sub> and pH using a smartphone. *Sensors and Actuators B: Chemical*, 2015. **220**: p. 326-330.
57. Chang, C. and L. Zhang, Cellulose-based hydrogels: Present status and application prospects. *Carbohydrate Polymers*, 2011. **84**(1): p. 40-53.
58. Buenger, D., F. Topuz, and J. Groll, Hydrogels in sensing applications. *Progress in Polymer Science*, 2012. **37**(12): p. 1678-1719.
59. Nam, J., et al., A colorimetric hydrogel biosensor for rapid detection of nitrite ions. *Sensors and Actuators B: Chemical*, 2018. **270**: p. 112-118.
60. Li, G., et al., Label-free 2D colloidal photonic crystal hydrogel biosensor for urea and urease inhibitor. *Sensors and Actuators B: Chemical*, 2018. **277**: p. 591-597.

61. Lim, S.L., et al., Biosensing of hepatitis B antigen with poly(acrylic acid) hydrogel immobilized with antigens and antibodies. *Sensors and Actuators B: Chemical*, 2017. **252**: p. 409-417.
62. Zhang, Y., et al., Bio-inspired layered chitosan/graphene oxide nanocomposite hydrogels with high strength and pH-driven shape memory effect. *Carbohydrate Polymers*, 2017. **177**: p. 116-125.
63. Kahlert, H., G. Meyer, and A. Albrecht, Colour maps of acid–base titrations with colour indicators: how to choose the appropriate indicator and how to estimate the systematic titration errors. *ChemTexts*, 2016. **2**(2): p. 7.
64. Sabnis, R.W., *Handbook of Acid-Base Indicators*. 2007: CRC Press (Taylor & Francis Group PLC).
65. Ito, S., Structural features of bromocresol purple and its binding sites on human serum albumin for a proton-exchange reaction. Vol. 6. 2016. 71-77.
66. Curto, V.F., et al., Real-time sweat pH monitoring based on a wearable chemical barcode micro-fluidic platform incorporating ionic liquids. *Sensors and Actuators B: Chemical*, 2012. **171**: p. 1327-1334.
67. Soni, A. and S.K. Jha, Smartphone based non-invasive salivary glucose biosensor. *Analytica Chimica Acta*, 2017. **996**: p. 54-63.
68. Jadoon, S., et al., Recent Developments in Sweat Analysis and Its Applications. *International Journal of Analytical Chemistry*, 2015: p. 1-7.
69. Mena-Bravo, A. and M.D. Luque de Castro, Sweat: A sample with limited present applications and promising future in metabolomics. *Journal of Pharmaceutical and Biomedical Analysis*, 2014. **90**: p. 139-147.
70. Zhou, Y., et al., Real-time colorimetric hydration sensor for sport activities. *Materials & Design*, 2016. **90**: p. 1181-1185.
71. Toh, H.S., et al., Electrochemical detection of chloride levels in sweat using silver nanoparticles: a basis for the preliminary screening for cystic fibrosis. *Analyst*, 2013. **138**(15): p. 4292-4297.
72. Wujcik, E.K., et al., Ion Sensor for the Quantification of Sodium in Sweat Samples. *IEEE Sensors Journal*, 2013. **13**(9): p. 3430-3436.

73. Matzeu, G., L. Florea, and D. Diamond, Advances in wearable chemical sensor design for monitoring biological fluids. *Sensors and Actuators B: Chemical*, 2015. **211**: p. 403-418.
74. Patterson, M.J., S.D.R. Galloway, and M.A. Nimmo, Variations in regional sweat composition in normal human males. *Experimental Physiology*, 2000. **85**(6): p. 869-875.
75. Morgan, R.M., M.J. Patterson, and M.A. Nimmo, Acute effects of dehydration on sweat composition in men during prolonged exercise in the heat. *Acta Physiologica Scandinavica*, 2004. **182**(1): p. 37-43.
76. Derbyshire, P.J., et al., Lactate in human sweat: a critical review of research to the present day. *The Journal of Physiological Sciences*, 2012. **62**(6): p. 429-440.
77. Andrus, P.L., et al., Characterization of Lactate Sensors Based on Lactate Oxidase and Palladium Benzoporphyrin Immobilized in Hydrogels. *Biosensors*, 2015. **5**(3).
78. Roda, A., et al., A 3D-printed device for a smartphone-based chemiluminescence biosensor for lactate in oral fluid and sweat. *Analyst*, 2014. **139**(24): p. 6494-6501.
79. Lamas-Ardisana, P.J., et al., Disposable amperometric biosensor based on lactate oxidase immobilised on platinum nanoparticle-decorated carbon nanofiber and poly(diallyldimethylammonium chloride) films. *Biosensors and Bioelectronics*, 2014. **56**: p. 345-351.
80. Sakchai, K., Partnering to innovate diabetes care in Thailand. *The Blueprint for Change Programme*, 201.
81. IDF Diabetes Atlas-8th Edition. International Diabetes Federation, 2017.
82. Kim, J., A.S. Campbell, and J. Wang, Wearable non-invasive epidermal glucose sensors: A review. *Talanta*, 2018. **177**: p. 163-170.
83. Hwang, D.-W., et al., Recent advances in electrochemical non-enzymatic glucose sensors – A review. *Analytica Chimica Acta*, 2018. **1033**: p. 1-34.
84. Kim, K., et al., Fabrication of a Urea Biosensor for Real-Time Dynamic Fluid Measurement. *Sensors (Basel, Switzerland)*, 2018. **18**(8): p. 2607.

85. Soni, A., R.K. Surana, and S.K. Jha, Smartphone based optical biosensor for the detection of urea in saliva. *Sensors and Actuators B: Chemical*, 2018. **269**: p. 346-353.
86. Tangwivat, S. and S.J. Milne, Diol-based sol-gel as a novel binder for barium titanate ceramics. *J. Sol-Gel Sci. Technol.*, 2005. **34**(2): p. 147-154.
87. Rattanawaleedirojn, P., et al., TiO<sub>2</sub> sol-embedded in electroless Ni-P coating: a novel approach for an ultra-sensitive sorbitol sensor. *RSC Advances*, 2016. **6**(73): p. 69261-69269.
88. Evans, E., et al., Modification of Microfluidic Paper-Based Devices with Silica Nanoparticles. *The Analyst*, 2014. **139**(21): p. 5560-5567.
89. Wilson, N.R., et al., Graphene Oxide: Structural Analysis and Application as a Highly Transparent Support for Electron Microscopy. *ACS Nano*, 2009. **3**(9): p. 2547-2556.
90. Huh, S.H., Thermal Reduction of Graphene Oxide Physics and Applications of Graphene - Experiments 2011: p. 73-90.
91. Štengl, V., et al., TiO<sub>2</sub>-graphene oxide nanocomposite as advanced photocatalytic materials. *Chemistry Central Journal*, 2013. **7**(1): p. 1-12.
92. Eluri, R. and B. Paul, Microwave assisted greener synthesis of nickel nanoparticles using sodium hypophosphite. *Mater. Lett.*, 2012. **76**: p. 36-39.
93. Ye, X.H., et al., Corrosion resistance of graphene directly and locally grown on bulk nickel substrate by laser irradiation. *RSC Advances*, 2015. **5**(45): p. 35384-35390.
94. Singh Raman, R.K., et al., Protecting copper from electrochemical degradation by graphene coating. *Carbon*, 2012. **50**(11): p. 4040-4045.
95. Chang, C.-H., et al., Novel anticorrosion coatings prepared from polyaniline/graphene composites. *Carbon*, 2012. **50**(14): p. 5044-5051.
96. Zhang, W., et al., Synergetic effect of metal nickel and graphene as a cocatalyst for enhanced photocatalytic hydrogen evolution via dye sensitization. *Scientific Reports*, 2015. **5**: p. 10589.
97. Nine, M.J., et al., Robust Superhydrophobic Graphene-Based Composite Coatings with Self-Cleaning and Corrosion Barrier Properties. *ACS Applied Materials & Interfaces*, 2015. **7**(51): p. 28482-28493.



98. Kuang, D., et al., Graphene–nickel composites. *Applied Surface Science*, 2013. **273**: p. 484-490.
99. Sahu, S.C., et al., A facile electrochemical approach for development of highly corrosion protective coatings using graphene nanosheets. *Electrochemistry Communications*, 2013. **32**: p. 22-26.
100. Singh, B.P., et al., The production of a corrosion resistant graphene reinforced composite coating on copper by electrophoretic deposition. *Carbon*, 2013. **61**: p. 47-56.
101. Chang, K.-C., et al., Room-temperature cured hydrophobic epoxy/graphene composites as corrosion inhibitor for cold-rolled steel. *Carbon*, 2014. **66**: p. 144-153.
102. Jensen, J.A.D., et al., Electrochemical Deposition of Buried Contacts in High-Efficiency Crystalline Silicon Photovoltaic Cells. *Journal of The Electrochemical Society*, 2003. **150**(1): p. G49-G57.
103. Saha, T.K., Adsorption of Methyl Orange onto Chitosan from Aqueous Solution. *Journal of Water Resource and Protection*, 2010. **Vol.02No.10**: p. 9.
104. Wijesena, R.N., N.D. Tissera, and K.M.N. de Silva, Coloration of cotton fibers using nano chitosan. *Carbohydrate Polymers*, 2015. **134**(Supplement C): p. 182-189.
105. Urban, G.A. and T. Weiss, Hydrogels for Biosensors, in *Hydrogel Sensors and Actuators: Engineering and Technology*, G. Gerlach and K.-F. Arndt, Editors. 2010, Springer Berlin Heidelberg: Berlin, Heidelberg. p. 197-220.
106. Chung, C., M. Lee, and E.K. Choe, Characterization of cotton fabric scouring by FT-IR ATR spectroscopy. *Carbohydrate Polymers*, 2004. **58**(4): p. 417-420.
107. Granger, D., et al., Na<sup>+</sup>/H<sup>+</sup> exchangers in the human eccrine sweat duct. *American Journal of Physiology - Cell Physiology*, 2003. **285**(5): p. C1047.
108. Bueno, D., et al., Colorimetric Analysis of Ochratoxin A in Beverage Samples. *Sensors (Basel, Switzerland)*, 2016. **16**(11): p. 1888.
109. Irfan, M., et al., Thermodynamic and Spectroscopic Investigation of Interactions between Reactive Red 223 and Reactive Orange 122 Anionic Dyes and Cetyltrimethyl Ammonium Bromide (CTAB) Cationic Surfactant in Aqueous Solution. *The Scientific World Journal*, 2014. **2014**: p. 540975.

110. Liu, Y., et al., Structure and properties of carboxymethyl cotton fabric loaded by reduced graphene oxide. *Carbohydrate Polymers*, 2019. **214**: p. 117-123.
111. Tian, M., et al., Ultraviolet protection cotton fabric achieved via layer-by-layer self-assembly of graphene oxide and chitosan. *Applied Surface Science*, 2016. **377**: p. 141-148.
112. Tian, M., et al., Electromagnetic interference shielding cotton fabrics with high electrical conductivity and electrical heating behavior via layer-by-layer self-assembly route. *RSC Advances*, 2017. **7**(68): p. 42641-42652.
113. Ye, X., et al., A Knittable Fibriform Supercapacitor Based on Natural Cotton Thread Coated with Graphene and Carbon Nanoparticles. *Electrochimica Acta*, 2016. **206**: p. 155-164.
114. Makaram, P., D. Owens, and J. Aceros, Trends in Nanomaterial-Based Non-Invasive Diabetes Sensing Technologies. *Diagnostics (Basel, Switzerland)*, 2014. **4**(2): p. 27-46.



## VITA

**NAME** Nadtinan Promphet

**DATE OF BIRTH** 13 December 1988

**PLACE OF BIRTH** Suratthani, Thailand

**INSTITUTIONS ATTENDED** 2015-present: Ph.D. Candidate in Nanoscience and Technology Interdisciplinary Program Chulalongkorn University, Bangkok, Thailand (Expected graduation date: July 2019)  
2011-2014: M. Sc. in Petrochemical and Polymer Science Chulalongkorn University, Bangkok, Thailand  
2007-2010: B. Sc. in Industrial Chemistry King Mongkut's Institute of Technology Ladkrabang, Bangkok, Thailand

**HOME ADDRESS** 99, Moo 10, Krud, Kanchanadit, Suratthani, Thailand, 84160

**PUBLICATION**

1. Promphet, N., Rattanawaleedirojn, P., Siralertmukul, K., Soatthiyanon, N., Potiyaraj, P., Thanawattano, C., Hiestroza, J. P., Rodthongkum, N., Non-invasive textile based colorimetric sensor for the simultaneous detection of sweat pH and lactate. *Talanta* 2019, 192, 424-430.
2. Promphet, N., Rattanawaleedirojn, P., Rodthongkum, N. Electroless NiP-TiO<sub>2</sub> sol-RGO: a smart coating for enhanced corrosion resistance and conductivity of steel, *Surface & coatings technology*. 2017, 325, 604-610.
3. Rattanawaleedirojn, P., Saengkiattiyut, K., Boonyongmaneerat, Y., Sangsuk, S., Promphet, N., Rodthongkum, N. TiO<sub>2</sub> sol-embedded in electroless Ni-P coating: a novel approach for an ultra-sensitive sorbitol sensor, *RSC Advance* 2016, 6(73) 69261-69269.

4. Promphet, N., Rattanarat, P., Rangkupan, R., Chailapakul, O., Rodthongkum, N. An electrochemical sensor based on graphene/polyaniline/polystyrene nanoporous fibers modified electrode for simultaneous determination of lead and cadmium. *Sensors and Actuators B: Chemical* 2015, 207, 526-534.

5. Promphet, N., Rangkupan, R., Rattanarat, P., Thueploy, A., Rodthongkum, N., Chailapakul, O. Electrospun graphene/polyaniline modified carbon electrode for heavy metal detection. *Proceeding of Pure and Applied Chemistry International Conference 2014*. 2014, 409-412.

6. Rodthongkum, N., Ruecha, N., Promphet, N., Rangkupan, R., Vachet, R.W., Chailapakul O., Graphene-Loaded Nanofiber-Modified Electrode: A Novel and Sensitive Electrochemical Detection System. *Nanotech 2014*. 2014, 1, 72-75.